ERASMUS MUNDUS FUSION DC

International Doctoral College in Fusion Science and Engineering

European Commission ERASMUS MUNDUS

Electromagnetic properties of edge turbulence in fusion plasma devices

PhD Thesis presented by: **Bing Liu**

Thesis supervisors:

Carlos Hidalgo Vera (CIEMAT)
Monica Spolaore (Consorzio RFX)

Thesis promoters:

José Ramón Martín Solís (Universidad Carlos III de Madrid)
Paolo Bettini (Università degli Studi di Padova, Centro Ricerche Fusione)

Doctoral Programme in Plasmas and Nuclear Fusion (Universidad Carlos III de Madrid); Physics Department

Joint European Doctorate and Network in Fusion Science and Engineering (Università degli Studi di Padova)

Leganés, November 2016

Universidad Carlos III de Madrid
www.uc3m.es

Università degli Studi di Padova

ERASMUS MUNDUS FUSION DC

International Doctoral College in Fusion Science and Engineering

European Commission ERASMUS MUNDUS

Electromagnetic properties of edge turbulence in fusion plasma devices

Author: Bing Liu

Thesis Directors: Carlos Hidalgo Vera, Monica Spolaore

Examination Committee:

Signature

President:

Vocal:

Secretary:

Mark:

Leganés, November 2016

Universidad Carlos III de Madrid
www.uc3m.es

Università degli Studi di Padova

Acknowledgements

CIEMAT:

First of all, I would like to thank my supervisor, Dr. Carlos Hidalgo, for introducing me to the area of plasma turbulence and proposing the exciting research topics. His guidance and encouragement always motivate me to think about new ideas which make everyday working at CIEMAT enjoyable. His attitude toward research, being open-minded and critical in thinking, especially kind in treating people has set a model of great scientist for me to pursue in my future career.

I would like to thank Boudewijn van Milligen for his generosity in sharing his knowledge and assistance with data analysis. I appreciate very much his succinct and elegant answers, in his 'FusionWiki' style, to many of my questions on fusion plasma and data analysis.

I am indebted to Maria Angeles Pedrosa for teaching me all the practical issues of probe measurements and guiding me through many of the experiments in TJ-II.

I want to thank Ulises Losada and Adriana Martin de Aguilera for their assistance with preparing and conducting experiments in TJ-II. I would like to extend my thanks to Eduardo de la Cal for teaching me fast camera operation, Paco Tabares for his support with the diagnostics and analysis of particle confinement time, Bernardo Zurro and Kieran McCarthy for the measurements D/H ratio for the isotope effect experiments in TJ-II. I would like to thank Arturo Alonso and Jose Luis Velasco for their insightful comments and discussions on the study of potential asymmetries in TJ-II. I am also grateful to Enrique Ascasibar, Paco Castejon, Teresa Estrada, Daniel Lopez-Bruna, Marian Ochando, Alvaro Cappa and Macarena Liniers for their support with experiments and kindly explaining to me many concepts relating to research topics in TJ-II. I also wish to acknowledge Jose Luis De Pablos, Gregorio Martin, Justo Lopez and Raul Garcia for their expertise in the electronics and DAQ system of the probes and electrode in TJ-II. A big thanks also goes to my office mates Fernando Martin and Alfonso de Castro, and Baojun Sun for their help with my life and study in Spain.

Universidad Carlos III de Madrid:

I am deeply grateful to my promotor, Professor José Ramón Martín Solís, for his kindness in preparing and managing my mobility and funding for my study in FUSION-DC, especially

for his kindness in consideration of my finance support in the last year of study. I would also like to thank Ana Belén, Rocío Pañero Martín, Aaron Hernandez and Jorge Alcusón for their help with my paperworks and study.

RFX and University of Padova:

I would like to thank my co-supervisor, Dr. Monica Spolaore, for her guidance and support for my study at RFX, and teaching me the interesting electromagnetic measurements and guiding me through the data analysis. I would also like to thank Professor Emilio Martines for arranging my stay in Padova and discussing my analysis results, and Dr. Gianluca De Masi for explaining to me about RFP configuration and helping me estimate the positions of m=0 islands for the study of magnetic topology effect. I also wish to thank Professor Paolo Bettini, Gianluigi Serianni, Fiorella Colautti, Yangyang Zhang and Xinyang Xu for their help with my study at RFX.

Instituto Superior Técnico (IST), Lisbon:

I would like to thank Carlos Silva preparing and guiding my isotope effect experiments in ISTTOK, and arranging my stay in Lisbon. I appreciate his always quick and helpful comments on my work. I would also like to thank Fernando Figueiredo for his support with the operation of ISTTOK and Tiago Pereira for measuring the D/H ratio for isotope effect experiments, and Rafael Henriques for helping me access the ISTTOK database.

Ghent University and FUSION-DC:

I would like to give a special thanks to Professor Guido Van Oost for bringing me into the Erasmus Mundus program for my Master and PhD studies and giving me a wonderful introduction to plasma physics and fusion engineering at Ghent University. I would also like to thank Professor Jean-Marie Noterdaeme, Kathleen Van Oost and Frank Janssens for organising my study in FUSION-DC.

I would like to acknowledge that this work was supported by the European Commission in the framework of the Erasmus Mundus International Doctoral College in Fusion Science and Engineering (FUSION-DC) and also supported in part by the Ministerio de Economia y Competitividad of Spain under project ENE2012-38620-C02-01.

My family:

Last but not least, I want to express my gratitude to my parents and brother for their support and understanding of my study abroad.

Abstract

This thesis work consists of three pillars. First, the isotope dependence of long-range correlation (due to, e.g. zonal flow and GAMs) has been studied in the TJ-II stellarator and ISTTOK tokamak with dual Langmuir probes. In TJ-II, it has been found that LRC slightly decreases with isotope mass, in contrast to tokamak results. In ISTTOK, GAM amplitude has been found to be higher in D than H dominated plasmas, in agreement with other tokamak results. Using biorthogonal decomposition (BOD), GAM and low frequency coherent modes were separated; their spectral and spatial structure properties were studied. In addition, measurements of Reynolds stress and Maxwell stress have been made using an electromagnetic probe during L-H transition in TJ-II. Second, macroscale flows and non-diffusive behavior of particle dynamics have been found around magnetic islands in TJ-II and RFX-mod with the analysis of long-range spatial and temporal correlation (Hurst exponent). In TJ-II, during dynamic configuration scan experiments, rational surfaces have been found to affect the development of long-range spatial and temporal correlation. In RFX-mod, LRC has been detected at both sides of the m=0 island. The possible relation between long-range temporal correlation (Hurst exponent) and the phase angle of magnetic perturbation was also studied. Third, a new strategy for studying plasma potential asymmetries in magnetic flux surface has been developed based on edge electrode biasing and probe measurements in TJ-II.

Contents

List of Figures

List of Tables

Part I

Introduction

Chapter 1

Introduction

1.1 Energy

The world energy demand is increasing mainly due to the population and economic growth. The continuous development of modern society requires the energy sources to be sustainable and environmentally friendly. However, currently over 80% of world energy comes from fossil fuels [1], including coal, oil and natural gas etc., which are limited in reserve. Moreover, CO^2 emissions from fossil fuel combustion is the main contribution to increase of the concentration of greenhouse gases and has an important effect on climate change. It has been reported that for our living environment the affordable level of increase in global average temperature above the pre-industrial levels is 2 ˚C, beyond which irreversible and almost uncontrollable catastrophic climate change is expected to take place. This increase has already reached 0.78 ˚C [2]. Therefore, it is urgent to find a way to reduce the energy-related CO^2 emissions. A short-term alleviation would be the development of new technologies to reduce CO^2 emissions from the fossil power plant and feasibility of large–scale CO^2 storage, while a long-term solution should consider the alternatives to fossil fuels. The only candidates with sufficient resources to take over the fossil fuels are solar, nuclear fission and nuclear fusion [3].

Solar energy is theoretically large and inexhaustible, but its intermittency (sunshine only in cloudy-free daytime) and low energy density (large area required) make it hard to build a solar power plant to produce significant amount of base load power. Nuclear fission is a well-established energy source and has been producing base load electricity for decades. However, the disposal of long half-life nuclear waste and the potential accident due to the intrinsic chain reaction of nuclear fission have long been a public concern.

Nuclear fusion holds promise for a clean and safe solution for our long-term energy needs [3]. First, fuel reserves are abundant. For deuterium and tritium reaction, deuterium can be

extracted from sea water; tritium does not naturally occur, but it can be bred from lithium isotope ^{6}Li. Second, nuclear fusion reactions emit no greenhouse gases or any other harmful chemicals into the atmosphere. Third, nuclear fusion is intrinsically safe. Fusion fuel is continuously fed into the reactor at a rate of sustaining the reaction for only a few tens of seconds at each instant. Fusion reaction can only happen under very high temperature and sufficiently accurate confinement field and no chain reaction involved. Any incorrect handling will stop the reaction.

1.2 Nuclear fusion

Protons and neutrons in a nucleus are hold together by short-range nuclear force. The energy required to disassemble a nucleus is called binding energy. Figure 1.1 shows that the average binding energy varies with elements; both lightest nuclei and heaviest have low average binding energy and the nuclei with intermediate mass have highest average binding energy. This shows that nuclear energy can be obtained by both splitting heavy nucleus (fission) and fusing light nuclei (fusion).

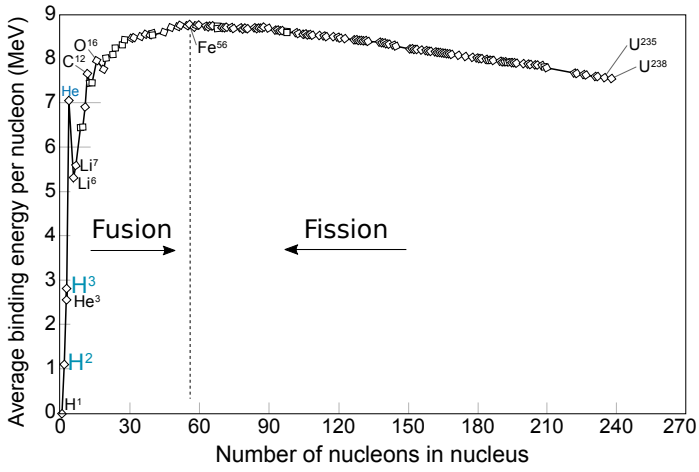

Figure 1.1. Average binding energy as a function of the mass number. Adapted from Wikipedia.com.

To achieve a fusion reaction, two nuclei need to gain sufficient kinetic energy to overcome the Coulomb repulsion and reach the short-range nuclear force regime. The first fusion reaction was experimentally realised with a deuterium (D) beam bombarding on a deuterium target [4], just after the discovery of deuterium (the hydrogen isotope of mass two [5]). It was during this bombardment experiments that the third hydrogen isotope, tritium (T), was discovered. After this accomplishment, the use nuclear fusion as an energy source was considered. However, it was recognised that bombarding a target with an accelerated beam

is not feasible for energy generation, because the energy used for accelerating the particle is much larger than the energy produced by the nuclear fusion reaction and most of the accelerated particles miss the target.

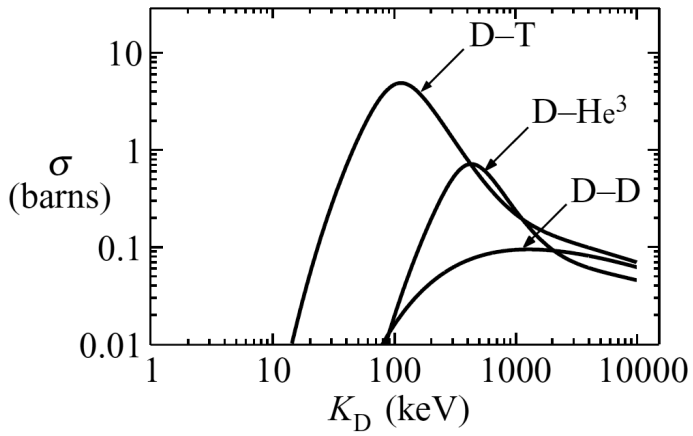

Figure 1.2. Cross-section for the reactions of D-T, D-D and D-^{3}He [3].

It is now generally accepted that the most feasible way for effective energy production from nuclear fusion is to heat the fusion fuels to high temperature, so that particles approach each other with strong thermal motion and nuclear reaction would take place. At such high temperature, the fusion fuels are ionised and in a state called plasma. Figure 1.2 shows the cross-sections (probability for nuclear reaction to occur) of different nuclear reactions. We can see the most promising reaction is between the deuterium and tritium producing neutron and α particle.

$$\mathrm{n} + \mathrm{T} \longrightarrow {}^4\mathrm{He}\ (3.5\mathrm{MeV}) + \mathrm{n}\ (14.1\mathrm{MeV}) \tag{1.1}$$

The produced energy is carried as kinetic energy by neutron and the α particle.

One of the important goal for realising fusion energy is to sustain the high temperature condition not by external heating but by energy produced by the nuclear reaction itself. This process is called ignition. To reach the ignition, the Lawson criteria [6] predicts that the following condition must be met:

$$nT\tau_E \geq 3 \times 10^{21} \mathrm{keVs/m^3} \tag{1.2}$$

where n is the plasma density, T the plasma temperature and τ_E energy confinement time. This triple product suggests that for effectively generating energy from nuclear fusion, plasma need to be confined at the high temperature plasma for sufficient long time with high density.

There are mainly two ways towards controlled fusion energy research: magnetic confinement fusion and inertial confinement fusion.

1.3 Magnetic confinement

1.3.1 Plasma

A plasma is an ionised gas, in which the electrons are stripped from the ions. The separation of positively and negatively charged particles gives rise to electric fields. Electrons are more mobile than ions in a plasma due to the small mass of an electron. Thus small charge separation can results in the electrostatic oscillation of electrons around the background ions. The frequency of this oscillation is called plasma frequency, $\omega_p = \frac{ne^2}{m_e \epsilon_0}$, representing a fundamental timescale in plasma physics. Fast movement of electrons can screen out charge imbalance in a plasma, which makes the bulk plasma neutral. The length scale over which the electrons screen out the charge imbalance is called the Debye length, $\lambda_D = \left(\frac{\epsilon_0 T_e}{ne^2}\right)^{1/2}$, where n is the number density, T_e is the electron temperature.

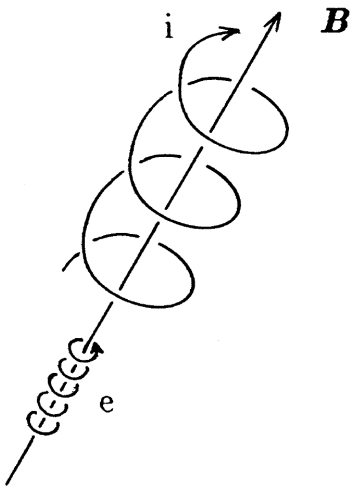

Figure 1.3. Motion of ion and electron in a magnetic field [7].

When a charged particle move with velocity **v** through an electric field **E** and magnetic field **B**, the electromagnetic force exerted on the charged particle is Lorentz force. Neglecting the gravity, the equation of motion is given by:

$$m\frac{d\mathbf{v}}{dt} = q(\mathbf{E} + \mathbf{v} \times \mathbf{B}) \tag{1.3}$$

In a straight uniform magnetic field, charged particle follows a spiral motion around the field line figure 1.3. This motion can be decomposed into a linear motion (guiding centre) along the field line and a circular motion, Larmor motion, perpendicular to the field line. Considering the Lorentz force equation (1.3), we get the cyclotron frequency ω_c and Larmor radius r_L of the motion as:

$$\omega_c = \frac{|q|B}{m} \tag{1.4}$$

$$r_L \equiv \frac{v_\perp}{\omega_c} = \frac{mv_\perp}{|q|B} \tag{1.5}$$

In a general electric field **E** and magnetic field **B**, i.e. **B** and **E** can vary in space and time, the guiding centre of the motion may drift across the magnetic fields. Based on the cause of the drift, the possible guiding center can be decomposed as: $\mathbf{E}\times\mathbf{B}$, ∇B, curvature, and polarization drift, $V_g = V_E + V_{\nabla B} + V_\kappa + V_p$. All these drifts basically arise due to the change or distortion of the Larmor orbits during the gyro motion. A fundamental guiding centre drift is the $\mathbf{E}\times\mathbf{B}$: $V_E = \frac{\mathbf{E}_\perp\times\mathbf{B}}{B^2}$. This is the basis for controlling small scale instabilities in a plasma.

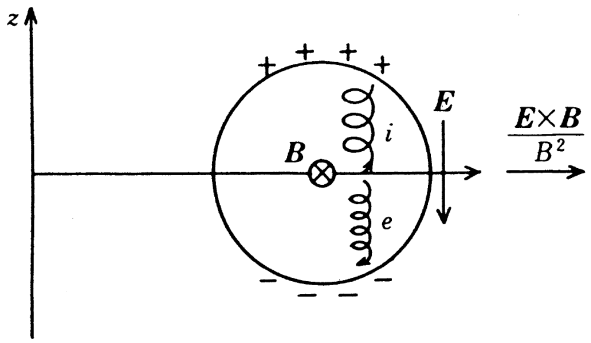

Figure 1.4. Charge separation caused by toroidal drift [7].

The guiding centre drifts provide an intuition for the understanding of plasma confinement. Due to the high mobility of charged particle along the magnetic field, there is always rapid end loss in an open field line device, like in straight cylinder and 'magnetic mirrors'. To avoid the end loss, the main configuration for magnetic confinement is built into torus. In a simple torus, vertical particle drift (e.g. due to ∇B drift) could occur and cause the separation of charged particles. This separation then results in electric fields. The $\mathbf{E}\times\mathbf{B}$ force will move the plasma outwards and degrade plasma confinement. This kind of charge separation can be compensated by helically twisting magnetic field lines around the torus, i.e. the total magnetic field is formed by the combination of a toroidal component B_ϕ and a

poloidal component B_θ. The number of poloidal transits per single toroidal transit of a field line on a toroidal flux surface is rational transform $\iota/2\pi$.

$$\frac{\iota}{2\pi} = \frac{d\psi}{d\Phi} \tag{1.6}$$

where ψ is the poloidal magnetic flux, and Φ the toroidal magnetic flux. More intuitively, if the field lines close on themselves after n poloidal and m toroidal transits of the torus, then $\iota = n/m$.

There are basically three ways of twisting the magnetic field, and thus creating rotational transform [8]:

(1) driving a toroidal current;

(2) elongating the flux surfaces and making them rotate poloidally as one moves around the torus;

(3) making the magnetic axis non-planar.

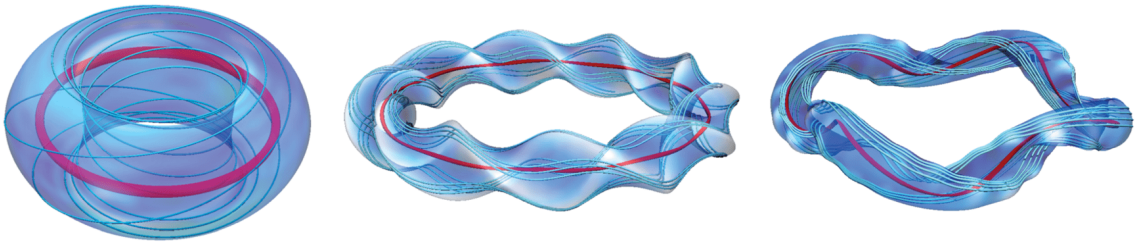

Figure 1.5. Outer flux surfaces (transparent blue), magnetic field lines (light blue), and magnetic axis (red) for tokamak, LHD stellarator, and TJ-II stellarator [9].

The magnetic configuration of toroidal fusion devices distinguish from each other mainly through the way of generating rotational transform. Tokamak and reverse-field pinch use the method (1). Some stellarators, for example LHD, use method (2). Some stellarators, for example, TJ-II and W7-X use both (2) and (3). Some more advanced design, for example NCSX, uses all three methods. Figure 1.5 shows the different ways of generating rotational transform.

The efficiency of confinement of plasma pressure by magnetic field is measured by plasma beta, defined as the ratio of the plasma pressure to the magnetic pressure.

$$\beta = \frac{\langle p \rangle}{B^2/2\mu_0} \tag{1.7}$$

1.3.2 Tokamak

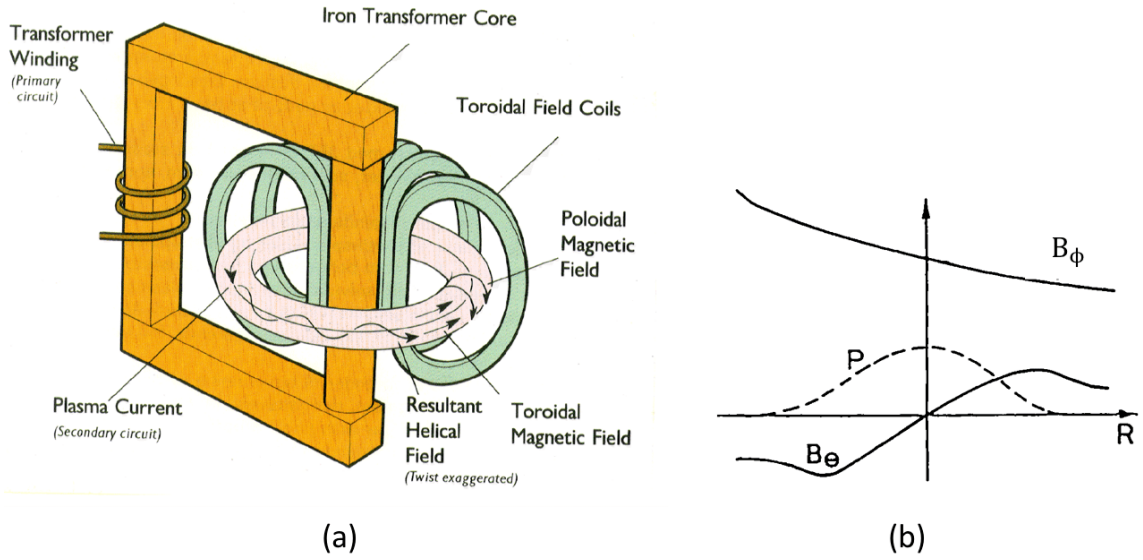

Figure 1.6. (a) Components of tokamak system; (b) typical profiles of toroidal and poloidal magnetic fields in a tokamak

The name tokamak originates from the acronym for the Russian words ***to****roidalnaya* ***ka****mera* ***ma****gnitnaya* ***k****atushka*, meaning 'toroidal chamber magnetic coils' [10]. A tokamak is a toroidal magnetic confinement system, which was first built in the late 1950's at Kurchatov Institute. This magnetic configuration is characterised by the combination of a strong toroidal field (B_ϕ) and a weak poloidal field (B_θ). As illustrated in the figure 1.6, the strong toroidal field is generated by the toroidal field coils along the torus, whereas the poloidal field is generated by the plasma current flowing along the torus. The plasma current are induced by a centre transformer; the plasma itself represents the secondary circuit. At the same time, plasma current also plays a role for Ohmic heating. In a tokamak, the twisting of magnetic field is measured by safety factor $q = \frac{rB_\phi}{RB_\theta}$, which relates to rotational transform through $q = 2\pi/\iota$.

The tokamak configuration is axisymmetric. The magnetic field lines are in principle uniform in the toroidal direction, except some small ripple fields from the separation of coils. The axisymmetry is a great advantage of tokamak configuration. Because this axisymmetry, the plasma confinement theory on tokamak has been well developed. [11]

Tokamak is the main configuration under investigation for fusion energy. The highest plasma parameters have been reached in tokamaks. The JET and TFTR tokamaks are the first devices which have achieved D-T fusion reactions. The largest fusion device ITER is being built as a tokamak. The roadmap to a feasible fusion reactor based on the tokamak

line is already established, while alternate concepts exist which may allow for further improvement. In this respect, the stellarator concept offers a route to a fusion power plant with unique capabilities: steady state operation, absence of plasma disruptions and high density operation.

1.3.3 Stellarator

In a stellarator, the rotational transform is produced by the helical fields generated by external coils [11]. This concept was first developed 1950s by Lyman Spitzer in Princeton[12]. The main advantage of stellarator is that it has potential to run plasmas in a steady state, because no plasma currents are needed for the generation of the poloidal magnetic fields. Then it does not have to suffer from disruptions of a toroidal plasma current. Figure 1.7 shows an a schematic of the magnetic coils of the stellarator Wendelstein 7-X, the largest stellarator in operation.

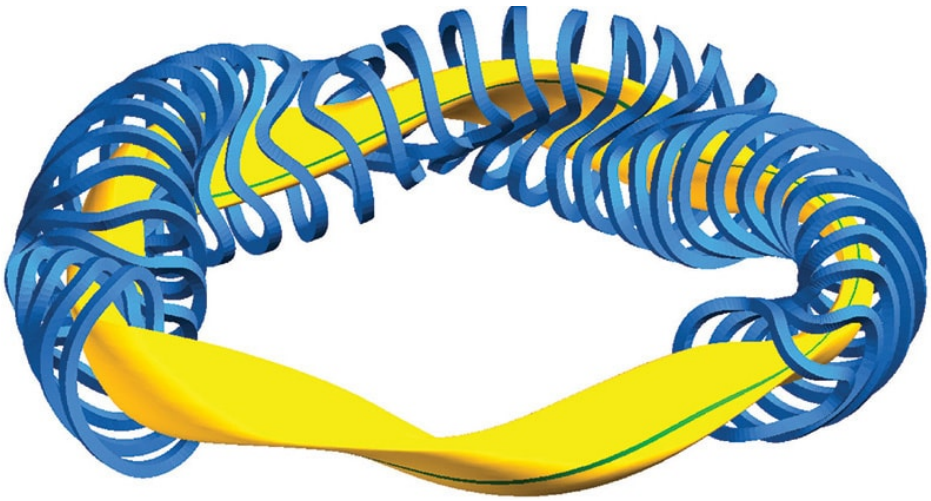

Figure 1.7. Schematic of the magnetic coils (blue) and magnetic field (green) in W7-X.

In a device without toroidal plasma current, Ampere's law implies that the integral of B_θ on a contour around the minor axis on each magnetic flux surface should vanish,

$$\oint \mathbf{B} \cdot d\mathbf{s} = 0 \tag{1.8}$$

.

This condition suggests that the poloidal field must change sign and magnitude along the contour and the field lines in a stellarator cannot wrap monotonically around the torus as in a tokamak. Instead, the magnetic field lines progress back and forth in the poloidal direction

as shown in figure 1.8. Therefore the stellarator magnetic field structure is a series of 'M' shape units, called the field periods. In each period, the magnetic field lines rotate in the poloidal direction [11].

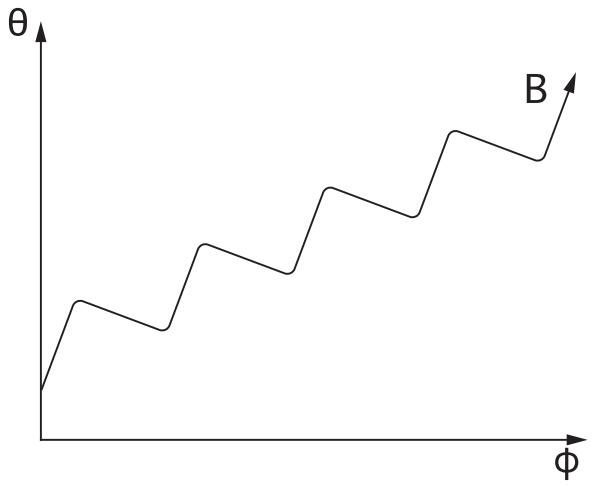

Figure 1.8. Illustration of stellarator magnetic field line on a flux surface, θ: poloidal angle, ϕ: toroidal angle.[11].

Compared with the axisymmetric tokamak, stellarators have approximately an order of magnitude more degrees of freedom in external magnetic fields[13]. Therefore, the stellarator configurations can be subdivided into different groups:

Classical stellarators l-fold poloidal symmetry is produced by 2l helical windings with alternating direction of current flow. Toroidal field coils are used to produced toroidal fields. This configuration is highly flexible, but the large alternating forces between the toroidal field coils and helical windings make the design of large scale experiments difficult.

Heliotron/Torsatron By changing the alternating direction of the current flow in the helical windings into unidirectional, i.e. the l-fold poloidal symmetry is produced by l helical windings, the stellarator becomes a heliotron, e.g. LHD. Since all current flow in the same direction, net toroidal field can also be produced. If the external toroidal field coils is eliminated, the helitron transforms into a torsatron, e.g. TJ-K. With careful design, a torsatron has potential to be made force-free.

Modular stellarator In this configuration, both toroidal and poloidal fields are produced by a system of discrete modular coils [14], e.g. Helically Symmetric Experiment (HSX).

Heliac A Heliac is a helical axis stellarator, in which the magnetic axis (and plasma) follows a helical line to form a toroidal helix rather than in one plane, e.g. TJ-II.

Helias A helical advanced stellarator, using an optimized modular coil set designed to simultaneously achieve high plasma, low Pfirsch-Schluter currents and good confinement of energetic particles; i.e. alpha particles for reactor scenarios, e.g. Wendelstein 7-X.

The successful start of the scientific exploitation of W7-X [15] is the first step towards bringing the stellarator to maturity as foreseen in the European Union roadmap.

Although the large degree of freedom in external magnetic fields makes it more difficult to design acceptable coils for stellarators than for the axisymmetric tokamak, it also offers large potential to optimise the coils [16, 17].

1.3.4 Reversed field pinch

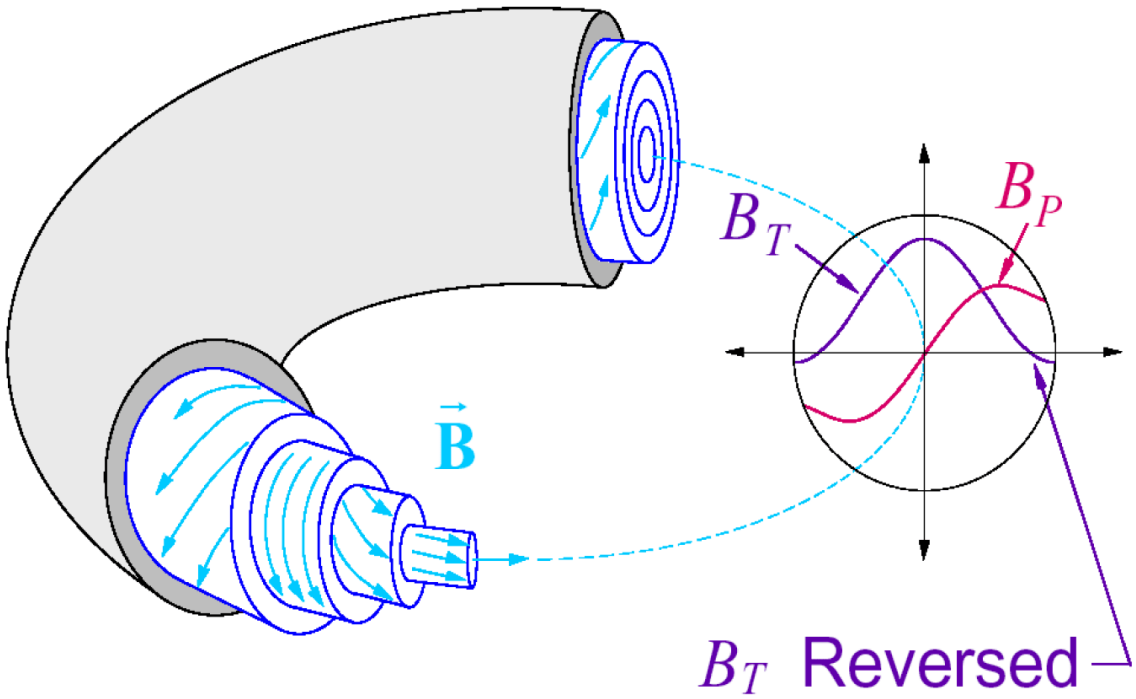

Figure 1.9. Schematic of the reversed field pinch magnetic field configuration.

The Reversed field pinch (RFP) is an axisymmetric toroidal confinement system [18]. RFP is characterised by its reversal of the toroidal component of magnetic field at the edge, as shown in figure 1.9. The feature makes the RFP attractive for magnetic fusion is the weak applied toroidal magnetic field.

The RFP configuration is obtained by driving a toroidal electrical current in a plasma embedded in a toroidal magnetic field, but the applied toroidal field is 10 – 100 times weaker. In a RFP device, a central solenoid is used to provide the loop voltage for triggering the discharge and driving a current in the confined plasma. A small toroidal bias field is embedded in the vacuum chamber. A large toroidal current is then ramped up which compresses both the plasma and the toroidal bias field. The plasma is heated by ohmic heating. The plasma temperature rises with the current raises. At the end of the current ramp, both of the toroidal and poloidal magnetic fields reach comparable magnitudes. Because most of the toroidal magnetic flux is trapped and compressed within the plasma, only a small residual toroidal field remains at the plasma edge. This field spontaneously reverses at the edge, which gives the names 'reversed field' pinch.

RFP equilibrium is a minimum energy relaxed state and can be explained on the basis of Taylor's relaxation theory [19]. Two dimensionless parameters are usually introduced to describe the RFP equilibrium, the pinch parameter Θ and the reversal parameter F:

$$\Theta = \frac{B_\theta(a)}{\left\langle B_\phi \right\rangle} \qquad F = \frac{B_\phi(a)}{\langle B_\theta \rangle} \tag{1.9}$$

where $\left\langle B_\phi \right\rangle$ is the average of B_ϕ over the poloidal section. Θ measures how much plasma and the magnetic field are pinched inside the torus, while F measures how much the toroidal field is reversed at the edge. In the RFP the reversal parameter F is always negative and the value Θ is usually high, while in tokamak the contrary is the case, F is positive and the Θ value is low.

1.4 Plasma turbulence and transport

1.4.1 Fluid Turbulence

In principle, all fluid motions are govern by Navier-Stokes equation, which is derived based on the application of Newton's second law to a fluid and continuity assumption. This does not necessarily mean that all fluid behaviours can be predicted by this equation. Consider the Navier–Stokes equation for a viscous, incompressible $\nabla \cdot \mathbf{u} = 0$ and homogeneous flow as:

$$\frac{\partial \mathbf{u}}{\partial t} + (\mathbf{u} \cdot \nabla)\mathbf{u} = -\nabla(p/\rho) + \mu \nabla^2 \mathbf{u} \tag{1.10}$$

where $\mathbf{u}$ is the velocity vector, ρ the density, p the pressure and μ the viscosity of the fluid. The nonlinear term $(\mathbf{u} \cdot \nabla)\mathbf{u}$ represents the convective acceleration and is also called inertia

term. $\mu\nabla^2\mathbf{u}$ is dissipation term. In fluid dynamics, if the dissipation term dominant, the disturbance in the initial condition is damped, the fluid behaves as a laminar flow. If, on the other hand, the inertia term dominates, the initial disturbance will experience continuos amplification, the fluid became turbulent. The ratio of the inertia term to the viscous force defines the Reynolds number:

$$R_e \sim \frac{(\mathbf{u}\cdot\nabla)\mathbf{u}}{\mu\nabla^2\mathbf{u}} \tag{1.11}$$

When the R_e exceeds some critical value, the solution of the Navier-stokes equation becomes unstable. The disturbance of the steady flow can grow due to the inertia, thus causing instability. For large R_e, the development of instabilities leads to a strongly fluctuating state of turbulence. Although in any one realisation the Navier-stokes equation is deterministic, over many realisations (repeat the measurement many times or measurements over longer time in a steady flow) the fluid dynamics is chaotic.

The turbulent velocity may be decomposed into the mean and fluctuating parts.

$$\mathbf{u} = \bar{\mathbf{u}} + \tilde{\mathbf{u}} \tag{1.12}$$

Substitute this decomposition into the Navier-stokes equation, the nonlinear term gives rise to a turbulent quantity $\rho\left\langle \tilde{u}_i\tilde{u}_j \right\rangle$, called Reynolds stresses. Turbulence is coupled to mean flow through Reynolds stress.

The motion of the fluctuating parts form the basic elements of turbulence, eddies (or vortices). The size of an eddy is around the distance over which the velocity varies significantly. This distance can be quantified by the velocity correlation in separated points $C_{ij}(\mathbf{r}) = \left\langle \tilde{u}_i(\mathbf{x})\tilde{u}_j(\mathbf{x}+\mathbf{r}) \right\rangle$, which is a generalisation of Reynolds stress and introduced first introduced by Taylor[20]. Vorticity $\omega = \nabla\times\mathbf{u}$ is an important concept in description of turbulence.

In three-dimensional (3D) turbulence at large Reynolds number, first, the inertial instabilities break up the mean flow and generate the largest eddies. Then, the large eddies themselves subject to inertial instabilities further breaking up and transferring energy into smaller eddies and so on. Through vortex stretching, energy passes from large eddies to small eddies without dissipation. This process is called energy cascade, as illustrated in figure 1.10 (a). The turbulent motion is considered the superposition of turbulent eddies of different sizes at each instant. Because of the dominance of inertia term, energy dissipation is negligible during the energy cascade. The energy spectrum is given by Kolmogorov's *five-thirds law* [21]:

$$E(k) = C\epsilon^{2/3}k^{-3/5} \tag{1.13}$$

where ϵ is the rate of cascade of kinetic energy per unit mass, k is the wavenumber. Energy dissipation becomes important when the eddy reach the smallest value so that the R_e becomes small ($R_e \approx 1$) and the viscous term play an important role. From dimensional analysis, Kolmogorov found smallest scale:.

$$\lambda_0 = (\nu^3/\epsilon)^{\frac{1}{4}} \tag{1.14}$$

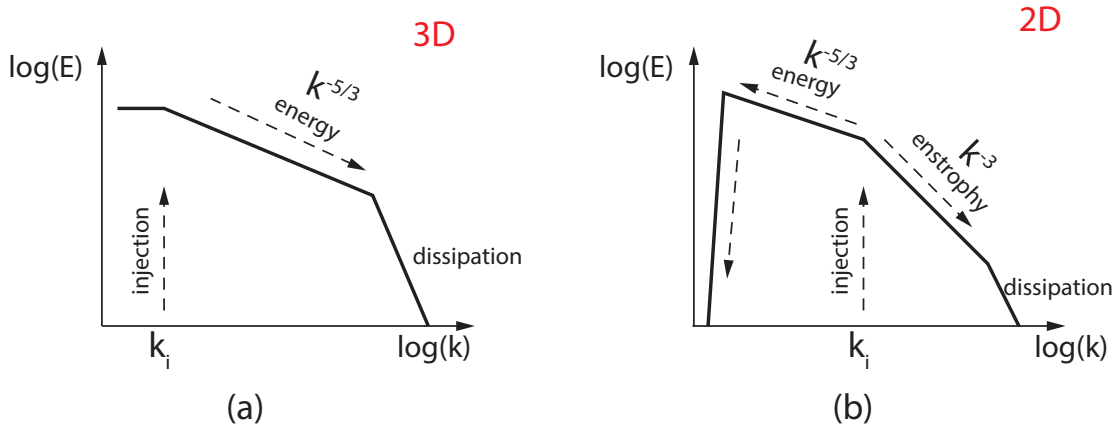

Figure 1.10. Illustration of the energy spectra for (a) 3D turbulence cascade and (b) 2D turbulence cascade.

In two-dimensional (2D) turbulence,i.e. $\mathbf{u}(\mathbf{x}, \mathbf{y}) = (u_x, u_y, 0)$, the vorticity is perpendicular to the 2D plane of fluid motion ($\mathbf{u} \cdot \mathbf{w} = 0$) and there is no vortex stretching ($(\mathbf{w} \cdot \nabla)\mathbf{u} = 0$). Before dissipation, vorticity is only advected and conserved. In contrast to 3D turbulence, dissipation now set the energy decay rate, not just the dissipation scales, because vorticity can no longer grow to balance viscosity reduction via vortex stretching. Vorticity structures cascade to smaller scales via the development of vortex sheets. This process is enstrophy cascade. The average energy remains constant, while vorticity decays. This implies if the energy is injected into the flow at constant rate at some intermediate range, the spectrum must be depleted large k (enstrophy direct cascade) but also filled at low k (energy inverse cascade), as illustrated in figure 1.10 (b). Following Kolmogorov's dimensional analysis, Kraichnan found the spectrum of this dual cascade [22]; the inverse energy cascade:

$$E(k) = C\epsilon^{2/3}k^{-3/5} \tag{1.15}$$

the enstrophy cascade:

$$E(k) = C'\eta^{2/3}k^{-3} \tag{1.16}$$

where C and C' are constants, ϵ is the rate of cascade of kinetic energy per unit mass, η is the rate of cascade of mean-square vorticity.

Although, strictly speaking, 2D turbulence does not really occur in nature, some flows have the properties of quasi-2D, for example, plasmas in a strong magnetic field. The generation of large scale zonal flow in magnetic fusion plasma seems to relate inverse energy cascade [23].

1.4.2 Plasma turbulence and confinement

Confined thermonuclear plasma is far from equilibrium, due to strong external drives that maintain steep gradients in the plasma parameters. The most obvious relaxation mechanism is via Coulomb collisions; in toroidal devices the resulting particle and energy fluxes are described by neoclassical transport theory. However, the plasma can also relax towards equilibrium through various types of instabilities: macro-instabilities and micro-instabilities. Whereas there are magnetic configurations that are stable to macro-instabilities it is likely that not all micro-instabilities can be stabilised.

Experimentally observed transport does not, in general, agree with calculated (neoclassical) values. In particular, electron energy transport can be over two orders of magnitude larger than the predictions from neoclassical theory; transport is anomalous. The heat and particle transport in fusion plasmas is generally due, in part, to turbulent process associated with small-scale instabilities driven by the inhomogeneity of density and temperature profiles in the direction normal to the magnetic surfaces. The magnitude of turbulent transport is probably the dominant parameter affecting the global confinement properties and hence the economical performance of a fusion reactor. Therefore, understanding the physics of anomalous transport in fusion devices remains one of the key issues in magnetic fusion research.

In the plasma edge region, turbulent transport is mainly due to two instabilities: the drift instability and the interchange instability.

Interchange instabilities

Figure 1.11 shows the way in which pressure gradient instabilities ('interchange instability') can develop in the plasma edge region in the presence of a magnetic field which comes out of the page and decreases with the distance to the plasma boundary (Figure 1.11(a)). In Figure 1.11(b), the plasma has developed a sight hump; the ions and electrons drift in opposite directions under the influence of the inhomogeneous magnetic field resulting in an electric field (Figure 1.11(c)). Under the combined influence of this electric field and the magnetic

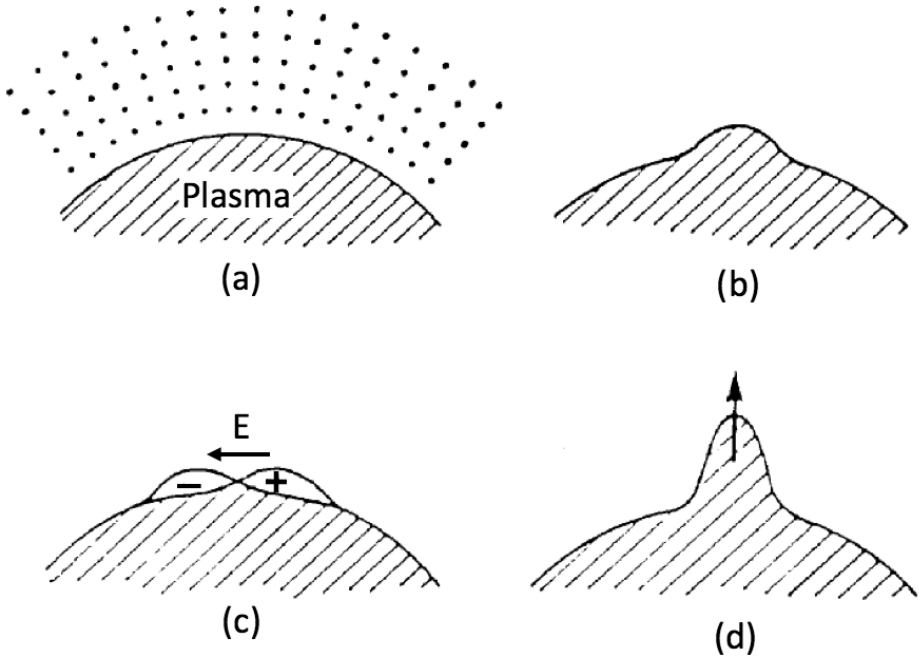

Figure 1.11. Schematic of the development of interchange instability in a toroidally confined plasma [24]

.

field the small bump will tend to grow creating an unstable situation in the plasma region in which the magnetic field intensity decreases as one moves radially out of the plasma boundary region. As a consequence of this mechanism, strong poloidal asymmetries are expected in the amplitude of fluctuations and turbulent transport, the maximum corresponding to those regions where the magnetic field intensity decreases as one moves away from the plasma.

Drift wave turbulence

Drift waves are low frequency (compared to the ion cyclotron frequency ω_{ci}) waves driven by gradients in ion and electron pressure gradients. The drift wave is stable if electron establish $\tilde{\phi}$ according to Boltzmann relation without delay ('adiabatic response'). Because of the low inertia, electrons flow rapidly along the field lines, generating an electric field parallel to magnetic field in order to establish force balance along the magnetic field given by,

$$n_e E_{\|} + \nabla_{\|} P_e = 0 \tag{1.17}$$

where P_e is the electron pressure, E is the electric and $\|$ represents the direction along magnetic field. Linearisation leads to a relation between the perturbed electron density $\tilde{n}_e$, and

electrostatic potential ϕ

$$\frac{\tilde{n}_e}{n_e} = \frac{e\phi}{T_e} \tag{1.18}$$

If a small perturbation in the ion and/or electron pressure gradient should occur, then the corresponding diamagnetic currents will developed a perturbed response [25]. Under the constrains that plasma is quasi-neutral and the divergence of the total perturbed current must vanish, a corresponding perturbed parallel current will be developed. Due to their small inertia, electron motion parallel to the magnetic field effectively generates this current. The resulting perturbations propagate predominantly in the ion and electron diamagnetic drift directions and are known as ion and electron drift waves. In the absence of dissipation of the parallel electron motion (i.e. adiabatic limit) the resulting drift wave density fluctuations will be in phase with the wave plasma potential fluctuations. If the electrons loses momentum to the background plasma as they move along to the magnetic field, the resulting dissipation will cause a delay of the response of the electron density to the plasma potential perturbation. As a result the potential perturbations are phase shifted relative to the density perturbation (i.e. non-adiabatic response). Figure 1.12 illustrates the mechanism of electron drift waves. The non-adiabatic response can occur via different processes including collisions, magnetic flutter or wave-kinetic effects. Examples of electron drift waves are: Trapped electron instabilities (TEM) caused by trapped electron dynamics and electron temperature gradient instabilities (ETG) caused by parallel compressibility (slab) or magnetic curvature (toroidal) [26].

Drift wave can also be due to ion mobility. In general, ion drift wave instabilities are caused by the impediment in the perpendicular ion motion. This impediment can result in the phase shift between density and potential fluctuations, even if the electron dynamics is adiabatic. An important ion drift wave is ion temperature gradient (ITG) instabilities. Drift waves can not be described in the framework of standard MHD; at least a 2-fluid description is needed.

1.4.3 Turbulence control: E×B sheared flow

Turbulence reduction by E × B sheared flow is an important discovery in fusion research[27]. The mechanism for turbulence suppression by sheared flow can be explained by the flow-induced decorrelation of turbulence. A large radial gradient in the radial electric field (E_r) can cause strong shear in the particle ($E_r \times B$) drift velocity. This strong shear tears apart the coherent cellular pattern of the unstable turbulence modes. The turbulence decorrelation time is inversely proportional to the radial gradient of the radial electric field, $\tau_c \approx \mathrm{B}(\mathrm{dE_r/dr})^{-1}$. On the other hand, the decorrelation time due to background diffusion is esti-

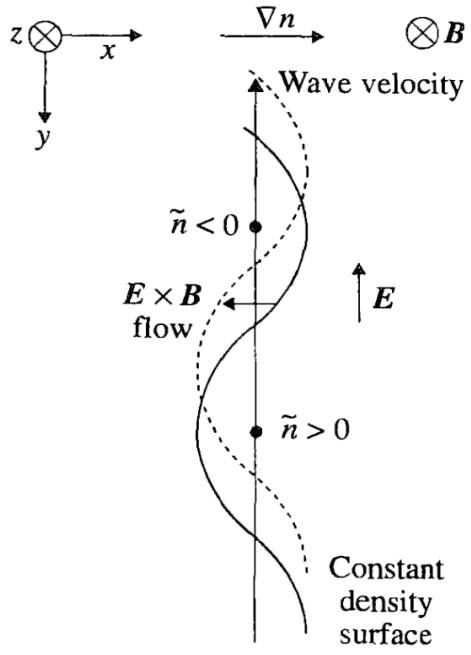

Figure 1.12. Mechanism of drift wave: the perturbed electric field directs from $\tilde{n} > 0$ region to $\tilde{n} < 0$ region. The associated $\mathbf{E} \times \mathbf{B}$ drift enhances the density in the less dense regions and reduces it in the more dense regions, causing the density and potential perturbations to oscillate in time and results in a drift wave propagating in the y direction [10].

mated by $\tau_b \approx L_c^2/D$, where L_c is the radial scale length of fluctuations and D is the diffusion coefficient. When $\tau_c < \tau_b$, the sheared flow reduces the radial scale (correlation length) of the fluctuations, and reduce the level of anomalous transport. This mechanism for reducing turbulent transport was proposed to explain the transition to the high confinement mode (H-mode).

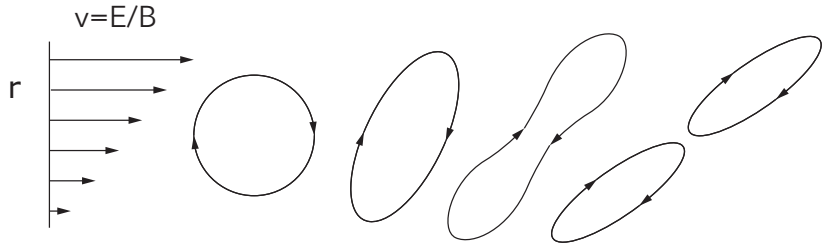

Figure 1.13. Effect of E×B sheared flow on a turbulent convective cell.

Figure 1.13 shows the mechanism of E ×B sheared flow on a turbulent convective cell. The radial force balance [28]:

$$E_r = \frac{1}{Z_i e n_i} \frac{\partial}{\partial r} p_i - u_{\theta i} B_\varphi + u_{\varphi i} B_\theta \tag{1.19}$$

Poloidal and toroidal flows play a crucial role in the development of radial electric fields and in the control of turbulence transport via sheared flows. Large electric field in the transport barrier is sustained by pressure gradient. However, in stellarator the role pressure gradient and mean flows in supporting electric field in high confinement is under investigation. Recent experimental results suggest that mean flow (zonal flow) may play important role. This represent a alternative route to high confinement mode [29].

Several mechanisms can contribute to mean ion flow generation: Reynolds stress, external biasing, injected radio-frequency waves, ion orbit loss, non symmetric transport. Among these mechanism, zonal flow flow general through Reynolds stress is an topic of high interest for fusion community.

1.4.4 Zonal flows

Zonal flow is $E \times B$ flow toroidally (n=0) and poloidally (m=0) symmetric but radially varying electric potential fluctuation with nearly zero frequency. Generation of zonal flow was first predicted by Hasegawa, as a result of inverse energy cascade. The prediction is based on Hasegawa-mima equation. Dual cascade of turbulent spectrum is predicted. This dual cascade is similar to 2D fluid turbulence [23]. Sheared flow can generated by the turbulence itself based on so-called predator-prey model [30]. The sheared flow relates to turbulence through turbulence induced Reynolds stress.

Momentum balance equation for zonal flow generation is given by:

$$\frac{\partial \langle V_\theta \rangle}{\partial t} = -\frac{\partial}{\partial r}\left(\langle \tilde{V}_r \tilde{V}_\theta \rangle - \frac{1}{\rho_m \mu_0}\langle \tilde{B}_r \tilde{B}_\theta \rangle\right) - \mu \langle V_\theta \rangle \tag{1.20}$$

where $\langle \tilde{V}_r \tilde{V}_\theta \rangle$ is Reynolds stress, the electrostatic components of turbulence-induced stress; $\frac{1}{\rho_m \mu_0}\langle \tilde{B}_r \tilde{B}_\theta \rangle$ is Maxwell stress, the magnetic component; $\mu \langle V_\theta \rangle$ is the viscous damping term. The first measurement Reynolds stress and demonstration its capability of driving poloidal flow was done in ISTTOK [31] with Langmuir probe. It was also found Reynolds stress is important in L-H transition [32]. Gyro-kinetic simulation confirms zonal flow generation by turbulence consistent with Hasegawa-Mima theory [33]. The first experimental detection of zonal flow was conducted in CHS [34].

Geodesic acoustic mode (GAM) is a type of zonal flow which was first predict in [35]. The flow structure (or radial electric field) of GAM is symmetric around the magnetic axis, i.e. m=n=0. However, the density fluctuation of GAMs is poloidally asymmetric with m=1, n=0. No significant density fluctuation is expected for stationary zonal flows. The first identification of GAMs was conducted in HL-2A [36]. A review of the theory of zonal flow

can be found in [37]. A review of the progress of zonal flow experiments can be found in [38].

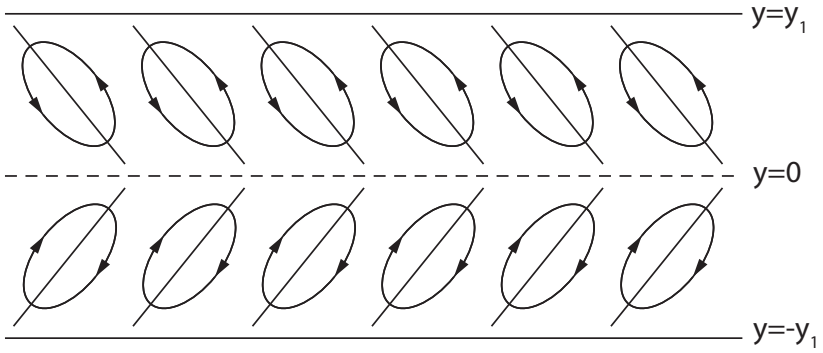

Figure 1.14. Illustration of a flow with some hypothetical pattern producing a convergence of momentum into the mid-channel [39].

Another mechanism for flow generation from turbulent events (structures) is through eddy tilting [40]. The energy exchange between turbulence and mean flow may be interpreted in term of eddy viscosity, which is associated with the momentum flux perpendicular to the mean flow direction [39]. If eddies transfer momentum from the high velocity region to low velocity region, the viscosity is positive and results in a decrease of shear. If the flux on the opposite direction, the turbulent flow exhibits negative viscosity. In this case, energy is transferred from turbulence to the mean flow and increase the shear, thus facilitating sheared flow development. Several conditions are required to achieve negative viscosity [40]. First, eddies which transport the momentum contrary to the gradient of mean flow must have a supply of turbulent kinetic energy. Second, the mean flow should experience some form of braking (e.g. positive viscosity) so that its value does not increase without limit. However, this braking should be low enough to allow the generation of differential rotation. Third, some kind of turbulent irregularity must be present. An illustration of flow generation by turbulence is shown in figure 1.14 [39]. The elliptical circulation and the systematic tilts of their major axes can be expressed as gradients in quadratic terms of fluctuating velocities ($d \left\langle \tilde{v}_i \tilde{v}_j \right\rangle / dr_i$) [40].

Zonal flows and mean sheared flows both have the capability to reduce turbulence. But they are different in scales, mean sheared flows are macroscopic and zonal flows are in mesoscopic scale. Comparison of zonal flow and sheared mean flow is shown in figure 1.15 [7]. Interaction between zonal flow and sheared mean flow has been studied through simulation [41] and experiments [42, 43].

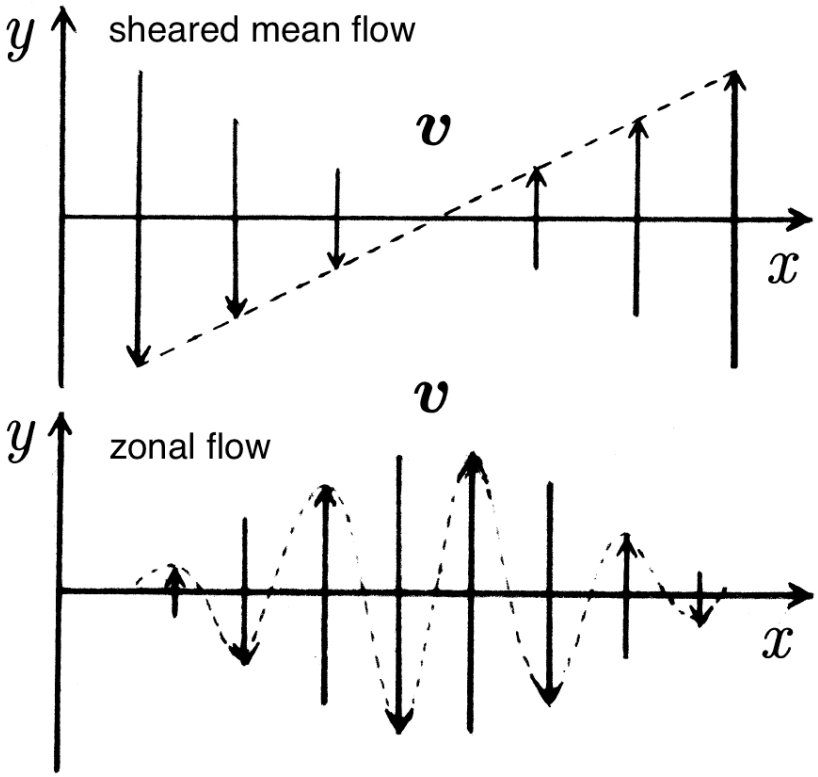

Figure 1.15. Comparison of zonal flow and sheared flow [7].

1.4.5 Isotope effect

In a magnetised plasma, isotope effect is referred to as the contradiction between experimental observation and theoretical prediction on the isotope dependence of plasma confinement. It has been observed in most fusion devices that deuterium-dominated plasmas have an improved confinement against the hydrogen-dominated ones [44]. It has also been observed that the plasma confinement of D-T plasmas is better than D plasmas [45]. Interestingly, isotope effect seems to be weaker in stellarators than in tokamaks [46].

Standard transport theories fail when predicting isotope effect. Classical transport is based on collisions and modelled by random walk, therefore, the step size of transport is Larmor radius. Considering neoclassical theory, the step size is the banana width, which is also proportional to the Larmor radius. Both theories predict deterioration of plasma confinement with increasing isotope mass. More refined theory considering plasma turbulence predicts gyro-Bohm scaling, which is also wrong in predicting isotope effect. This contradiction between the experiments and theories has been a mystery for the fusion community for more than 30 years.

Furthermore, considering the present ITER power capabilities (in the range of 70 MW), a reduction of the L-H power threshold (P_{L-H}) with ion mass (D vs. H) would have great

impact on ITER plasma operation scenarios. The P_{L-H} power threshold deduced from empirical scaling laws is sufficient to define the minimum P_{input} required for ITER operation. Experimental studies have shown a reduction of the L-H power threshold by about 50% when using Deuterium and He instead of Hydrogen [47]. Thus, better understanding of the dependence of the L-H power threshold on isotope mass is urgently needed to improve our confidence in ITER scenarios.

Therefore, two different approaches have been explored to investigate and understand ion mass dependences of confinement and transport (table 1.1) [29]:

An engineering approach use of empirical control parameters like ion mass and magnetic configuration to get the optimum plasma conditions for achieving the minimum L-H power threshold in ITER and confinement optimisation.

A basic physics approach basic understanding of underlying mechanisms including: Role of ion mass on turbulence (Gyro-Bohm-like scaling), role of ion and electron transport channels, interplay between long (neoclassical) and short scale (turbulent) radial electric fields, stability and role of plasma profiles and Z_{eff}, influence of ion mass on zonal flows and GAMs and role of atomic physics mechanisms. Studies in tokamaks and stellarators have provided experimental evidence for the importance of multi-scale physics to unravel the impact of the isotope effect on transport.

1.4.6 Impurity transport

Particle and impurity transport are usually described empirically in terms of diffusive and convective terms driven by neoclassical and turbulence mechanisms. In the framework of neoclassical mechanisms in tokamaks, the main ion density gradient (inwards) and the ion temperature gradient (outwards at low collisionality, otherwise known as temperature screening) are responsible for opposite convective fluxes. In non-axisymmetric devices the sign of the radial electric field is expected to play a dominant role in the convection of impurities. Thus, by standard neoclassical theory, high inward radial electric fields are foreseen to enhance inward impurity convection in stellarators. As a consequence high density (ion root operation) shows a tendency for impurity accumulation [63]. Interestingly, efficient impurity control has been achieved in non-axisymmetric plasma regimes with inwards radial electric field in high-density H-mode plasmas in the W7-AS stellarator [64] and in the so-called impurity hole regime in the LHD helical device [65]. In both cases the underlying mechanisms remain unknown. Those results show that, indeed it is possible the simultaneous achievement of improved energy confinement with low impurity accumulation which is a necessary condition for the development of fusion reactor relevant scenarios.

Table 1.1. Approaches to investigate and understand ion mass dependences of confinement and transport in tokamaks and stellarators [29].

Isotope effect: transport and L-H transition	**Approach and Validation (tokamaks vs stellarators)**
Empirical actuators - Ion mass (H/D/He) - Magnetic configuration - Perturbative effects	• *Key empirical question:* What are the optimum configuration and plasma conditions for achieving minimum L-H power threshold in the ITER non-nuclear / nuclear phases? - ITPA scaling laws - Tokamak vs Stellarators, RMPs, X-point location - e.g. MHD effects
Towards basic understanding	• *Role of ion mass on turbulence:* Gyro-Bohm-like scaling in tokamaks [48] and stellarators[49]. • *Transport:* Ion vs electron transport [50]. • *Interplay between neoclassical and anomalous mechanisms:* Role of neoclassical E_r and interplay with short radial scale E_r in tokamaks [43] and stellarators [51–53, 42]. • *Stability:* Pedestal stability can be affected via a relative shift of temperature and density profiles [54] and role,of Z_{eff} [55]. • *Role of ion mass on Zonal Flow (ZF) and GAMs:* Amplitude of large-scale flows vs ion mass in tokamaks [56, 57] and stellarators [49, 58]. GK simulations [59, 60]. • *Role of atomic physics:* Boundary conditions (ionization/charge exchange) [61, 62]

Significant progress has been reported regarding the physics understanding of empirical actuators, like ECRH / ICRH core heating, to avoid impurity accumulation, including the following mechanisms:

- A reduction of the background density gradient, leading to a reduction of the inward (neoclassical) convection of impurities in tokamaks and stellarators.
- An increase of turbulence level in both tokamaks [66] and stellarators [67].
- The amplification of core temperature screening, which would be relevant in core α-heating regimes in tokamaks.
- Modification of the neoclassical radial electric fields in stellarators.

- The development of core plasma potential flux surface asymmetries which due to its 3D structure is expected to be stronger in stellarators than in tokamaks.

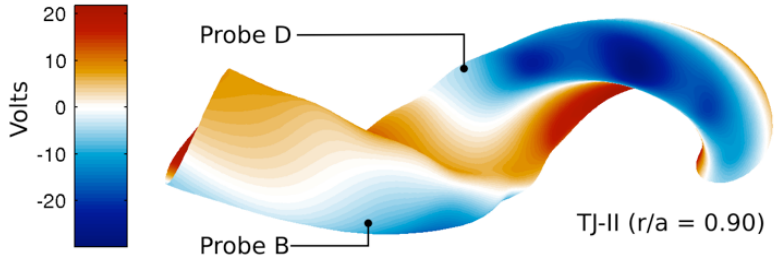

Figure 1.16. Simulation of potential asymmetry in ECRH plasma in TJ-II [68].

It has been predicted that impurity accumulation is affected by 3D asymmetries [69]. Direct experimental observations of electrostatic potential variations within the same magnetic flux surfaces have been reported both in electron and ion root regimes in the TJ-II stellarator [68, 70]. Significant asymmetries are observed in electron-root wave-heated plasmas, which are reduced in ion-root beam-heated conditions and when the electron temperature decreases. The order of magnitude (in the order of tens of volts) as well as the observed dependencies on the electric field root are well reproduced by neoclassical Monte Carlo calculations figure 1.16 , thus improving confidence in impurity transport predictions. More recently, we have investigated the simultaneous matching of potential profiles and the amplitude of potential modulation induced by biasing in ion-root plasma regimes, concluding that plasma potential asymmetries are ubiquitous in the TJ-II stellarator. It remains an open question how these regimes extrapolate to plasmas with higher temperatures and lower collisionality.

The unique capabilities of the dual HIBP system allows the investigation of multi-scale mechanisms to be expanded from the plasma edge to the plasma core in the TJ-II stellarator. Experiments with combined NBI and ECR heating have shown direct experimental evidence of the influence of ECRH on turbulent mechanisms, increasing both the level of fluctuation and the amplitude of Long-Range-Correlations (LRC) as proxy of Zonal Flows for potential fluctuations but not for density and poloidal magnetic fluctuations as well as affecting neoclassical radial electric fields. Whereas ECRH influences the level of fluctuations in a wide range of plasma densities, ECRH induced reversal of the neoclassical radial electric field has been observed only in low-density plasmas [67].

Part II

Methodology

Chapter 2

Experimental methods

This chapter includes introduction to the fusion devices TJ-II stellarator, ISTTOK tokamak and RFX-mod reversed field pinch, and probe diagnostics.

2.1 Experimental setup in TJ-II

TJ-II is a four-period helical-axis stellarator (also called heliac) with an average major radius of $\langle R \rangle = 1.5m$ and average minor radius of $\langle a \rangle \leq 0.22m$. TJ-II is located at CIEMAT in Madrid and started operation in 1997.

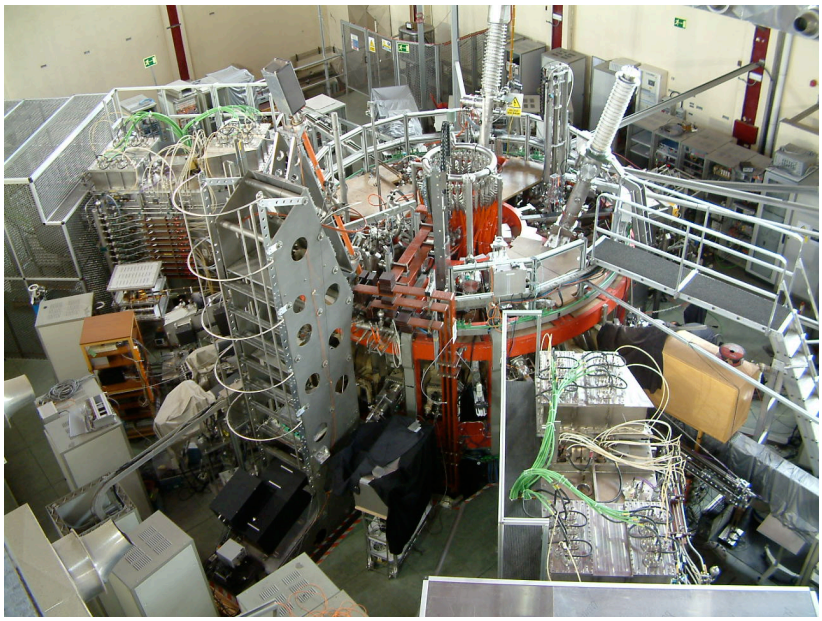

Figure 2.1. Top view of TJ-II

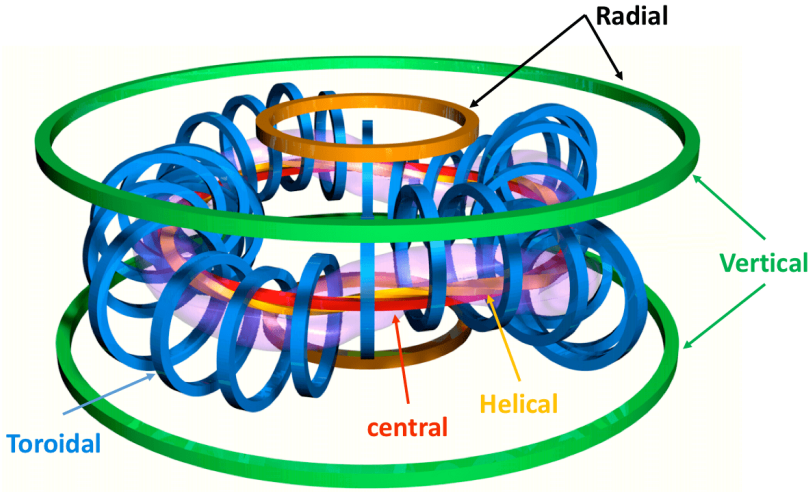

Figure 2.2. TJ-II Coil system. Red: central coils. Yellow: helical coil. Blue: 32 toroidal coils. Green: vertical coils. Brown and green: radial coils. (Adapted from FusionWiki)

Figure 2.2 shows the coil system of TJ-II. The toroidal field is created by 32 toroidal coils. An important feature of TJ-II is that it equips with a toroidally directed central coil closely fitted with a $l = 1$ winding helical coils. Separately controllable currents in the hard core windings gives the device its unique flexibility to vary the rotational transform, shear and magnetic well in a wide range. The main helical field is produced by the central coil (CC), helical coil (HX), and TF coils. The vertical field coils (VF) allow positioning the magnetic axis. The magnetic configuration is defined by the currents flowing through the coils CC, HX, and VF, usually labelled as $I_{CC}\_I_{HX}\_I_{VF}$ (in 100 A). The TJ-II main parameters are summarised in table 2.1.

TJ-II uses two methods for heating: Electron Cyclotron Resonance Heating (ECRH) and Neutral Beam Injection (NBI). The ECRH system includes two gyrotrons heating with $f = 53.2$ GHz 2nd harmonics X-mode polarisation and power of $P_{ECRH} = 2 \times 300$ kW. The NBI system has two injectors and provides power of $P_{NBI} = 2 \times 1$ MW (co and counter 700 kW port-through at 33 kV). In TJ-II the ECRH plasma can usually reach the plasma density $n_e \sim 1 \times 10^{19}$ m^{-3} and $T_e \simeq 1$ keV. The NBI plasma can reach $n_e \sim 4 \times 10^{19}$ m^{-3} and $T_e = 250 - 300$ eV.

2.2 Experimental setup in ISTTOK

ISTTOK is a small-size, large aspect ratio circular cross-section tokamak with a poloidal graphite limiter and an iron core transformer [72]. It has a major radius of 46 cm and a minor radius of 8.5 cm, and can reach maximum toroidal magnetic field of 2.8 T. ISTTOK is

Table 2.1. TJ-II parameters [71]

Design parameters	
Major radius	1.5 m
Average magnetic field	1 T
Number of periods	4
Number of TF coils	32
TF coil radius	0.425
TF coil swing	0.2825 m
TF coil current (nominal 1 T)	234 kA
l=1 helical coil swing	0.07 m
VF coil radius	2.25 m
VF coil height	+0.75
Maximum I_CC	-280 kA
Maximum I_HX	-200 kA
Maximum I_VF	200 kA
Calculated Ranges	
Range of rotational transform at magnetic axis	0.96~2.5
Range of plasma average radius	0.10~0.25 m
Shear range	-1~10 %
Magnetic well depth range	0~6

located at Instituto Superior Técnico (IST) in Lisbon and stated operation in 1991. A picture of ISTTOK is shown in figure 2.3. The parameters of a typical discharge in ISTTOK are shown in table 2.2.

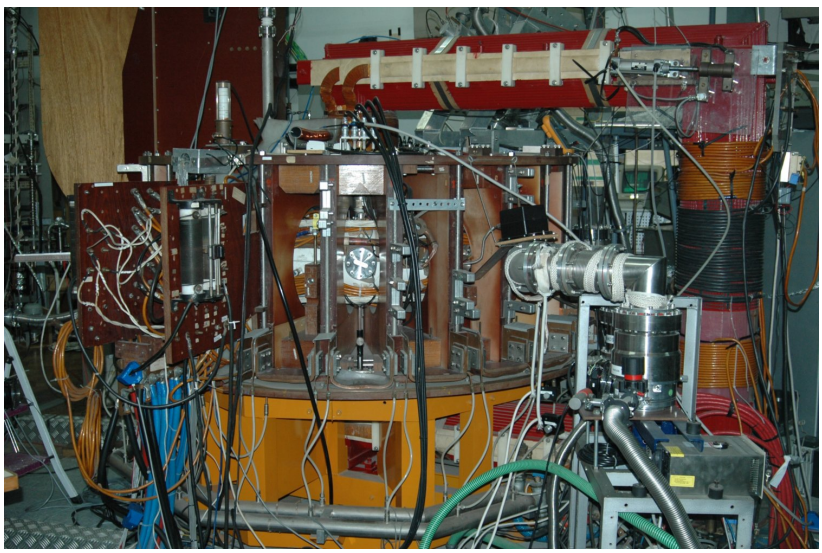

Figure 2.3. ISTTOK tokamak

Table 2.2. ISTTOK discharge parameters

Parameters		Values
Plasma current		$\sim 7\,kA$
Discharge duration		$\sim 45\,ms$
Plasma density at r=0		$\sim 5 \times 10^{18}\,m^{-3}$
Electron temperature at r=0		~120 eV
C^{III} ion temperature at r=0		$\sim 100\,eV$
Energy confinement time		$\sim 0.8\,ms$
Beta at r=0		$\sim 0.6\%$
Safety factor	q(0)	~ 1
	q(a)	~ 5

2.3 Experimental setup in RFX-mod

The **R**eversed **F**ield e**X**periment *modified* (RFX-mod) [73] is the largest reversed field pinch device presently in operation. A picture of RFX-mod is shown in figure 2.4. RFX-mod is located at Consorzio RFX in Padova and started operation in 2004. The main parameters of RFX-mod are shown in table 2.3. In RFX-mod, plasma is heated with purely ohmic heating, as in all RFPs.

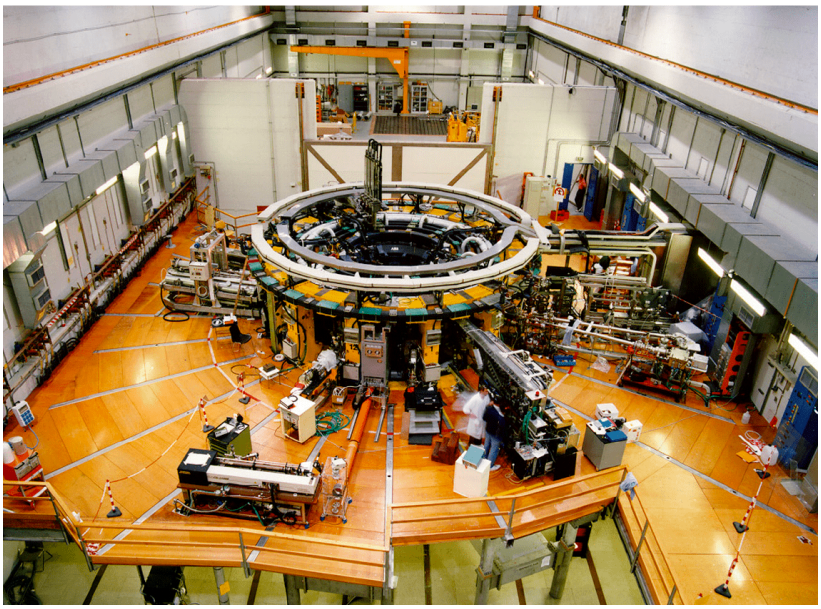

Figure 2.4. Top view of RFX-mod

RFX-mod is an upgrade of the previous RFX device [74]. The goal of the modification is to improve and introduce a new active control of the MHD modes. There are two main upgrades. First, introduced a new feedback control system. The system mainly consists of

192 (4 poloidal × 48 toroidal) independently power saddle coils which completely surrounds the toroidal surface (figure 2.5). On the surface magnetic probes are installed to measure magnetic fields for the feedback control purposes. Second, the old 65 mm thick aluminium shell has been replaced by a close fitting 3 mm copper shell, as indicated in figure 2.5(a). This change shortens the magnetic field penetration time from 450 ms to 50 ms, which now is much shorter than the discharge duration time (∼0.5 s) and makes the feedback control possible.

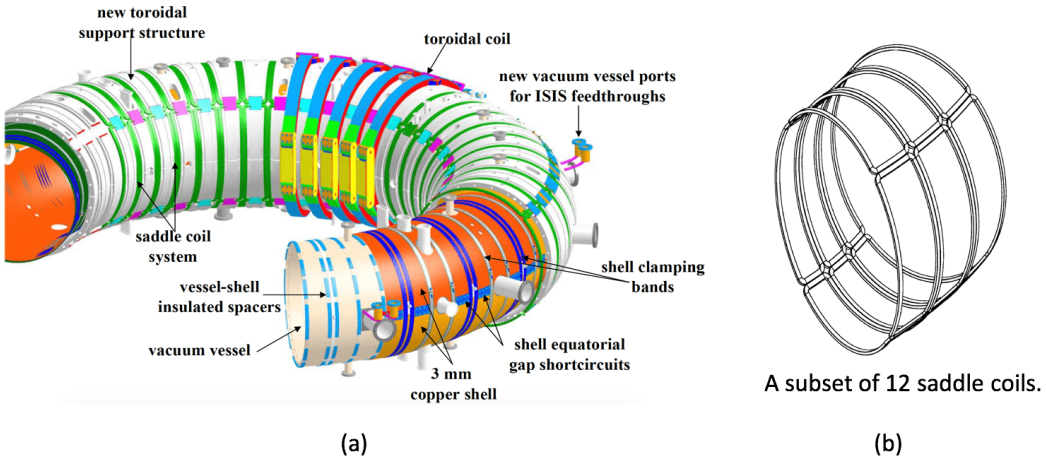

Figure 2.5. Coil system of RFX-mod

Table 2.3. Main parameters of RFX-mod

Parameters	**Values**
Major radius	2 m
Minor radius	0.459 m
Toroidal magnetic field	<0.7 T
Plasma current	<2 MA
Discharge duration	<0.5 s
Plasma density	$\sim 5 \times 10^{19}$
Maximum electron temperature	1.3 keV

By the control of the radial magnetic fields at the edge, plasma current in RFX-mod can reach up to 2 MA. At such high current, spontaneous transition from the multiple helicity (MH) state to quasi-single helicity (QSH) state through self-organisation has been observed in RFX-mod [75]. This transition represents a new paradigm for achieving chaos-free plasma in RFP.

The flexibility of the feedback control system also allows RFX-mod to run as a low-current ($I_p \leq 0.15$ MA) Ohmic tokamak [76].

2.4 Probe diagnostics

Langmuir probe is a widely used fundamental plasma diagnostics, named after its inventor Irving Langmuir. The Langmuir probe measurement is made basically by inserting a small metallic electrode or a wire into a plasma. The probe can be biased at various voltages positive or negative relative to the plasma through a power supply. Then the plasma properties (density, potential and temperature) can be extracted from the current-voltage characteristic collected by the probe. One advantage of probe diagnostics over other techniques is that the probe measurements are local. This allows the probe to achieve high spatial and temporal resolution and makes it suitable for plasma turbulence study. A price paid for the local measurements (direct contact with plasmas) is that the accessibility of the probe to a plasma is limited by the conditions in which the probe can survive. The probe measurements are available for plasma of temperature $T_e < 100$ eV.

2.4.1 Langmuir probe theory

When plasma is in contact with a solid surface, the electrons and ions hit the surface with thermal speed and tend to stick to it. Because the electron thermal velocity is higher than that of ions, initially more electrons reach the solid surface than ions and the surface is charged negatively. Negative potential is built on the surface which repels electrons and draws ions. After reaching a balance, a positive charged layer, called sheath, is formed around the solid surface. In the bulk plasma, the condition of quasineutrality ($n_e \approx n_i$) is valid, while in the sheath region it is not valid ($n_i > n_e$) and strong electric field arises. The electric field is related to the ion and electron density through Gauss's law, $\nabla \cdot \mathbf{E} = \frac{e}{\epsilon_0}(n_i - n_e)$. With $\mathbf{E} \equiv -\nabla\phi$, we obtain 1D Poisson's equation:

$$\frac{d^2\phi}{dx^2} = -\frac{e}{\epsilon_0}(n_i - n_e) \tag{2.1}$$

Figure 2.6 shows the electric potential variation near the probe surface. We take the potential inside the plasma as a reference, i.e. $\phi_\infty = 0$. The potential and density at the sheath edge are denoted as ϕ_{se} and n_{se}. Assume the electrons are Maxwellian in the sheath. Then the electron density $n_e(x) = n_{se}\exp[e(\phi - \phi_{se})/kT_e]$. The potential on the probe is $\phi_{pr} = \phi(0)$. Assume ion temperature $T_i = 0$, originated at a single point and with zero velocity. From energy and particle conservation, we can obtain the ion density, $n_i = n_{se}(\phi_{se}/\phi)^{1/2}$.

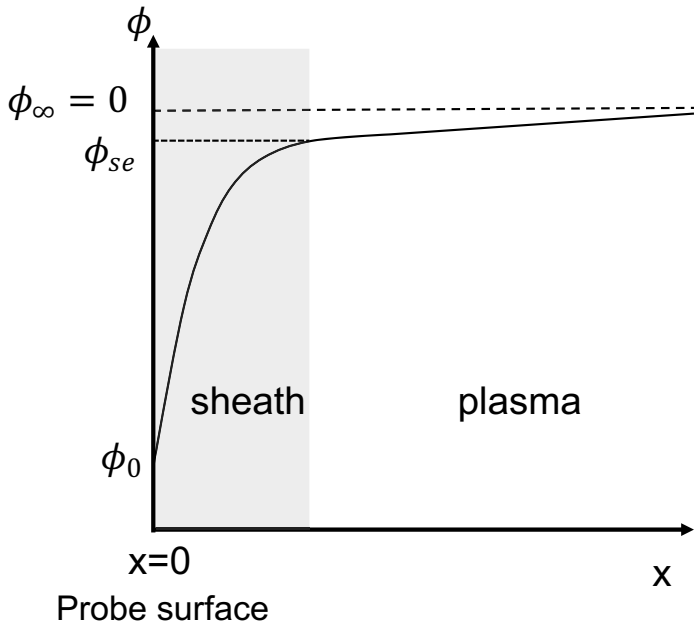

Figure 2.6. Schematic of the electric potential variation near the probe surface.

Substituting these two terms into the Poisson equation, we get,

$$\frac{d^2\phi}{dx^2} = -\frac{e}{\epsilon_0} n_{se} \left[\left(\phi_{se}/\phi \right)^{1/2} - \exp\left[e\left(\phi - \phi_{se} \right) / kT_e \right] \right] \tag{2.2}$$

Considering the region just inside the sheath, we define $\Delta = \phi_{se} - \phi > 0$ and expand the two terms in the right-hand side of the equation (2.2) up to the first-order term. The Poisson equation becomes:

$$\frac{d^2\Delta}{dx^2} = -\frac{e\Delta}{\epsilon_0} n_{se} \left[\frac{e}{kT_e} - \frac{1}{2\left|\phi_{se}\right|} \right] \tag{2.3}$$

Exponential (physically meaningful) solution requires $\frac{e}{kT_e} \geq \frac{1}{2|\phi_{se}|}$, which implies $m_i v_{se} \geq kT_e$. This results in Bohm's criterion for the exit velocity:

$$v_{se} \geq c_s = \left(\frac{kT_e}{m_i} \right)^{1/2} \tag{2.4}$$

The solution also gives a rough estimation of the sheath thickness of the order of the Debye length [77]:

$$L_{sheath} \approx \sqrt{\frac{\epsilon_0 k T_e}{e^2 n_{se}}} \equiv \lambda_{Debye} \tag{2.5}$$

A improved analysis shows that the sheath is about 15-30 Debye length [78]. Sheath thickness is an important parameter for building multiple-tip probe. The distance between two probe tips should be large enough to avoid sheath overlapping.

The probe signal is related to the electron and ion flux to the probe surface. The electrons are Maxweillian and the unidirectional flux can be estimated as $\Gamma_e = \frac{1}{4} n_{se} \bar{c}_e \exp(e\phi_{pr}/kT_e)$, where the 1/4 comes from averaging over solid angle and $\bar{c}_e = (8kT_e/\pi m_e)^{1/2}$ is the average electron thermal speed. The ion flux to the probe is $\Gamma_i = n_{se} c_s$. When the two fluxes reach a balance, i.e. $\Gamma_i = \Gamma_e$, the net current to the probe disappears. In this case, the potential on probe is called floating potential ϕ_f. From balance between the electron and ion flux, the relation between floating potential ϕ_f and plasma potential ϕ_p is obtained as:

$$\phi_f = \phi_p - \alpha T_e \,, \qquad \alpha = 0.5 \ln \left[\left(2\pi \frac{m_e}{m_i} \right) \left(1 + \frac{T_i}{T_e} \right) \right] \tag{2.6}$$

For a hydrogen plasma, $\alpha \approx 3$. Usually this value should be determined experimentally, because the electron saturation current may be reduced in the presence of magnetic field.

If the probe is biased by an external power supply, the electron flux is still based on Maxewllian distribution, while the ion flux is dependent on the sheath flux, no matter the probe is biased or not. The ion flux is given by

$$\Gamma_i = n_{se} c_s = \frac{1}{4} n_{se} \bar{c}_e \exp(e\phi_f / kT_e) \tag{2.7}$$

The total current density drawn by probe is the sum of the ion and electron currents:

$$j = e\left(\Gamma_i - \Gamma_e\right) = \frac{1}{4} n_{se} \bar{c}_e \left[\exp\left(e\phi_f / kT_e\right) - \exp\left(e\phi_{pr} / kT_e\right) \right] \tag{2.8}$$

Considering the pre-sheath density drop $n_{se} = n_0/2$,

$$j = e \frac{n_0}{2} c_s \left\{ 1 - \exp\left[e\left(\phi_{pr} - \phi_f\right) / kT_e \right] \right\} \tag{2.9}$$

When the probe is biased with very negative voltage, the electron collection goes to zero, only ions collected, and $\exp\left[e\left(\phi_{pr} - \phi_f\right)\right] / kT_e \sim 0$. This gives the measurement of ion saturation current:

$$I_{sat} = A_p j_{sat} = \frac{1}{2} A_p e n_0 c_s \tag{2.10}$$

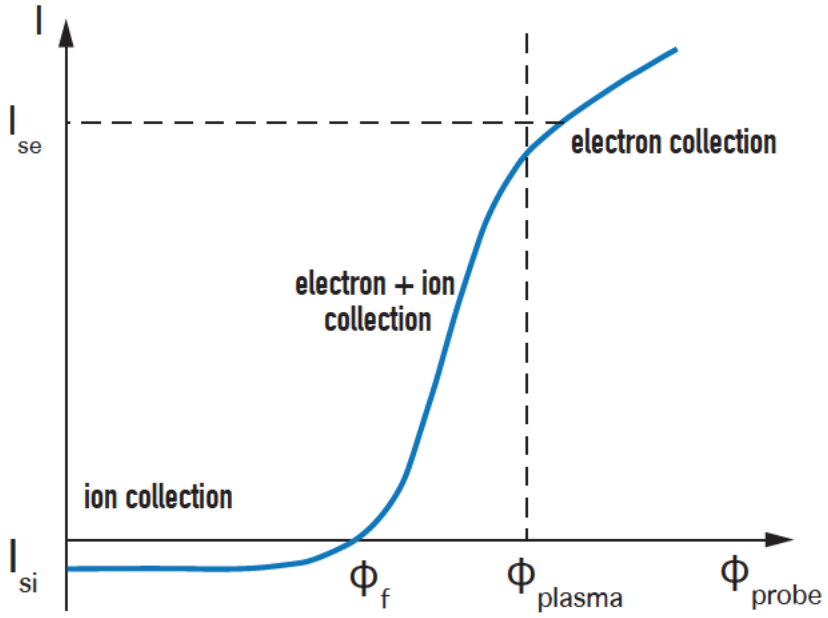

Figure 2.7. Typical Langmuir probe characteristic curve

where A_p is the particle collection area of the probe. In general, with various biasing voltage, the current collected is expressed as:

$$I_{probe} = I_{sat}\left[1 - \exp\left(e(\phi_{pr} - \phi_f)/kT_e\right)\right] \tag{2.11}$$

A typical Langmuir probe characteristic curve showing different probe operation regions is illustrated in figure 2.7.

2.4.2 Langmuir probe measurements

Langmuir probe is a flexible and versatile plasma diagnostic. Operating with sweeping bias voltage, we can obtain a I-V characteristic curve; fitting the I-V curve gives the estimation of electron temperature T_e. With constant bias voltage, average values and fluctuations of ion saturation current I_s and floating potential ϕ_f can be measured, which relates to electron density n_e and plasma potential ϕ_p. Thus probe has potential to measure the electrostatic properties (n_e, ϕ_p, T_e) and their fluctuations. Probe can be built with various configuration by the combination of probe tips measuring basic plasma properties. The time resolution probe is limited by its cutoff frequency, $f_{cut} = 1/2\pi R_{sheath}C_{stray}$, where R_{sheath} is the sheath resistance, C_{stray} is the stray capacitance, and in TJ-II, the cut-off frequency can reach $f_{cut} > 1\,\text{MHz}$. The spatial resolution is limited by the sheath thickness, such that two probe tips should separated far enough to avoid sheath overlapping. For a typical fusion edge

plasma, the spatial resolution can reach below 2 mm. This makes Langmuir probe a suitable diagnostic for characterising turbulent transport and structures. The probe measurements with various configuration and basic statistical analysis are summarised below.

Single point A single probe tip The simplest configuration is with a single probe tip. In sweeping mode, it can measure the electron temperature. With fast sweeping, it may even provide some measurements of fluctuations. At constant bias voltage, both average values and fluctuations of ion saturation current I_s and floating potential ϕ_f can be measured, which provide estimations electron density n_e and plasma potential ϕ_p. In principle, probe has potential to measure the electrostatic properties (n_e, ϕ_p, T_e) and their fluctuations.

Statistical analysis of fluctuation is important for the study of plasma turbulence. The standard linear power spectrum analysis is commonly used for analysing the distribution of fluctuation power over frequencies. Empirical similarity in spectra of density and potential fluctuations has been found over different configurations [79]. Power spectrum analysis does not provide information on the nonlinear effect of phase coupling between different waves. The nonlinear interaction can be analysed using the bicoherence method [80]. Experimental evidence of three-wave coupling has been found in [81]. If there are intermittent or bursty events in edge turbulence, wavelet analysis is more helpful for detecting the intermittency [82]. For the study of self-similarity and memory effect in plasma turbulence, Hurst exponent has been introduced [83].

Two points Biasing two probe tips with respect to each other, a double probe is formed [84]. A double probe is a improved method to measure electron temperature with sweeping mode. The entire system is floating and no ground is needed for the bias. The I-V characteristic of the double probe is: $I = I_s \tanh(V/T_e)$.

With two points measuring both floating potentials or ion saturation currents, two-point correlation[85] can be used for the analysis of phase velocity, wavenumber and correlation length. Assume the distance of the two tips is Δx and the phase difference between the fluctuations measure by two probe tips. The phase difference can provide an estimation of wavenumber $k = \Delta\varphi/\Delta x$. In frequency domain, we can calculate the fluctuation power in the wavenumber-frequency space $S(k, \omega)$. The phase velocity is estimated by weighting ω/k with the spectral density function:

$$v_\theta = \frac{\sum_{k,\omega} (\omega/k) S(k,\omega)}{\sum_{k,\omega} S(k,\omega)} \tag{2.12}$$

The $S(k,\omega)$ weighted wavenumber and frequency can be obtained in a similar way.

Two-point correlation also gives an estimation of the frequency resolved correlation length (L_c) through the turbulent broadening of the wavenumber, spectral width $\sigma_k(\omega)$:

$$\sigma_k(\omega) = \left[\frac{\sum_{k,\omega} (k - \bar{k}(\omega))^2 S(k,\omega)}{\sum_{k,\omega} S(k,\omega)} \right]^{1/2} \qquad \text{and} \qquad L_c(\omega) \equiv \left[\sigma_k(\omega)\right]^{-1} \tag{2.13}$$

It should be noted that the inverse proportion of σ_k to the correlation length does not make physical sense in the presence of simultaneous co- and counter-propagation of waves which implies the phase velocity of ≈0. For the analysis of correlation length, we may need to remove the parts with $v_{ph} \approx 0$ [86].

Three points A standard triple probe [87] is basically the combination of a floating potential ϕ_f and a double probe configuration. In the double probe configuration, the positively biased tip measures potential (ϕ^+) and the negatively biased tip measures ion saturation current I_s. An important feature of a triple probe is that it allows instantaneous measurements (fluctuations) of electron temperature:

$$T_e = \frac{\phi^+ - \phi_f}{\ln(2)} \tag{2.14}$$

Although this measurement of T_e is fast, we should be aware that the measurement is non-local because the estimation is based on the measurements from two separated probe tips. A small spatial variation may cause phase shift between the two probe tips. Both phase and amplitude of the measurement of T_e fluctuations can be affected by this phase error, and thus having an significant impact on the measurements of heat flux with probe. Modified triple probes have been proposed to reduce the phase delay errors [88, 89].

When three tips in poloidal direction are set such that the middle tip measures I_s and the other two measure ϕ_f, the probe is able to measure the turbulence-induced particle flux:

$$\Gamma_r = \langle \tilde{n}_e \tilde{v}_r \rangle = \left\langle \tilde{n}_e \tilde{E}_\theta \right\rangle / B_\phi \tag{2.15}$$

where poloidal electric field fluctuation is estimated as $\tilde{E}_\theta \approx (\tilde{\phi}_{f1} - \tilde{\phi}_{f2})/d_\theta$ and d_θ is the poloidal separation of signals ϕ_{f1} and ϕ_{f2}. Normalised the flux with elec-

tron density, effective velocity of particle transport is: $V_{\text{eff}} = \left\langle \tilde{n}_e \tilde{E}_\theta \right\rangle / (n_e B) = \left\langle \tilde{I}_s \tilde{E}_\theta \right\rangle / (I_s B)$.

Another important quantity is the turbulence-induced heat flux, which is expressed as the sum of convective and conductive terms [90]:

$$Q_r = Q_{conv} + Q_{cond} = \frac{3}{2} T_e \Gamma_r + \frac{3}{2} \frac{n_e \left\langle \tilde{T}_e \tilde{E}_\theta \right\rangle}{B_\phi} \tag{2.16}$$

As has been discussed before, the most critical issue for the estimation of heat flux is the accurate measurements of T_e fluctuations.

Multiple points A probe can built in a 2D configuration with multiple measurements in both poloidal and radial direction. This configuration may be able to measure simultaneously the poloidal and radial electric field fluctuations ($\tilde{E}_r$ and $\tilde{E}_\theta$) at same point. From these measurements, Reynolds stress can be estimated [31]:

$$\text{RS} = \langle \tilde{v}_r \tilde{v}_\theta \rangle = \left\langle \tilde{E}_r \tilde{E}_\theta \right\rangle / B^2 \tag{2.17}$$

In this estimation, the fluctuations of E_r and E_θ should be calculated for the same point to avoid the phase shift.

In a rake probe configuration, multiple tips can be used to estimate the correlation length in edge plasma turbulence [49]. Usually, one of the probe tip is taken as the reference. By the correlation functions between the reference signal and signals measured by all rake probe tips. A spatial correlation function can be obtained. The decay length of the correlation function provides an estimation of the correlation length.

Dual probe system By installing similar probes in two distant locations in a device, a dual probe system is built. With this system, plasma properties at large scale can be studied by adjusting the radial positions of the two probes properly and measuring the fluctuations and average values measured two distant locations. The similarity of fluctuations is quantified by long-range correlation (LRC) [51, 91, 92, 56, 49], which is a standard to detect and characterisation of large coherent structures (zonal flows and GAMs) in a plasma turbulence. Comparison of the mean values of potential measurements at two poloidal/tporoidal separated positions on the same magnetic surface provides a measure of potential the asymmetries in plasma [68, 70], which is an important aspect of the study of impurity transport.

All the measurements introduced above can be made at a fixed position or through a reciprocating driving system to move the probe fast in and out of the plasma during a dis-

charge. Figure 2.8 shows the photos of two of Langmuir probe heads installed in TJ-II and the schematic of reciprocating system [93].

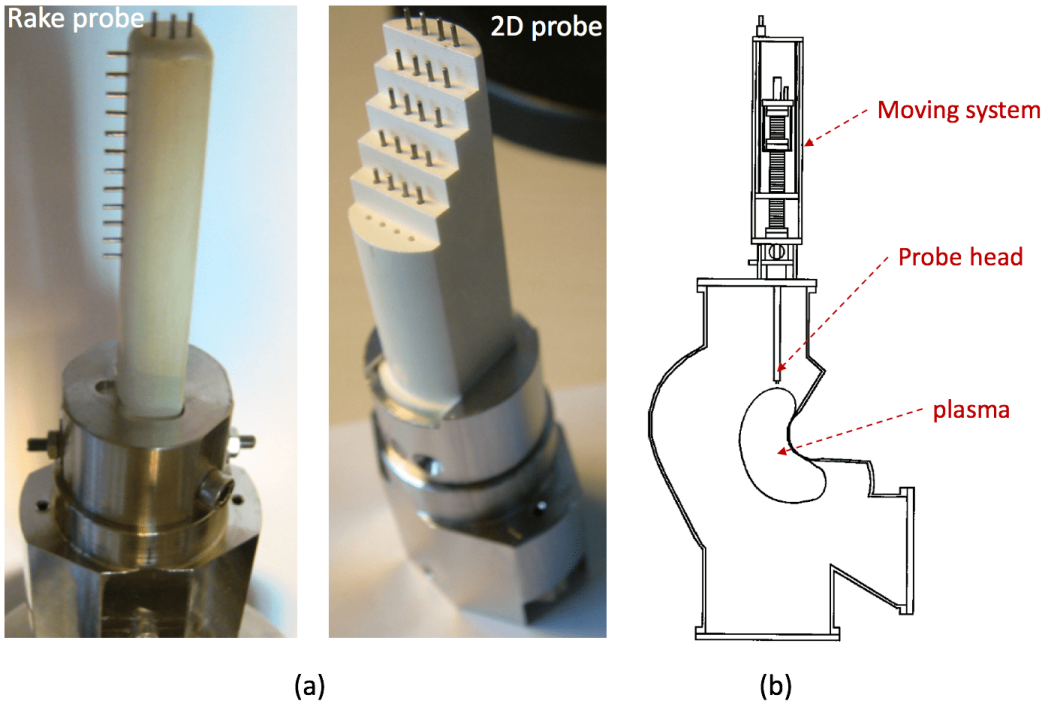

Figure 2.8. (a) Two examples of probe heads installed in TJ-II; (b) schematic of the probe installed in the reciprocating system [93].

In TJ-II, the reciprocating system mainly includes two parts [93]: a removable probe head and a displacement system which enables the probe to be displaced in vacuum. The probe displacement system has two components: a slow one (course length $\leq 0.8\ m$) to set the probe at the initial measurement position, and a fast one (run length $= 0.1\ m$) to obtain the desired measurements within an adjustable time interval during the plasma discharge. The spatial resolution of the radial movement is about 1 mm. The fast displacement (up to 1.7 m/s) is achieved by using a pneumatic system.

ISTTOK is also equipped with a dual probe system. The probe configurations are similar to the probes installed in TJ-II. Both probes can be moved radially on shot-to-shot basis.

2.4.3 Electromagnetic probe

A more advanced probe system is the electromagnetic probe, which measures the electrostatic and magnetic properties simultaneously. Figure 2.9 shows the pictures of the electromagnetic probes: the 'U-probe' installed in RFX-mod [94] and the 'Vorticity probe' installed TJ-II [94, 95]. In both probes, the magnetic measurements are made by a group of three-axial

pick-up coils. Each coil allows measurements of time derivative of magnetic field in three directions. The U-probe consists of two fingers separated in the perpendicular direction. In each finger, an array 5×8 Langmuir probe tips are installed to measure electrostatic properties, and a radial array of 7 magnetic coils spaced 6 mm are arranged inside. This probe has been used for the measurements of parallel current density associated to filaments [94]. The vorticity probe has an Langmuir probe array installed in the middle and the three magnetic probes forming a right angle in the radial-poloidal plane. As its name suggests, this probe can measure the vorticity in turbulence. With the measurements of electrostatic and magnetic fluctuations, both probe can also provide measurements of Reynolds stress ($\propto \left\langle \tilde{E}_r \tilde{E}_\theta \right\rangle$ for tokamak or stellarator, and $\left\langle \tilde{E}_r \tilde{E}_\phi \right\rangle$ for RFP) and Maxwell stress ($\propto \left\langle \tilde{B}_r \tilde{B}_\theta \right\rangle$ for tokamak or stellarator, and $\left\langle \tilde{B}_r \tilde{B}_\phi \right\rangle$ for RFP).

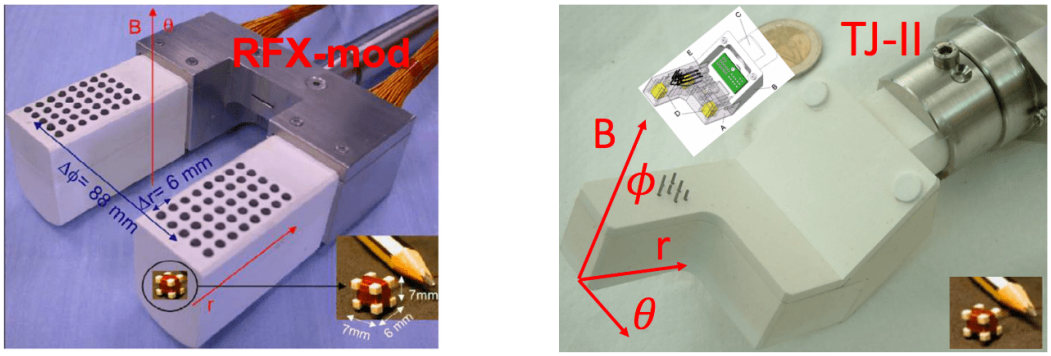

Figure 2.9. Electromagnetic probes: (a) U-probe in RFX-mod [94] and (b) Vorticity probe in TJ-II [94, 95]

2.5 Biasing electrode in TJ-II

Electrode biasing is a technique for externally modifying the edge electric field. When an biased electrode (with respect to wall or limiter) is inserted into the plasma edge, radial electric fields are induced by cross-field currents, according to the $J \times B$ force balance.

Electrode biasing experiments play an important role in the demonstration of the causality relation between radial electric and transport barrier formation [96]. Further analysis of the biasing current-voltage characteristic can provide a way of studying the mechanism of transport barrier formation [97, 98].

In TJ-II, a 2D carbon composite mushroom-shaped electrode (12 mm high with a diameter of 25 mm) has been installed [99]. The electrode is screwed to a stainless steel shaft, which is protected by boron nitride as insulating material to be exposed to the plasma. The

electrode is manipulated by a fast reciprocating probe drive. It can be biased (up to 350 V) with respect to the wall or one of the two limiters located in the Scrape-Off Layer region (about 0.5 cm beyond the LCFS). The electrode can run in DC, DC+AC mode. Various shapes of waveform can be used for the biasing voltage, for example, sine, triangular and square. The frequency of the waveform can be in the region 1-800 Hz, with resolution of 1 Hz.

Part III

Experimental results

Chapter 3

Isotope effect physics, turbulence and long-range correlation studies in the TJ-II stellarator *

The impact of isotope mass on the radial correlation length (L_r) and long-range correlation (LRC) of plasma turbulence has been investigated in Electron Cyclotron Resonance Heated (ECRH) low-density deuterium-hydrogen plasmas in the TJ-II stellarator. We find that the L_r increases with deuterium/hydrogen (D/H) ratio. However, the amplitude of LRC decreases slightly with D/H ratio, in contrast to previous results in tokamak plasmas [Y. Xu et al., Phys. Rev. Lett. **110**, 265005 (2013)]. These findings show the impact of the isotope effect on both the largest scales (LRC determined by the size of the device) and the characteristic radial scale of turbulent structures.

3.1 Introduction

Understanding the mechanism of plasma confinement scaling with isotope mass has been a long-standing open issue in magnetic fusion research. It has been observed in most tokamak experiments that the plasma confinement time increases with increasing ion mass under similar plasma conditions [44]. However, standard transport theories fail when predicting the isotope effect. According to diffusive-like transport theories, the diffusivity is $D \propto L_r^2/\tau_c$, where L_r is characteristic radial scale length, τ_c is characteristics time scale. If L_r scales as $L_r \sim \rho_i$, then an increase of ion mass implies an unfavorable effect on plasma confinement.

*This chapter is based on the publication: B. Liu *et al* 2015 *Null. Fusion* **55** 112002

Recently, a multi-scale mechanism, based on experimental observations in TEXTOR [56] and TJ-II [100], has been proposed to explain the isotope effect. The basic idea is that the smallest scales (related to Larmor radius) in a plasma can affect the formation of turbulence structures and the development of large-scale zonal flows thus affecting plasma transport. Interestingly, the isotope effect was reported to be weaker in stellarators than in tokamaks [46].

In this paper we present a study of the impact of isotope mass on the development of long-range correlation (LRC) and radial correlation length (L_r) of plasma turbulence in the TJ-II stellarator.

3.2 Experimental set-up

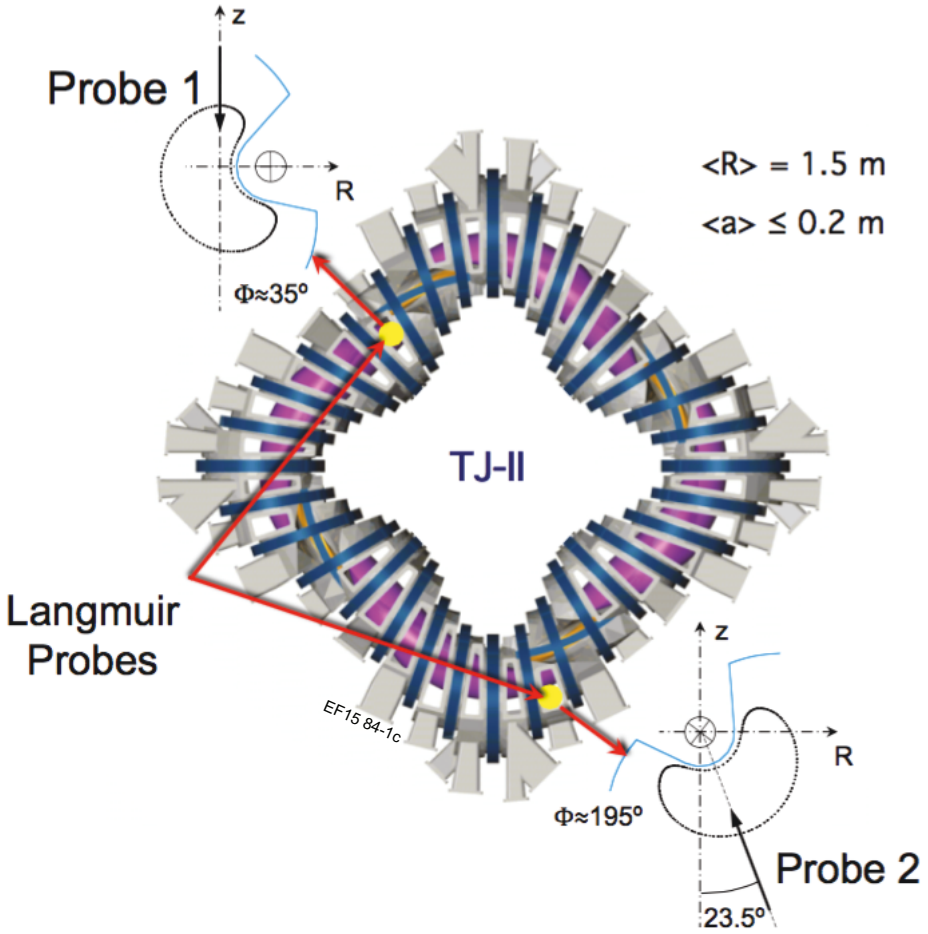

Figure 3.1. A schematic view of TJ-II with two Langmuir probe arrays (Probe1 and Probe 2) installed around toroidally apart (5 m).

Experiments were carried out in the TJ-II stellarator, in Electron Cyclotron Resonance Heated (ECRH) plasmas ($P_{ECRH} \leq 400$ kW, toroidal magnetic field $B_T = 1T$, plasma major radius $\langle R \rangle = 1.5$ m, plasma minor radius $\langle a \rangle \leq 0.22$ m, rotational transform $\iota(a)/2\pi \approx 1.6 - 1.9$). Experiments reported in this paper were performed in low-density deuterium-hydrogen plasmas with plasma density in range $(0.35 - 1) \times 10^{19}$ m^{-3}. Two Langmuir probe arrays, indicated in figure 3.1 as Probe 1 and Probe 2, were installed at different toroidal locations in TJ-II approximately 160° apart (5 m). Probe 1 consists of 4×5 tips with 4 tips in the poloidal direction spaced 3 mm apart and 5 tips in the radial direction spaced 5 mm apart. Probe 2 has a similar configuration with 3×6 tips spaced 2 mm and 3 mm in poloidal and radial directions respectively. For present study, two radial columns of tips, one from each probe (5 tips from Probe 1 and 6 tips from Probe 2), were used to measure floating potential signals at two toroidal locations. This setting allows us to characterize the properties of local turbulence structures and large-scale coherent structures simultaneously.

To study the dependence of plasma properties on isotope mass systematically, the D/H ratio of plasmas was changed steadily shot-to-shot from hydrogen dominated to deuterium dominated plasmas up to the ratio of $D/H \sim 2$ and back to the hydrogen dominated in the same way. Plasma conditions were kept almost identical for all shots.

3.3 Long-range correlation measurements

Long-range correlation (LRC) quantifies the degree of long-range similarity between plasma fluctuations. It is computed as the normalized cross-correlation between two signals x(t) and y(t) as follows:

$$\gamma_{xy}(\tau) = \frac{E\{[x(t+\tau) - \bar{x}][y(t) - \bar{y}]\}}{\sqrt{E\{[x(t) - \bar{x}]^2\}.E\{[y(t) - \bar{y}]^2\}}} \tag{3.1}$$

The maximum LRC between these two signals can be estimated at zero time delay, i.e. $\gamma_{xy}(\tau = 0)$. Using two toroidally separated probe arrays, with each one having multiple tips in the radial direction, we can obtain a matrix of LRC coefficients between each tip in probe 1 measurements with all tips in probe 2 measurements. Then, we use the largest element in this matrix to define the amplitude of LRC, denoted as $\gamma_{12}(\tau = 0)$.

Figure 3.2 plots the time-averaged cross-power spectrum and cross-phase spectrum between two toroidally separated floating potential signals measured by Probe 1 and Probe 2. The correlation between these two signals is dominated by low frequencies (below 20 kHz), and their phase difference is close to zero for the whole frequency range in agreement with previous findings [51].

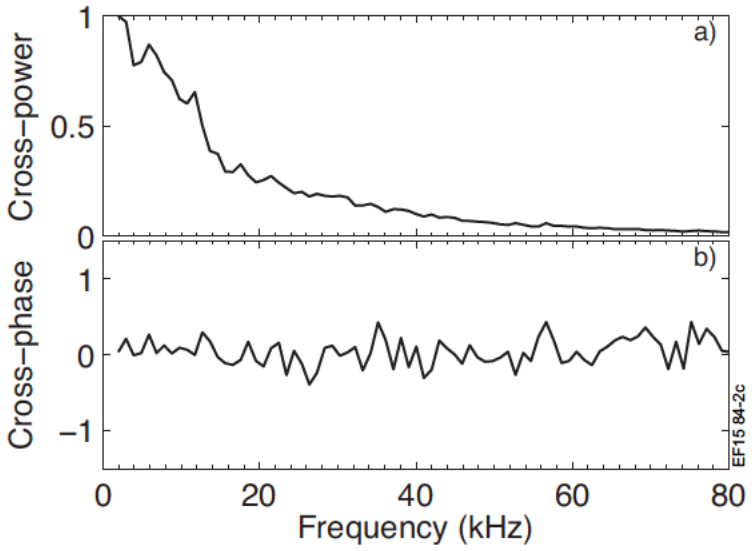

Figure 3.2. The (Top) cross-power spectrum and (Bottom) cross-phase spectrum between two toroidally separated floating potential signals measured in hydrogen plasmas (#34266).

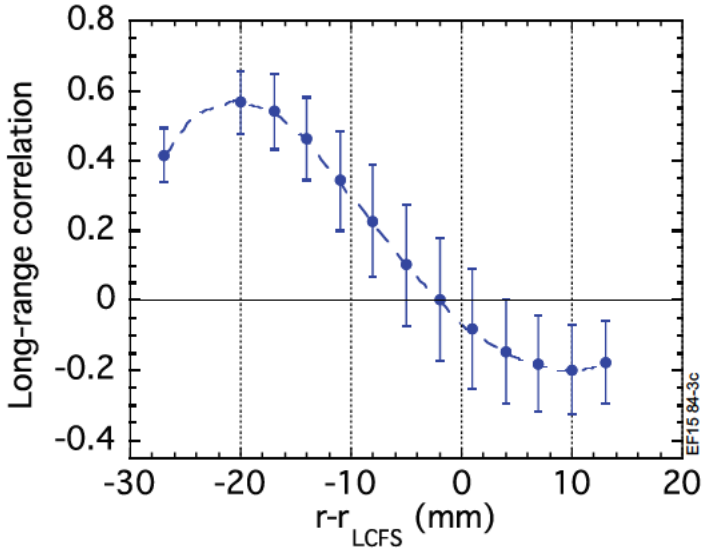

Figure 3.3. A typical profile of long-range correlation (LRC) at the edge of TJ-II.

Figure 3.3 shows a typical profile of LRC, which was obtained through shot-to-shot measurements. We can see that the LRC profile has a characteristic radial scale of the order of a few centimeters. To measure the amplitude of LRC in H and D plasmas, the two toroidally separated probe arrays were both fixed at the radial position of , which is around the position of the peak in the profile of LRC in figure 3.3.

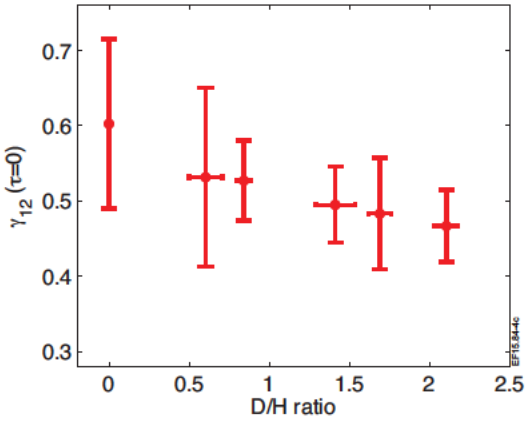

Figure 3.4. The change of the amplitude of LRC with D/H ratio for plasmas at the line-averaged density near to the electron-ion root transition ($n_e \approx 0.6 \times 10^{19} m^{-3}$).

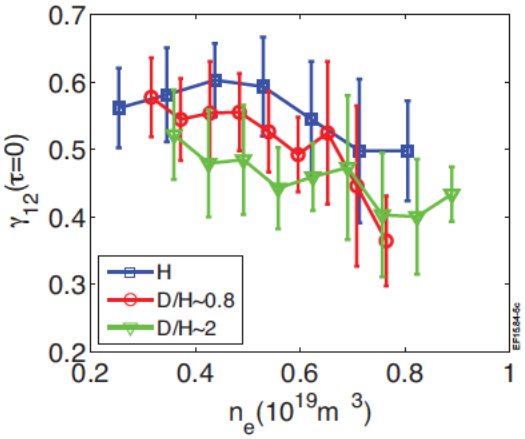

Figure 3.5. The variation of the amplitude of LRC versus line-averaged density for plasmas of different D/H ratios.

Figure 3.4 plots the change of the amplitude of LRC with the D/H ratio at line-averaged electron density in the proximity of the electron-ion root transition ($n_e \approx 0.6 \times 10^{19}$ m^{-3}). It is clear that the amplitude of LRC does not increase with increasing D/H ratio (or effective ion mass), or even shows a slight tendency to decrease. This is in contrast to recent finding in the TEXTOR tokamak, which has observed a systematically increase in the amplitude of LRC with ion mass [56].

Figure 3.5 compares the variation of the amplitude of LRC versus density for plasmas with different D/H ratios: pure H, $D/H \sim 0.8$ and $D/H \sim 2$. It shows that the amplitude of LRC decreases more clearly with ion mass at plasma densities below the electron-ion root transition ($n_e < 0.6 \times 10^{19}$ m^{-3}). Furthermore, a slight decrease in LRC amplitude is observed at plasma densities above the threshold density ($n_e > 0.6 \times 10^{19}$ m^{-3}) in agreement with previous observations [51].

3.4 Radial correlation length measurements

The radial correlation length (L_r) of floating potential fluctuations was characterized using five radially spaced (5 mm apart) tips from Probe 1. Figure 3.6 illustrates an example of

computing . The top panel of figure 3.6 shows a group of functions of the correlation between floating potential signals measured simultaneously by a reference tip (the middle one, tip 3) and all the radially separated probe tips (tip 1-5). The bottom panel of figure 3.6 represents the correlation coefficients after linear interpolation of the correlation functions along the radial direction. We computed L_r, based on the second moment of the correlation coefficient distribution in the radial position and time delay plane, as follows:

$$L_r = 2\sqrt{\frac{2\sum(r_i - \bar{r})^2\gamma(r_i,\tau_j)}{\sum\gamma(r_i,\tau_j)}} \tag{3.2}$$

where r_0 is the radial position of the reference tip, and $\gamma_{i0}(\tau_j)$ is the cross-correlation coefficient between signals at radial position r_i and r_0 at the time delay τ_j. Assuming a Gaussian distribution of correlation coefficients, L_r equals to the full width of $1/e$ radial decay of the the correlation function.

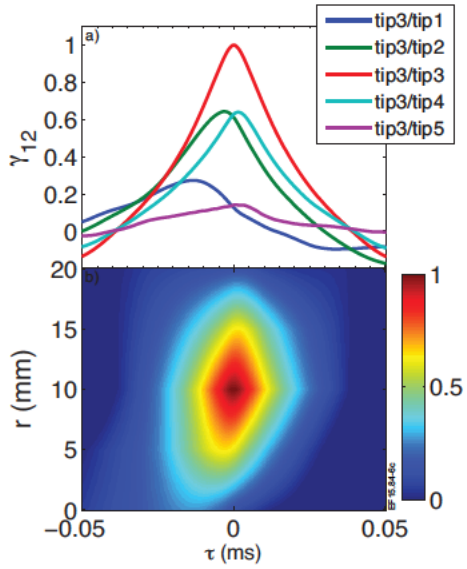

Figure 3.6. An example of computing : (Top) the correlation functions between signals from the reference tip (tip3, the middle one) and all radial tips (tip 1-5, radially spaced 5 mm apart) of Probe 1; (Bottom) the correlation functions after linear interpolation along the radial direction.

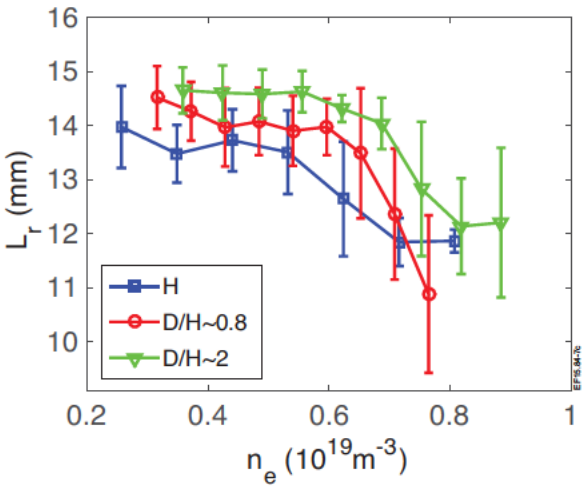

Figure 3.7. The variation of radial correlation length (L_r) versus line-averaged density for plasmas of different D/H ratios.

The same set of shots as for the analysis of LRC were used for the study of L_r. Figure 3.7 compares the variation of L_r with line-averaged electron density for different D/H ratios.

We can observe that L_r slightly increases with increasing effective D/H ratio over almost the whole density range. This is consistent with results from TEXTOR [56], TJ-K [58] and FT-2 [101]. By comparing H and D/H ~ 2 plasmas, we found that 70% increase in the effective ion mass corresponds to 10% increase in radial correlation length. In the electron-root regime ($n_e < 0.6 \times 10^{19}$ m^{-3}), we estimated that L_r scales with effective ion mass as $L_r \sim m^{0.2\pm0.1}$. It can also be seen that L_r decreases when the plasma transits to the ion-root ($n_e > 0.6 \times 10^{19}$ m^{-3}) where edge sheared flows are developed [102].

A preliminary analysis of the isotope dependence of particle confinement was conducted in the TJ-II stellarator based on $H_\alpha(D_\alpha)$ measurements. It was observed that the particle confinement tends to decrease with increasing D/H ratio. It is interesting to note that the impurity confinement was also found to decrease with D/H ratio in TJ-II [103]. A quantitative study of the scaling of plasma confinement with isotope mass will be reported in a forthcoming publication.

3.5 Conclusion

We have investigated the impact of the isotope mass on the development of long-range correlation (LRC) and radial correlation length (L_r) of plasma turbulence in ECRH plasmas in the TJ-II stellarator with the following conclusions: a) the amplitude of the LRC slightly decreases with isotope mass in contrast to TEXTOR [56] results; b) the local correlation length L_r increases with isotope mass in agreement with TEXTOR [56], TJ-K [58] and FT-2 [101] results. Those findings show the impact of the isotope effect on both the largest scales (LRC determined by the size of the device) and the characteristic radial scales of turbulent structures.

Chapter 4

Multi-scale study of the isotope effect in ISTTOK *

The isotope effect, namely the isotope dependence of plasma confinement, is still one of the principal scientific conundrums facing the magnetic fusion community. We have investigated the impact of isotope mass on multi-scale mechanisms, including the characterisation of radial correlation lengths ($\boldsymbol{L}_r$) and long-range correlations (LRC) of plasma fluctuations using multi-array Langmuir probe system, in hydrogen (H) and deuterium (D) plasmas in the ISTTOK tokamak. We found that when changing plasma composition from the H dominated to D dominated, the LRC amplitude increased markedly (10–30%) and the $\boldsymbol{L}_r$ increased slightly ($\sim$ 10%). The particle confinement also improved by about 50%. The changes of LRC and $\boldsymbol{L}_r$ are congruent with previous findings in the TEXTOR tokamak (Xu et al 2013 Phys. Rev. Lett. 110 265005). In addition, using biorthogonal decomposition, both geodesic acoustic modes and very low frequency (< 5 kHz) coherent modes were found to be contributing to LRC.

4.1 Introduction

Understanding the mechanism of plasma confinement scaling with isotope mass has been a long-standing open issue in magnetic confinement fusion plasma research. It has been observed in most tokamak experiments that the plasma confinement time increases with increasing ion mass under similar plasma conditions [44]. However, standard transport theories fail when predicting the isotope effect. According to diffusive-like transport theories, the diffusivity is $D \propto L_{\mathrm{r}}^2/\tau_{\mathrm{c}}$, where L_{r} is characteristic radial scale length, and τ_{c} is the

*This chapter is based on the publication: B. Liu *et al* 2016 *Null. Fusion* **56** 056012

characteristic time scale. If L_r scales as $L_r \sim \rho_i$, then an increase of ion mass implies an unfavourable effect on plasma confinement.

If turbulent fluctuations are characterised by the macroscopic size of the plasmas, the transport has the conventional Bohm scaling, whereas if they are determined by the gyro-radius, it is described by the gyro-Bohm scaling. The observation in L-mode regimes of gyro-Bohm-like transport scaling for the electron channel indicates that the characteristic radial wavelength of the plasma turbulence is on the order of the Larmor radius, rather than the plasma radius, while Bohm-like transport for ions has been observed [104]. In addition, the effective diffusivity and global confinement time scaling were found to vary from gyro-Bohm-like to Bohm-like depending upon whether the electron or ion channel dominated the heat flux [105]. Some simulations have shown a gradual transition from a Bohm-like scaling for small system size to a gyro-Bohm scaling for larger plasma systems [106]. However, while Bohm and gyro-Bohm behaviour are widely used to describe the empirical confinement time, they have the wrong isotopic mass dependence [107]. Moreover, experimental studies have shown a reduction of the L–H power threshold by about 50% when using deuterium (D) and helium (He) instead of hydrogen (H). Present ITPA scaling laws predict that ITER H-mode operation is likely in He but only marginally feasible in H [108]. Thus, a better understanding of the isotope dependence of the L–H power threshold is urgently needed to improve our confidence in ITER scenarios.

Recently, a multi-scale mechanism has been proposed to explain the isotope effect [56]. The development of zonal flows/geodesic acoustic modes (GAMs) by inverse energy cascade via $E \times B$ symmetry breaking mechanisms (i.e. eddy tilting) should be strongly sensitive to the size of turbulence structures. Considering that the typical radial scale length of mean $E \times B$ sheared flows, $\lambda_{E\times B}$, is in the order of 1 cm, the amplitude of inverse energy cascading processes is expected to be k-dependent with maximum energy transfer in k-scales in the order of $2\pi/\lambda_{E\times B}$ (i.e. wave number in the range of 5–10 cm^{-1}). Thereupon, a minor increase in the size of turbulent structures, λ_{turb} in the range of $\lambda_{turb} \approx \lambda_{E\times B}$, may eventually result in an increase in the amplitude of zonal flows/GAMs. Changes of zonal flows and GAMs with isotope mass have been found through experiments [56, 49, 109] and simulations [110, 111, 59].

In this paper, we present a study of the isotope effect from the prospective of multi-scale mechanism in the ISTTOK tokamak.

4.2 Experimental methods

The ISTTOK tokamak is a large aspect-ratio circular cross-section tokamak ($R = 46\,\mathrm{cm}$, $a = 8.5\,\mathrm{cm}$, $B_\mathrm{T} = 0.5\,\mathrm{T}$, $I_\mathrm{P} \approx 4$–$6\,\mathrm{kA}$) with a poloidal graphite limiter. Around the limiter radius the electron temperature is about $T_\mathrm{e} \approx 20\,\mathrm{eV}$ and the electron density is $n_\mathrm{e} = 0.5$–$1 \times 10^{18}\,\mathrm{m}^{-3}$.

Two Langmuir probe arrays, indicated in figure 4.1 as the 2D probe and rake probe, were installed in ISTTOK approximately 120° toroidally and 60° poloidally apart from each other, and with a distance of about 1 m. A field line passing through one of the tips of the first probe is expected to run several toroidal turns before hitting one of the tips of the second probe. The rake probe consists of 10 tips (7 tips were connected in the present study) spaced 3 mm apart in the radial direction. The 2D probe consists of 4×4 tips spaced 3 mm apart in both radial and poloidal directions. For our present study, the first radial column of tips was considered.

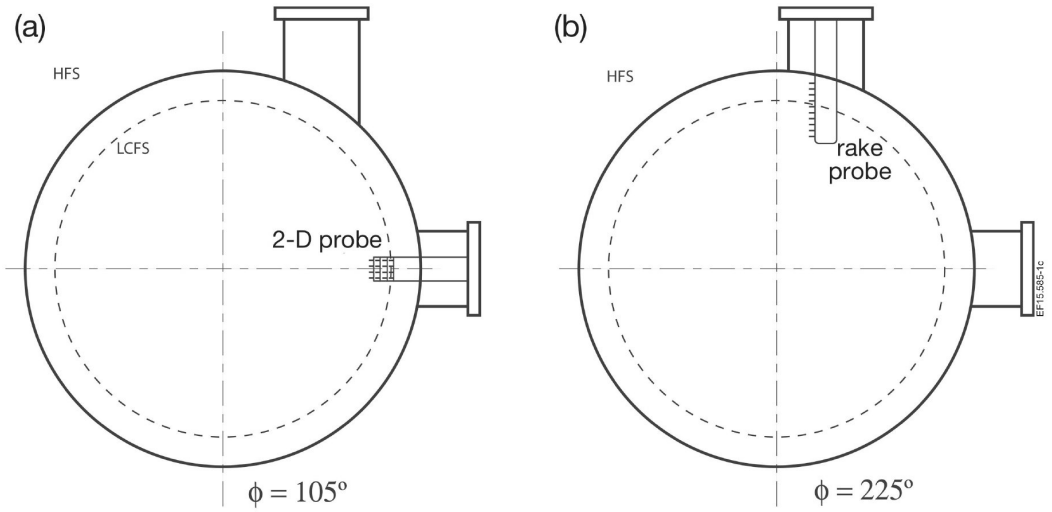

Figure 4.1. Schematic of two toroidal cross-sections of ISTTOK showing the toroidal and poloidal locations of the 2D probe (a) and rake probe (b). Both probes can move radially from shot to shot.

Both probes were operated in floating potential measurement mode. This setting allows for simultaneous characterisation of local turbulence structures and large-scale coherent structures in the edge plasma: the local turbulence structures can be estimated from the correlation length in floating potential fluctuations measured with the rake probe; the large coherent structures can be detected and quantified from the correlation between floating potential fluctuations measured with the rake probe and the 2D probe. The sampling rate of the probe data acquisition is 2 MHz. To quantify particle confinement in H and D plasmas, the Balmer-alpha monitor was tuned into 656 nm and equipped with a filter of bandwidth of

3 nm to collect both H_α and D_α emission. In a H/D plasma, two peaks corresponding to H_α and D_α emission were fitted with Gaussian curves. D/H ratio was then estimated from the ratio of the intensities of these two Gaussian curves.

There were two experimental campaigns (in the years 2013 and 2014) dedicated to isotope effect study in ISTTOK. In both campaigns, experiments started with H plasmas and followed by D/H mixed plasmas with D/ (D + H) > 85% in the 2013 and D/ (D + H) > 90% in the 2014. Hereafter, the D/H mixed plasmas will be referred to as D plasma for convenience. Owing to the reproducibility of discharges in ISTTOK, plasma conditions (plasma current, vertical position and radial position) were kept almost identical in each campaign. To compare the properties of H and D plasmas, we considered plasmas with stable plasma current and density from the first positive half-cycle of the discharges: time windows, $16 < t < 29$ ms for 2013 data and $10 < t < 24$ ms for 2014 data.

4.3 Results

4.3.1 Particle confinement

Changes in global particle confinement time were estimated from the ratio of the total number of electrons in the discharge (assumed to be proportional to the line-averaged density n_e) to the total ionization rate at the plasma periphery (assumed to be proportional to the H_α $\left(D_\alpha\right)$ emission). The most significant source of recycling in ISTTOK is in the limiter region, as it has a poloidal limiter. The H_α $\left(D_\alpha\right)$ emission was therefore measured by a photodiode looking tangentially to the plasma into the limiter. The line-averaged electron density was measured along a line of sight crossing vertically the plasma at the centre of the poloidal cross-section. It was found that the particle confinement of D plasmas was 50% higher than that of H plasmas in ISTTOK (figure 4.2). This result is in line with the isotope dependence of plasma confinement for most tokamaks [44].

4.3.2 Amplitude of long-range correlation

Long-range correlation (LRC) measures the long-distance similarity of plasma fluctuations. It is a standard tool used to detect large coherent structures (e.g. zonal flows, GAMs) in plasma turbulence [56, 49, 91, 51, 112]. To quantify LRC, we compute the normalised cross-correlation between two toroidally separated signals x(t) and y(t) as follows:

$$\gamma_{xy}(\tau) = \frac{E\{[x(t+\tau) - \bar{x}][y(t) - \bar{y}]\}}{\sqrt{E\{[x(t) - \bar{x}]^2\}.E\{[y(t) - \bar{y}]^2\}}}$$

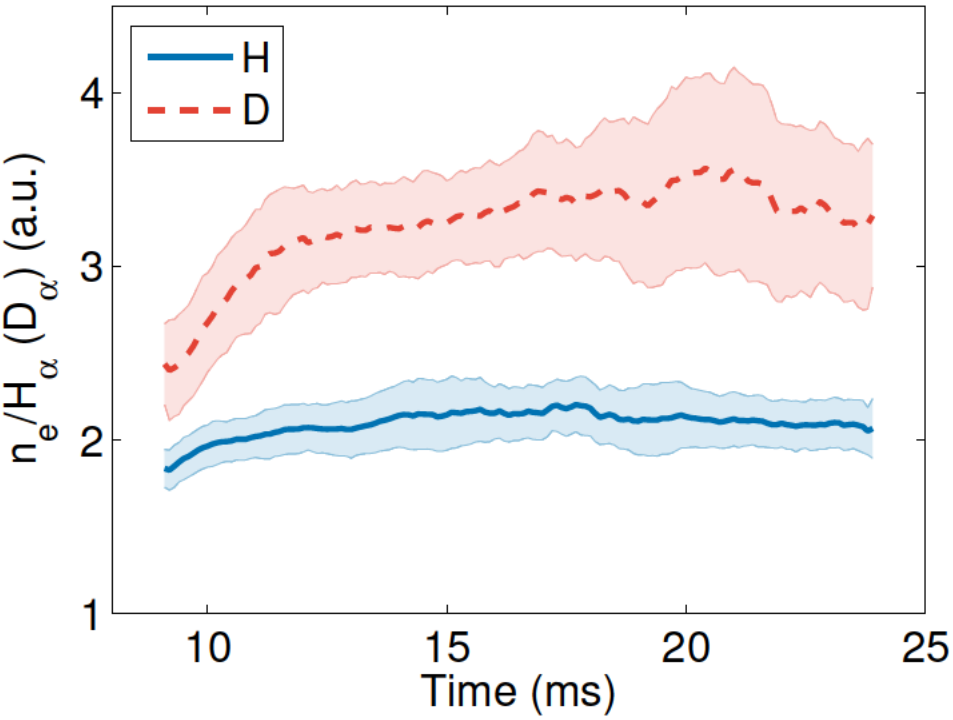

Figure 4.2. Time evolution of particle confinement for H and D plasmas. The shaded regions indicate standard deviation of mean among 10 H plasma shots (37261, 37262, 37263, 37264, 37266, 37268, 37269, 37270, 37271, 37272) and eight D plasma shots (37350, 37357, 37359, 37361, 37364, 37365, 37366, 37368).

The maximum LRC between these two signals is estimated at zero time delay, i.e. $\gamma_{xy}(\tau = 0)$. From our multi-array Langmuir probe system (6 radial tips from the rake probe and 4 radial tips from the 2D probe), we can get a 4×6 matrix of LRC. The largest element in this matrix quantifies the amplitude of LRC between these two distant probe arrays. Figure 4.3(a) shows an example of visualising the amplitude LRC. As indicated by the dash lines, the amplitude LRC takes place between two tips at different radial positions. This is probably due to a shift in the plasma geometric centre with respect to that of the vacuum vessel (plasma displaced in the radial or vertical direction). When we take the radial positions of the amplitude of LRC as reference points, we found that the floating potential profiles measured simultaneously by the two probe arrays are similar (figure 4.3(b)). This offers us a way to label the magnetic flux surface [68].

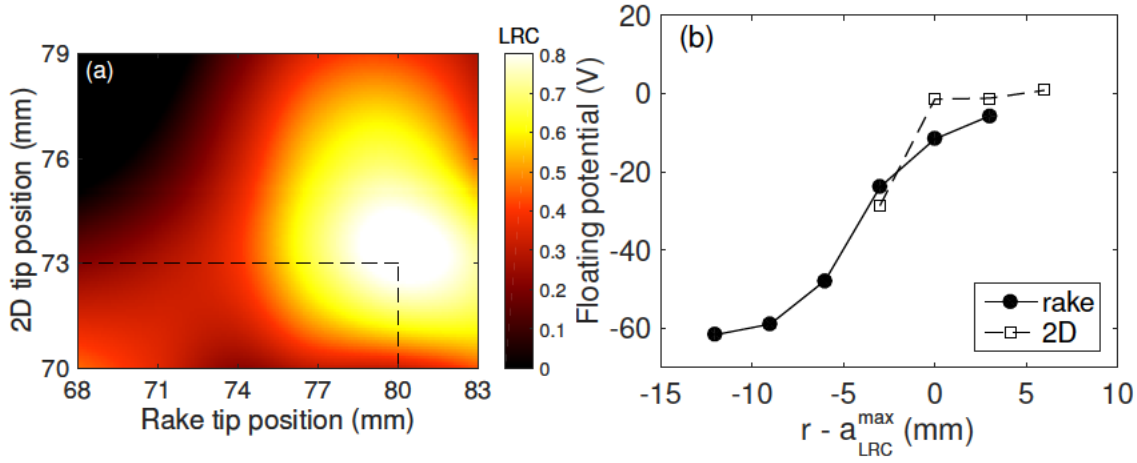

Figure 4.3. Example of visualising the amplitude of LRC (#35580, 19 < t < 20.5 ms). (a) Contour plot of LRC, linearly interpolated. (b) Profiles of floating potentials measured by probe rake probe and 2D probe with reference points at the positions of the amplitude of LRC (for the rake, $a^{\max}_{\mathrm{LRC}} = 80$ mm; for the 2D, $a^{\max}_{\mathrm{LRC}} = 73$ mm).

4.3.3 Cross-power spectra

To resolve the frequency of the large coherent structures contributing to LRC, we computed the cross-spectrum between two toroidally separated probe tips, between which maximum LRC takes place (figure 4.4). Peaks of frequency of around 12 kHz for D plasma and 14 kHz for H plasma with width less than 10 kHz were identified. This agrees with a previous study on GAMs in ISTTOK [112]. The decrease of GAM frequency with isotope mass is consistent with the predicted by the relation $f_{\mathrm{GAM}} \propto 1/\sqrt{M_i}$ [35] and in agreement with previous experimental results from the FT-2 tokamak [109]. Interestingly, in addition to a significant cross-power at the GAM frequencies, there is also large cross-power towards very low frequencies below 10 kHz.

4.3.4 Biorthogonal decomposition analysis of coherent modes

In this section, we use biorthogonal decomposition (BOD) method to study the low frequency coherent modes in ISTTOK. BOD has been previously used for the identification of zonal flow-like structure [113].

With multipoint measurements (e.g. probe array), we obtain a data matrix $Y(i,j)$, where the index $i = 1,\ldots,N$ labels the time and $j = 1,\ldots,M$ the detector (probe tip). BOD decomposes the data matrix $Y(i,j)$ as follows:

$$Y(i,j) = \sum_k \lambda_k \Psi_k(i) \Phi_k(j)$$

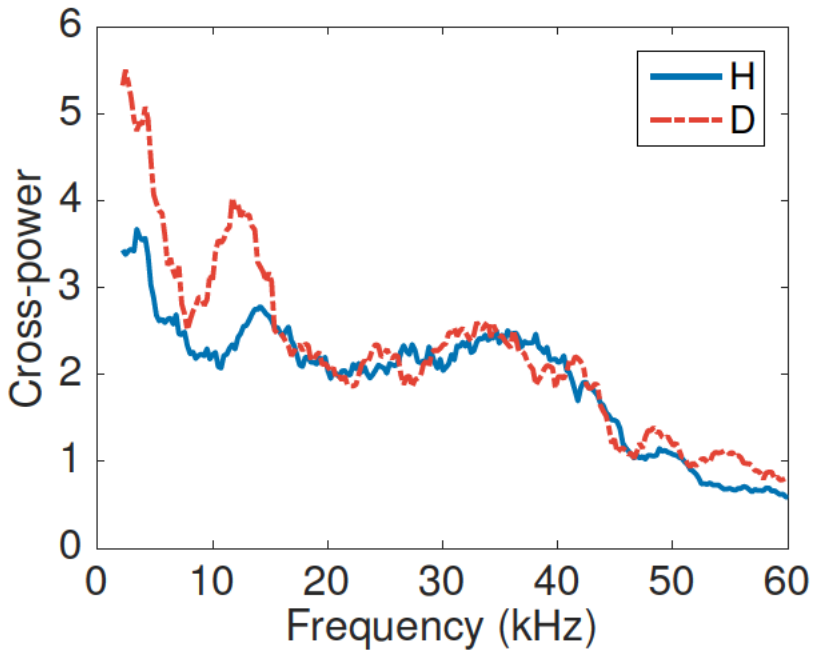

Figure 4.4. Cross-spectra of H and D plasmas. Spectra were averaged over six shots of H plasma and five shots of D plasma. Frequencies below 2 kHz were removed (2013 data).

where ψ_k is called a 'chrono' (a temporal function) and ϕ_k a 'topo' (a spatial function). Chronos and topos satisfy the orthogonality relations: $\sum_i \psi_k(i)\psi_l(i) = \sum_j \phi_k(j)\phi_l(j) = \delta_{kl}$. ψ_k and ϕ_k are ordered by the eigenvalue of λ_k, which represents the contribution of mode k to the total fluctuation energy. Further analysis of the chronos and topos gives us information about spectral, correlation and spatial structure properties of each mode.

For application to ISTTOK, the data matrix was obtained from two subsets of floating potential measurements: seven tips of rake probe and four tips (one column) of the 2D probe. Figure 4.5 shows the results of BOD analysis. Figure 4.5(a) shows that the fluctuation energy is dominated by first two modes. The first mode is dominated by very low frequencies (< 5 kHz). It is radially localised and contributes to LRC. The second mode is dominated by frequency ($10 - 25$ kHz), which is at the regime of GAMs [112], and contributes the most to LRC. To clarify the properties of these two modes, we computed the coherence between magnetic fluctuation signals measured with Mirnov coils located at the low field side and Langmuir (floating potential) probe signals, as shown in figure 4.6. A relatively high coherence was found at frequencies of just a few kHz (~ 2 kHz), corresponding to the first mode in 4.5(c). This indicates that the radially localised low frequency (~ 2 kHz) mode is coupled with an MHD oscillation at the edge. The decrease of coherence at frequencies $10 - 25$ kHz is in agreement with previous studies of GAMs in ISTTOK [112]. At the lowest frequencies, the coherence between Mirnov and floating potential signals decreases to noise levels mean-

ing that there is also a contribution to LRC from electrostatic modes. This suggests that there may also be zonal flows at very low frequencies. Although low-frequency zonal flows are regularly observed in the TJ-II stellarator [51, 91], they are seldom observed to coexist with GAMs in tokamaks; one such observation has been reported in the HL-2A tokamak [114]. The properties and generation mechanism of low-frequency coherence mode contributing to LRC in ISTTOK is under further investigation.

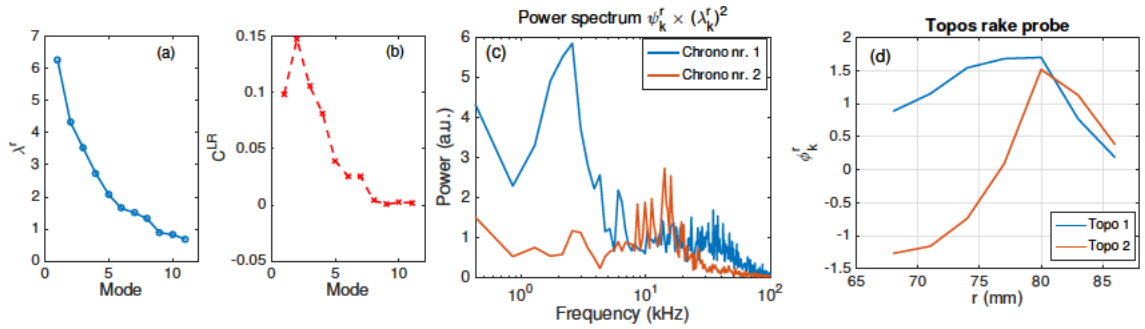

Figure 4.5. (a) BOD eigenvalues, (b) long-range correlation contribution of each mode, (c) spectra of the chronos of first two BOD modes, and (d) topos of the first two BOD modes. (#37261).

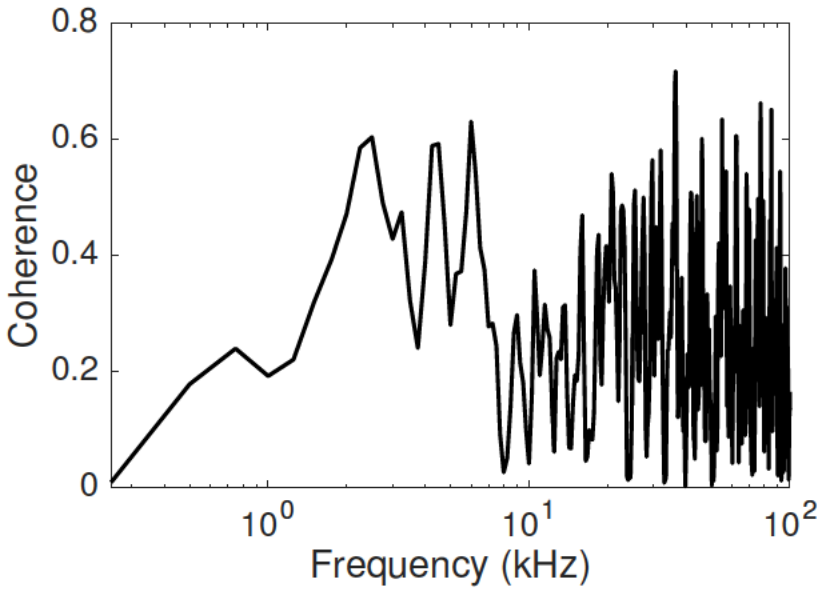

Figure 4.6. Coherence between floating potential signal and magnetic fluctuation signal measured by Mirnov coil (#37261).

4.3.5 LRC of H and D plasmas

We compared time evolution of the amplitudes of LRC in H plasmas and D plasmas with data from both campaigns (the years 2013 and 2014). In each campaign, multiple shots of H plasma and D plasma of the same plasma conditions and probe positions were considered. As can be seen in figure 4.7, the amplitudes of LRC in D plasmas were 10–30% higher than those in the H plasmas. These results agree with the previous finding in TEXTOR [56]. The time evolution of the amplitudes of LRC started at the similar level in both campaigns, but in 2014 they decreased steadily along the discharges. This is most likely due to slow outward movements of the plasmas. Figure 4.8 plots the amplitude of LRC versus floating potentials measured by rake probe with the data from 2014. This is to confirm the change of LRC amplitude with isotope mass under the same floating potentials. We can also see that significant LRC took place at the floating potential $-10 < \phi_f < 10$ (V).

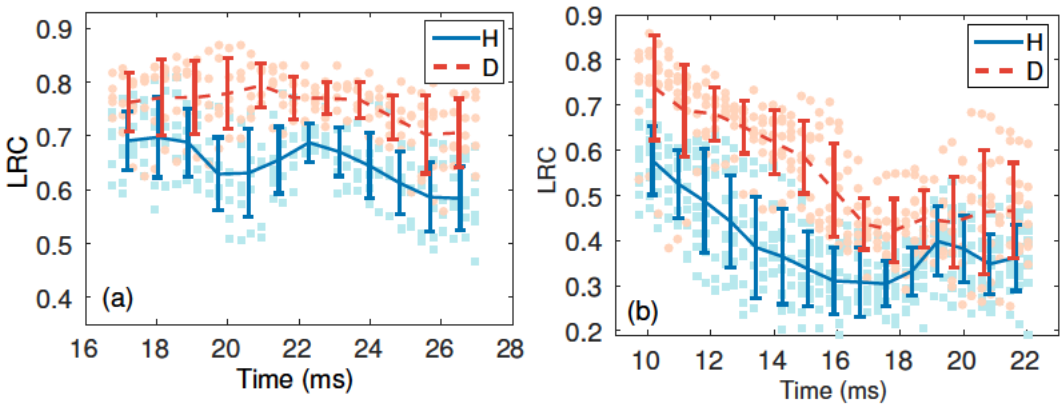

Figure 4.7. Time evolution of the amplitude of LRC for the campaign 2013 (a) and 2014 (b). The error bars indicate standard deviation of mean LRC among six H plasma shots and five D plasma shots for 2013, and 10 H plasma shots and seven D plasma shots for 2014.

4.3.6 Radial correlation length

The radial correlation length (L_r) of floating potential fluctuations was characterized using the rake probe. L_r was defined as the second moment of the distribution of the cross-correlation coefficients between the fluctuation of signals measured with all tips and a reference tip (the middle tip for present study) of the rake probe. Assuming a Gaussian distribution of correlation coefficients, L_r is equal to the full width at $1/e$ of the maximum correlation

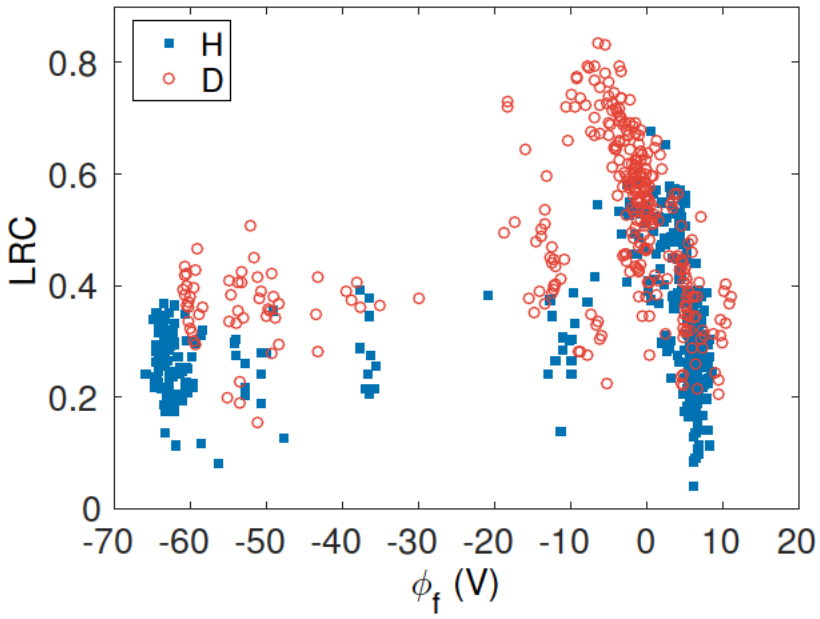

Figure 4.8. Comparison of the amplitude of LRC versus floating potentials measured with rake probe for H and D plasmas (2014 data).

coefficient. L_r is computed as follows:

$$L_r = 2\sqrt{\frac{2\sum(r_i - \bar{r})^2\gamma(r_i,\tau_j)}{\sum\gamma(r_i,\tau_j)}}$$

where r_0 is the radial position of the reference tip, and $\gamma_{i0}\left(\tau_j\right)$ is the cross-correlation coefficient between signals at radial position r_i and r_0 at the time lag τ_j. The maximum time lag was taken as 30 μs for present study. In general, this method may include correlation due to radial propagation if there are turbulent structures propagating radially. In the present study, this radial propagation was not found to alter the L_r significantly.

For estimating L_r, we used 14 H plasma shots and 12 D plasma shots with the same plasma conditions and the same radial position, $r = 68\ mm$ ($\rho = 0.8$), of the rake probe. In this case, the rake probe tips cover the radial region $\rho = 0.8 \sim 0.97$ (from the innermost to the outermost tips).

We computed the radial correlation length (L_r) at two frequency bands: low frequency band, 1 < f < 25 kHz, including low frequency coherent events (e.g. GAM, zonal flow and MHD), and a high frequency band, 25 < f < 250 kHz, dominated by a broadband ambient turbulence.

Figure 9 shows the time evolution of L_r in H and D dominated plasmas. The low frequency range (1 < f < 25 kHz) L_r was found slightly higher ($\sim$ 10%) in D plasmas than in

H plasmas. At the high frequency range (25 < f < 250 kHz) L_r is comparable in D and H plasmas and lower than the L_r value measured at the low frequency range. Because of the dominance of low frequency cross-power, the L_r at the whole frequency mainly reflects the low frequency fluctuations. The increase of L_r with isotope mass has also been observed in TJ-K [58], FT-2 [101], TJ-II [49] and AUG [115].

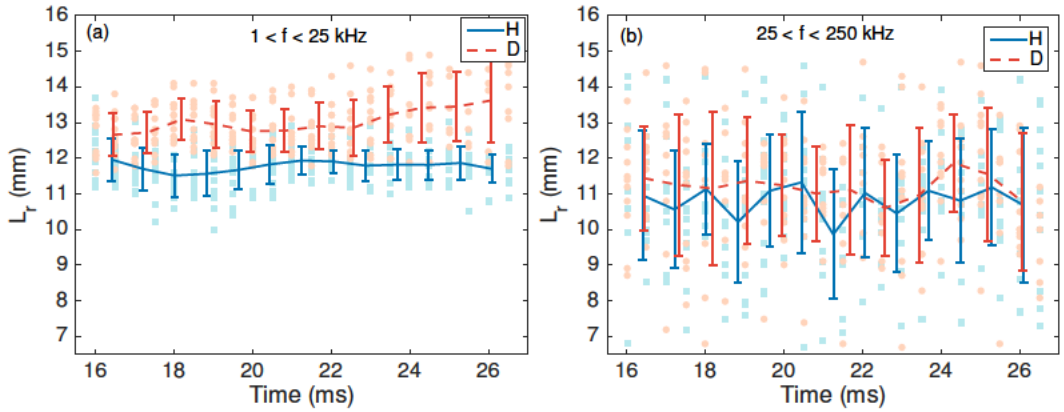

Figure 4.9. Time evolution of radial correlation length (L_r) in H and D plasmas at: (a) low frequency band 1 < f < 25 kHz; (b) high frequency band 25 < f < 250 kHz. Error bars indicate standard deviation of the mean L_r among 14 H plasma shots and 12 D plasma shots (2013 data).

These results suggest that, distinguishing the radial scale of large scale coherent structures (which, in the case of zonal flow-like structures, do not contribute to transport), and the scale of local turbulence, may be necessary to elucidate upon the dependence of the characteristic size of fluctuating structures with plasma gyro-radius and the isotope physics.

4.4 Conclusion

We have investigated the impact of isotope mass on particle confinement and the development of LRC and radial correlation length (L_r) of plasma fluctuations in the ISTTOK tokamak. We have found that: (a) particle confinement increases significantly with isotope mass; (b) both LRC and L_r increase with isotope mass; and (c) through BOD analysis, both GAMs and very low frequency (<5 kHz) coherent modes were found contributing to LRC. These findings show the impact of the isotope effect on both the largest scales (LRC, determined by the size of the device) and the characteristic radial scale (L_r) of plasma fluctuations.

Chapter 5

Electromagnetic turbulence measurements during the L-H transition in the TJ-II stellarator *

5.1 Introduction

It is well known that sheared flows can suppress turbulence and help to improve plasma confinement. Fluctuating, turbulence-generated zonal flows are a benign non-linear turbulence saturation mechanism, consistently observed in simulations and reported in several experiments. Because of their transport modulation capability zonal flows have been considered natural candidates for triggering the L-H transition. Theoretically, both electrostatic fluctuation-induced Reynolds stress and magnetic fluctuation-induced Maxwell stress can play a role in affecting zonal flows generation [37]. Whereas measurements of Reynolds stress with multi-pin Langmuir probes have been conducted in several devices [31], only a few measurements of Maxwell stress have been reported [116]. In this work we present local measurements of magnetic properties and Maxwell stresses in the proximity of the L-H transition in the TJ-II stellarator.

5.2 Experimental methods

Experiments were carried out in the TJ-II stellarator, in the pure NBI heated plasmas (toroidal magnetic field $B_T = 1$ T, plasma major radius $\langle R \rangle = 1.5$ m, plasma minor radius $\langle a \rangle \leq 0.22$m, rotation transform $\iota(a)/2\pi \approx 1.6 - 1.9$). The electromagnetic properties were measured us-

*This chapter is based on the publication: B. Liu *et al* 2015 *EPS* P4.166

ing an electromagnetic (EM) probe (also dubbed 'vorticity probe') [95, 117] consisting of a Langmuir probe array and three three-axial pick-up coils, which measure the time derivative of the three components of magnetic field. The three magnetic probes form a right angle in the radial-poloidal plane. They are separated by 3 cm in both radial and poloidal directions. The Langmuir probe array locates in the middle of two magnetic probes in the radial direction. This setup allows simultaneous measurements of magnetic and electrostatic properties.

The direct measurement by the magnetic coils is time derivative of the magnetic fields, $\frac{\partial B}{\partial t}$, while the quantity of interest for the calculation of Maxwell stress is the fluctuation of magnetic field $\tilde{B}$. To calculate Maxwell stress $\left\langle \tilde{B}_r \tilde{B}_\theta \right\rangle$ from $\frac{\partial B}{\partial t}$, the following two approaches are considered. For convenience, in the following part we denote the magnetic field in time domain by $b(t)$ and its Fourier transform by $B(\omega)$.

Time domain First do the integration (cumulative sum) of time series $\frac{\partial b(t)}{\partial t}$ in time domain. Then removing the mean with a high pass filter (2 kHz), we get the fluctuation $\tilde{b}(t)$. Averaging the product $\tilde{b}_r(t)\tilde{b}_\theta(t)$ over time window of interest gives us the maxwell stress.

Frequency domain To compute the magnetic fluctuation, we can do Fourier transform of the signal $\mathrm{FFT}(\frac{\partial b}{\partial t}) \longrightarrow B_\omega = i\omega B$. Then by inverse Fourier transfer of $B(\omega > 2\,\mathrm{kHz})$, $\mathrm{IFFT}(\frac{B_\omega}{i\omega}|_{\omega>2}) \longrightarrow \tilde{b}(t)$

Parseval's theorem states that $\sum_t b_r(t)b_\theta(t) = \frac{1}{N}\sum_\omega B_r(\omega)B_\theta(\omega)$. This gives us a way to compute Maxwell stress in frequency domain, $\sum_t \tilde{b}_r(t)\tilde{b}_\theta(t) = \frac{1}{N}\sum_{\omega>2\mathrm{kHz}} B_r(\omega)B_\theta(\omega)$.

These approaches allow us to compute the time evolution of Maxwell stress as well as the frequency resolved maxwell stress.

5.3 Radial profiles of magnetic fluctuation and Maxwell stress

Radial profiles of electromagnetic properties were measured by the EM probe on a shot-to-shot basis in TJ-II. Sixteen shots of similar plasma conditions with probe measured at six different radial positions were taken into account for this analysis. Figure 5.1(a) shows the radial profile of magnetic fluctuation (rms). Magnetic fluctuation level increases significantly radially inwards. Maxwell stress was estimated by the time average of the product of radial and poloidal components of magnetic field fluctuation $\left\langle \tilde{B}_r \tilde{B}_\theta \right\rangle$. As shown in figure 5.1(b), the Maxwell stress as well as its gradient also increase radially inwards reaching values close to $10^5\ m^2/s^2$ at the innermost radial position ($\rho = 0.86$), which were the measurements so far available. When comparing with Reynolds stress previously measured in

TJ-II with Langmuir probe, both the level and gradient of Maxwell is relatively low [118]. The frequency resolved Maxwell stress, shown in figure 5.1(c), suggests that the main contribution to Maxwell stress comes from the magnetic fluctuation with frequencies below 50 kHz. This agrees with Maxwell stress measurements from the Extrap-T2R RFP [116].

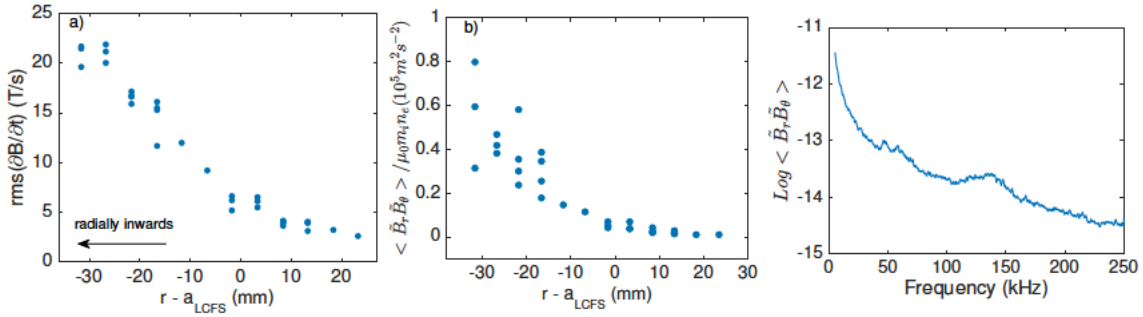

Figure 5.1. (a) Profile of magnetic fluctuation level; (b) P profile of Maxwell stress; and (c) frequency resolved Maxwell stress.

5.4 Electromagnetic dynamics during L-H transition

The time evolution of plasma parameters and edge fluctuations were monitored by the EM probe in the proximity of the L-H transition for the shot #37638 (figure 5.2), showing a decrease in H_α and the level of electrostatic and magnetic fluctuations. We also notice that in the middle of the H-mode there is a burst (at around 1027 ms) which shows up in almost all measured signals, including I_s and parallel current density $\tilde{J}_\parallel$. This indicates that the burst may be related to some filamentary electromagnetic structure. Further investigation of this ELM-like event is in progress. The reduction of electrostatic and magnetic fluctuation in a wide frequency range can be seen in figure 5.3.

To explore the variation of local electrostatic turbulence structure during L-H transition, we measured the radial correlation length (L_r) and poloidal correlation length (L_θ) with two radial and two poloidal Langmuir probe tips using standard two-point correlation technique [85]: the correlation length L_c was estimated from the broadening of fluctuation power spectrum in the wavenumber axis in the wavenumber-frequency plane. Figure 5.4 shows the time evolution of the local turbulence structure. L_r decreases as approaching the L-H transition. When L-H transition taking place, L_θ appears to increase.

Figure 5.5(a) shows the time evolution of Maxwell stress measured by three magnetic probes in the vorticity probe. Maxwell stress measured by probe 1 is significant larger than by probe 2 and 3. With these measurements, the gradients of Maxwell stress in the radial direction can be estimated, as shown in figure 5.5(b). Considering the distance between

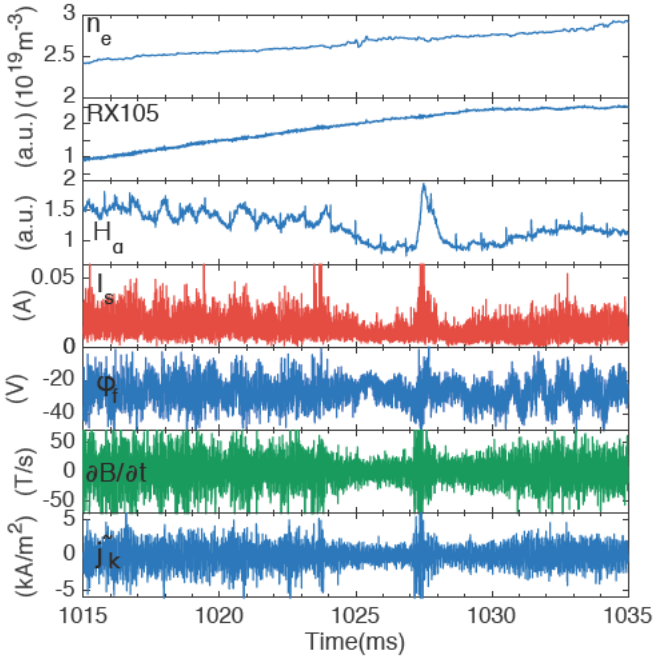

Figure 5.2. Time evolution of plasma parameters (#37638).

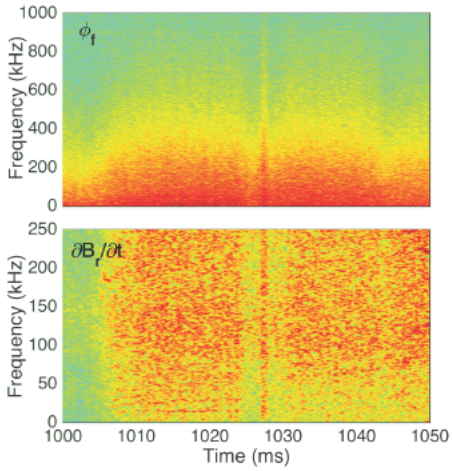

Figure 5.3. Spectrogram of floating potential and magnetic fluctuation. The sampling rate of floating potential measurement is 2 MHz and magnetic fluctuation measurement is 500 kHz. This results in different frequency scales.

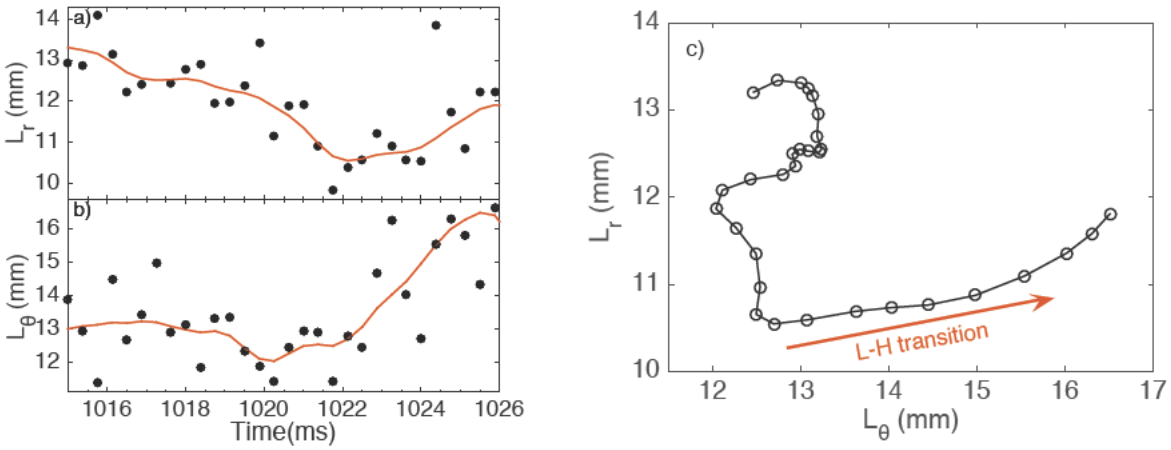

Figure 5.4. Time evolution of (a) radial correlation length (L_r); (b) poloidal correlation length (L_θ); and (c) the portrait L_r and L_θ.

two probe is 3 cm, we estimated that the gradient of Maxwell stress can reach the order of 10^7 m/s^2 at around $\rho = 0.9$. This is about one order of magnitude lower than the gradient of Reynolds stress ($\sim 10^8$ m/s) previously measured in TJ-II [118]. We note that this position has not yet reached the transport barrier region which is at $\rho < 0.85$ in TJ-II [119]. It may be interesting to have measurements of Maxwell stress further inside the plasmas in TJ-II in the future. The cross-power spectrogram between the two components for the analysis of Maxwell stress is shown in figure 5.5(c) showing that the Maxwell stress is mainly due to the fluctuation of magnetic field at low frequencies.

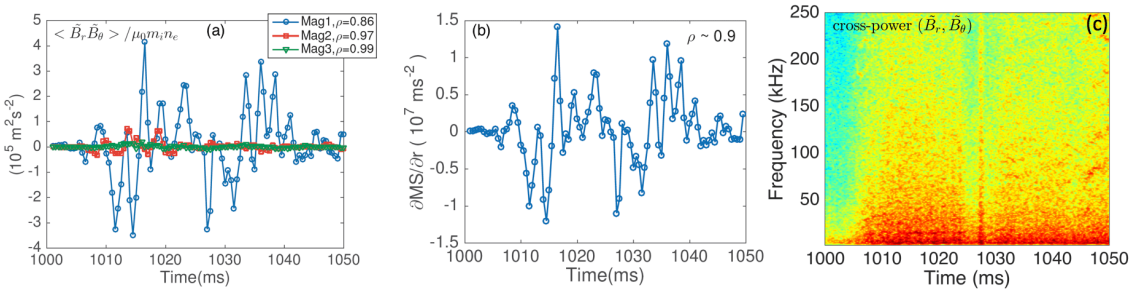

Figure 5.5. Time evolution of (a) Maxwell stresses measured at three different radial position and (b) gradient of Maxwell stress, estimated by two radial magnetic probes; (c) cross-power spectrogram between $\tilde{B}_r$ and $\tilde{B}_\theta$.

5.5 Conclusion

We have conducted electromagnetic measurements of plasma turbulence in the TJ-II stellarator with the electromagnetic probe up to the position of $\rho = 0.86$. It has been found that magnetic fluctuation and Maxwell stress increase radially inwards; in the proximity of L-H transition, a significant gradient of Maxwell stress was observed at the plasma edge. The value is about one order of magnitude lower than previously measured Reynolds stress [118], however, considering the measurement position was still outside the transport barrier [119], it would be interesting to measure the Maxwell stress further inside the plasmas in TJ-II in the future.

Chapter 6

Influence of magnetic topology on long-range spatial and temporal correlation in stellarator and reversed field pinch plasmas *

The influence of magnetic topology on long-range spatial and temporal correlation has been studied using multi-Langmuir probe systems in the TJ-II stellarator and RFX-mod reversed field pinch. During dynamic magnetic configuration scan in TJ-II, long-range spatial correlation and temporal correlation (Hurst exponent) were found to change according to the magnetic configuration near the low-order rational surface. In RFX-mod, long-range spatial correlation was found to increase both inwards and outwards with respect to the edge magnetic islands radial position. These findings indicate that magnetic topology has an effect on the formation of large coherent structures and the local particle dynamics.

6.1 Introduction

The influence of magnetic topology on plasma performance has attracted considerable interest in magnetic fusion research [9]. In stellarator devices, global confinement and the accessibility to improved confinement regimes (H-mode) is strongly linked to magnetic topology [120]. In particular low order rational surfaces have been found to affect the generation of Reynolds stress and sheared flow [121–123]. In tokamak, magnetic perturbation is considered an important tool to control the ELMs [124]. In reversed field pinch (RFP), a very in-

*This chapter is based on the manuscript to be submitted for publication

teresting process/phenomenon is the spontaneous transition from the multiple-helicity states (higher level of magnetic chaos) to the single-helicity state (lower level of magnetic chaos) showing the importance of magnetic topology in plasma confinement [75]. In RFX-mod, it has been found that magnetic topology (helical perturbation) has an influence on the edge plasma flow and small-scale turbulence [125, 126], as well as on the plasma transport and electromagnetic filaments [117].

Long-range spatial and temporal correlations are important elements in the understanding of plasma transport. In the present study, long-range temporal correlation is quantified by the Hurst exponent [127], and long-range spatial correlation (LRC) is measured by the cross-correlation between measurements of two toroidally/poloidally separated probes. In TJ-II, the study of the magnetic topology effect on LRC at low density ($0.4 \times 10^{19}\ m^{-3}$) ECRH plasmas shows the role of magnetic topology effect on connection length, thus affecting LRC [128]. Long-range correlation can be due to several mechanisms, e.g. zonal flow, GAMs, MHD modes and drift-wave turbulence [128]. Hurst exponent has been proposed to quantify the long-range temporal correlation in fusion plasmas [83]. The impact of a rational surface on the long-range temporal correlation has been studied at the gradient region of plasma [129, 130]. Due to the complicated magnetic edge topology, LRC is more difficult to detect in RFX-mod [92]. The improved magnetic boundary control [131] allows the operation of RFX-mod at the RFP configuration with the reversal surface much closer to the first wall. The first experimental detection of LRC was then reported at the edge of RFX-mod recently [132]. Although extensive research has been done on this topic, it is not clear how the magnetic topology affects large coherent structures (e.g. zonal flows), and transport behaviour.

In this paper, we study the effect of magnetic topology effect on the formation of large coherent flows and particle dynamics in TJ-II and RFX-mod with Langmuir probe diagnostics.

6.2 Experimental methods

6.2.1 Experimental setup in TJ-II

TJ-II is a four-field-period low magnetic shear helical-axis stellarator with major radius $\langle R \rangle = 1.5\ m$, minor radius $\langle a \rangle \leq 0.22\ m$, and toroidal magnetic field $B_T = 1\ T$. A distinct feature of TJ-II is its central coil which consist of a circular coil wrapped with an $l = 1$ winding [71]. This design provides TJ-II the flexibility in variation of rotational transform in a wide range. TJ-II has been upgraded to change the currents in the coils dynamically:

the current can be ramped during a discharge. In this way, the magnetic configuration can be changed dynamically, the so-called dynamic configuration scan. First dynamic configuration scan in TJ-II was reported in [133]. During a dynamic scan, rational surfaces can be moved radially, as shown in figure 6.1.

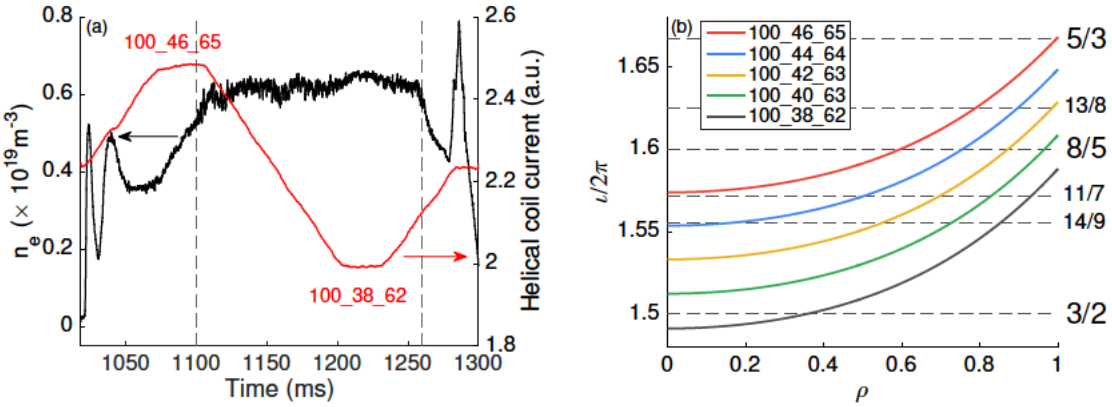

Figure 6.1. Dynamic configuration scan in TJ-II: (a) time evolution of line-averaged density and helical coil current; (b) iota profiles in different configurations.

Two Langmuir probe arrays are installed at reciprocating systems in Sectors D (ϕ = 38.2°) and B (ϕ = 195°) toroidally separated by 160° (5 m): one is a rake probe with 12 tips radially spaced 3 mm; the other is fixed at a radial position. These settings allow simultaneous measurements of edge plasma fluctuations at different toroidal positions.

The probe measurements were carried out during dynamic configuration scans, changing the magnetic configuration in a narrow iota range (5-10%), with the presence of different low rational surfaces (n/m = 8/5, 3/2, 5/3). During the fine iota scan, other plasma configuration parameters remain basically unchanged: the volume changes less than 5% and the magnetic axis displacement is lower than 0.7 cm between configurations of each scan. Good density control was obtained during the dynamic configuration scan for plasma densities around $0.6\times10^{19}\,m^{-3}$ (i.e. below the plasma density at which edge sheared flows are spontaneously developed in the TJ-II stellarator in the considered range of configurations [134]).

6.2.2 Experimental setup in RFX-mod

RFX-mod is a circular cross-section reversed field pinch (RFP) with a major radius R = 2 m and minor radius a = 0.459 m. The device is equipped with a feedback control system consisting of 192 (4 poloidal × 48 toroidal) independently powered saddle coils and fully covering the torus [73]. By the active control of radial magnetic field at the plasma boundary, RFX-mod has achieved high plasma current (I_p = 2 MA).

There are two insertable probes installed on RFX-mod: one is dubbed 'U-probe' [135], the other is a Gundestrup probe [136]. They are toroidally separated by 30° (1 m apart). U-probe consists of two fingers, each equipped with a 2D (radial and toroidal) array with 5 rows of probe tips radially spaced 6 mm. Both probes are insertable and can be moved on a shot-to-shot basis up to 50 mm inside the plasma.

6.2.3 The RFX-mod magnetic topology

Electrostatic features in the RFP are usually found to be strongly connected to the underlying magnetic topology. At low plasma currents, the RFX-mod core magnetic topology is characterised by a chaotic configuration (the so called multiple helicity state) due to the superposition of different tearing modes with same poloidal m=1 number and various toroidal n numbers. At higher plasma current ($I_P > 1$ MA) plasma experiences a spontaneous transition from the multiple-helicity state into a quasi-single-helicity (QSH) state (dominated by the m=1, n=-7 tearing mode), in which plasma is in 3D helical configuration and plasma confinement improves. When the axis of the dominant magnetic island merges with the main magnetic axis, the state is called single-helical-axis (SHAx) state [75]. A magnetic topology similar to high plasma current QSH states can also be induced at low current ($I_P < 500$ kA) by applying a helical boundary condition through the feedback control system [131]. The low current of this induced helical states make the plasma edge accessible to probe measurements.

The RFX-mod edge magnetic topology is, instead characterised by the presence of a $q = 0$ surface whose radial position is defined by the inversion of the toroidal magnetic field (a peculiar feature of the RFP configuration). The $q = 0$ surface is a resonant surface for all the $m = 0$ tearing modes. These modes form a chain of magnetic islands in the plasma edge. The radial position of these $m = 0$ island can be adjusted by setting the edge toroidal and poloidal magnetic field, $B_\phi(a)$ and $B_\theta(a)$, by external coil system. Two conditions, the 'shallow reversal' and 'deeper reversal' distinguished by the reversal parameter $F = B_\phi(a)/\langle B_\phi \rangle$, are considered. For the shallow case, with $-0.12 < F < 0$ the $m = 0$ island is close to the wall; for the deeper case, with $-0.2 < F < -0.12$ the $m = 0$ island is well detached from the wall [137].

The radial position of $m = 0$ islands was estimated by modelling the edge magnetic topology with a Field Line Tracing code named FLiT [138]. The magnetic topology is reconstructed by matching the equilibrium solution of a Newcomb-like solver [139] with the magnetic measurements of a set of 48×4 external magnetic probes.

6.3 Data analysis

Long-range spatial correlation (LRC) measures the long-distance similarity of plasma fluctuations. It is a standard tool to detect large coherent structures (e.g. zonal flows, GAMs) in plasma turbulence [92, 91]. To quantify LRC, we compute the normalised cross-correlation between two toroidally separated signals x(t) and y(t) as follows:

$$\gamma_{xy}(\tau) = \frac{E\{[x(t+\tau) - \bar{x}][y(t) - \bar{y}]\}}{\sqrt{E\{[x(t) - \bar{x}]^2\}.E\{[y(t) - \bar{y}]^2\}}} \tag{6.1}$$

The LRC between these two signals is evaluated at zero time delay,i.e. $\gamma_{xy}(\tau = 0)$.

Long-range temporal correlation is characterised by the algebraic decay of the auto-correlation of a fluctuation signal for long time lags. It has been demonstrated [83] that long-range temporal correlation can be effectively estimated by calculating the Hurst exponent from the rescaled range statistic (R/S) [140]. The value of Hurst exponent also indicates the degree of deviation of transport behaviour from the normal diffusive transport [129]. The Hurst exponent of a signal is computed as follows. Consider a signal, X_i, of length n, we compute its standard deviation $S(n)$, and accumulated deviation from the mean $W_K = X_1 + X_2 + \cdots + X_K - k\overline{X}(n)$. R/S is defined as [83]:

$$\frac{R(n)}{S(n)} = \frac{max(0, W_1, W_2, \ldots, W_n) - min(0, W_1, W_2, \ldots, W_n)}{\sqrt{S^2(n)}} \tag{6.2}$$

By fitting the mean R/S with length n, $E\left[\frac{R(n)}{S(n)}\right] \xrightarrow{n\to\infty} \lambda n^H$, we obtain the Hurst exponent H. The value of Hurst exponent $0 < \mathrm{H} < 0.5$ indicates subdiffusion; $H = 0.5$, normal diffusion and $0.5 < \mathrm{H} < 1$, superdiffusion [83, 141]. An example of obtaining the Hurst exponent by fitting the R/S curve is shown in figure 6.2.

6.4 Results

6.4.1 Results from TJ-II

LRC in TJ-II

Figure 6.3 compares the time evolution of floating potential profile measured by the rake probe during the dynamic magnetic configuration scan ($\iota(a)/2\pi = 1.67 - 1.6$) and at a fixed magnetic configuration ($\iota(a)/2\pi = 1.63$), in which the rational surface 8/5 is located at the edge. During this experiment, the probe 1 (rake probe) was located in the plasma edge region

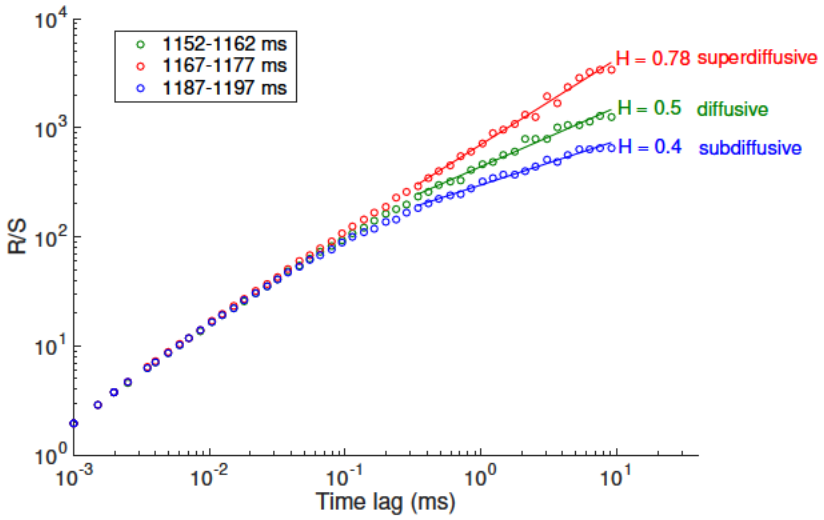

Figure 6.2. An example of obtaining the Hurst exponent by fitting R/S for superdiffusion, diffusion and subdiffusion (#24747, TJ-II)

(the probe measurement region covers $0.82 < \rho = r/a < 1$), whereas the probe 2 was located at a fixed position $r/a \sim 0.85$. As can be seen, minor changes in the iota value result in strong modifications in the floating profiles and their gradients. A systematic study of the influence of dynamic configuration scan on the plasma profiles has been reported [142].

Figure 6.4 shows the time evolution of LRC during the dynamic configuration scan and at fixed magnetic configuration with plasma density at $n_e \sim 0.6 \times 10^{19}\,m^{-3}$. The LRC show an intermittent character and strong modulation during the magnetic configuration scan. LRC is characterised by the floating potential fluctuation measured by probe 1 and probe 2, with frequency below 20 kHz.

LRC between two toroidally separated signals can be attributed to various mechanisms (e.g. MHD modes, zonal flow and drift-wave turbulence) [128]. Previous studies suggest that LRC can be related to the parallel and perpendicular size of the structure of drift-wave turbulence (connection length) in low density ECRH plasmas ($n_e \sim 0.4 \times 10^{19}\,m^{-3}$), in which zonal flow was considered insignificant. However, at higher density ($n_e \geq 0.6 \times 10^{19}\,m^{-3}$) additional LRC (may be due to zonal flows) has been observed [128].

To clarify the role of zonal flow in the development of LRC, we use biorthogonal decomposition (BOD) to study the correlation properties. BOD has been first proposed for the identification of zonal flow-like structure based on experiments in TJ-II [113]. We briefly summarise the method below.

With multipoint measurements (e.g. probe array), we obtain a data matrix $Y(i, j)$, where the index $i = 1, \ldots, N$ labels the time and $j = 1, \ldots, M$ the detector (probe tip). BOD decomposes the data matrix $Y(i, j)$ as follows:

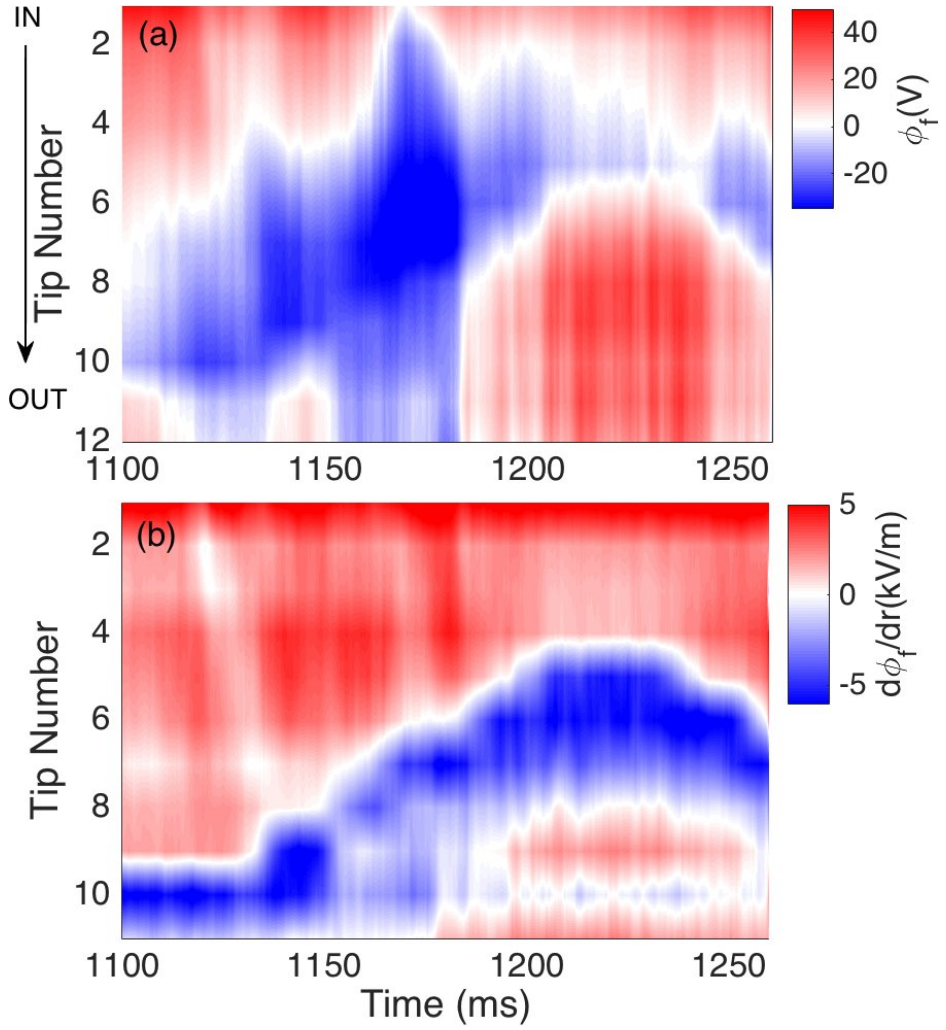

Figure 6.3. Time evolution of (a) floating potential profile and (b) radial electric field profile in TJ-II during dynamic configuration scan.

$$Y(i,j) = \sum_k \lambda_k \Psi_k(i) \Phi_k(j) \tag{6.3}$$

where ψ_k is called a 'chrono' (a temporal function) and ϕ_k a 'topo' (a spatial function). Chronos and topos satisfy the orthogonality relations: $\sum_i \psi_k(i)\psi_l(i) = \sum_j \phi_k(j)\phi_l(j) = \delta_{kl}$. ψ_k and ϕ_k are ordered by the eigenvalue of λ_k, which represents the contribution of mode k to the total fluctuation energy. Further analysis of the chronos and topos gives us information about spectral, correlation and spatial structure properties of each mode.

Figure 6.5 shows the BOD analysis of floating potentials measured by probe 1 and probe 2. As can be seen, the main contribution to the LRC comes from the fluctuations with frequency below 20 kHz (figure 6.5(c)). The spatial structure of this contribution, the topo

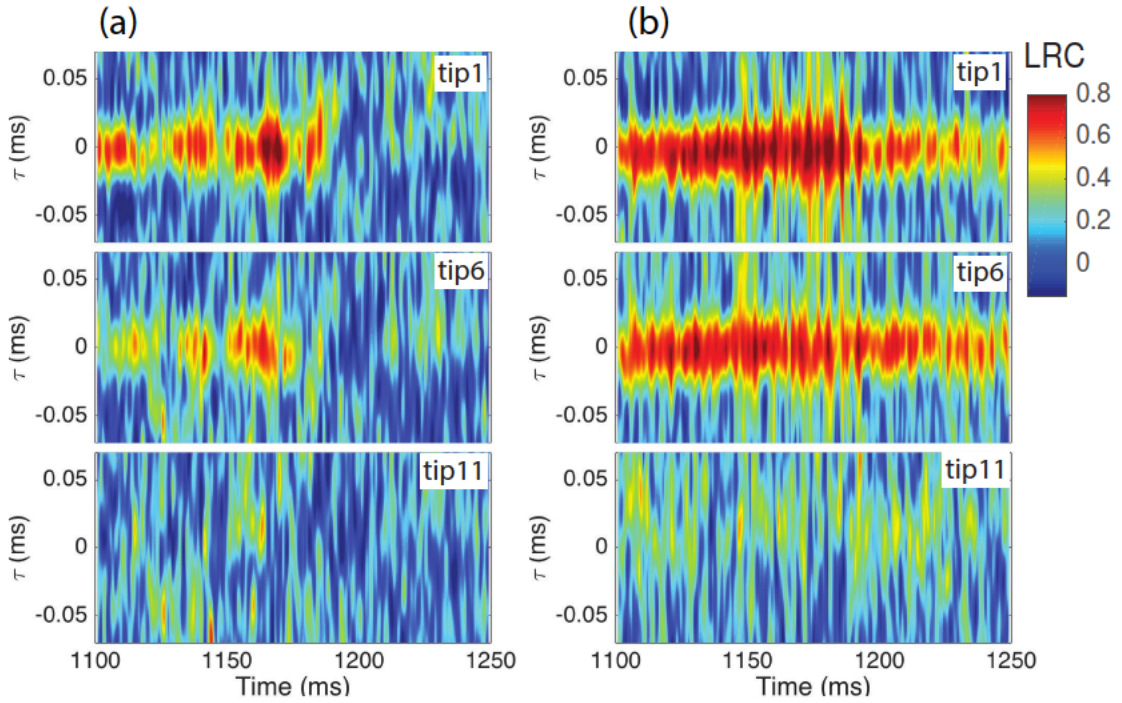

Figure 6.4. Comparison of the time evolution of long-range correlation for plasmas during dynamic configuration scan (a) and fixed configuration (b) in TJ-II.

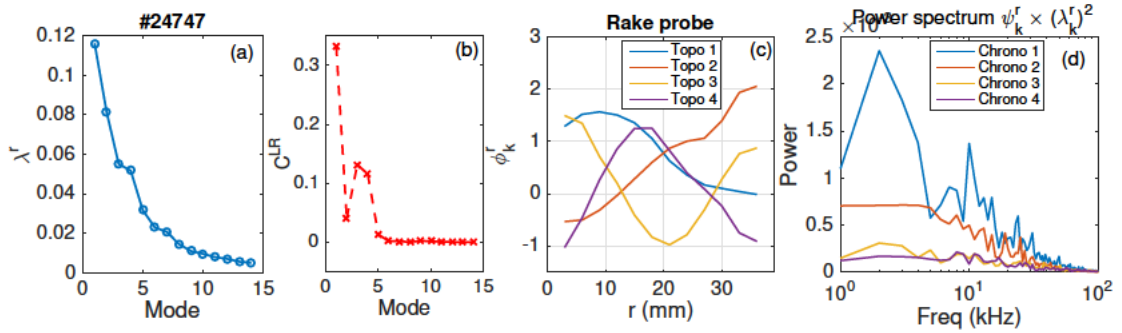

Figure 6.5. (a) BOD eigenvalues (b) long-range correlation contribution of each mode, (c) spectra of the chronos of first four BOD modes, and (d) topos of the first four BOD modes.(#24747, TJ-II)

of this BOD mode is edge localised. This shows the features of zonal flow. It confirms that zonal flows are the main contribution to LRC during the dynamic configuration scan at high density ($n_e \geq 0.6 \times 10^{19}$ m^{-3}). Therefore, the change of LRC during the magnetic configuration scan mainly reflect the change of zonal flow.

Hurst exponent in TJ-II

Long-range temporal correlation was estimated by the Hurst exponent. We computed the Hurst exponent with 12 floating potential signals measured by probe 1 (the rake). The probe

measurements cover the region $0.82 < \rho < 1$. Figure 6.6 shows the time evolution of Hurst exponent of floating potential signals measured by the rake probe during the dynamic configuration scan. Several diagonal ridges of high Hurst exponent can be seen. By fitting one of the ridges, we estimated the propagation speed is about 1 m/s. Interestingly, during the dynamic configuration scan, it takes $\Delta t \sim 100\,ms$ for the rational surfaces propagating a distance from $\rho \sim 0.5$ to $\rho \sim 1$. We can estimate the propagation speed as $a\Delta\rho/\Delta t \sim 1\,m/s$. Thus, these ridges probably correspond to the radial motion of the rational surface (5/8) during the configuration scan, thus reflecting the influence of the rational surface on the long-range temporal correlation.

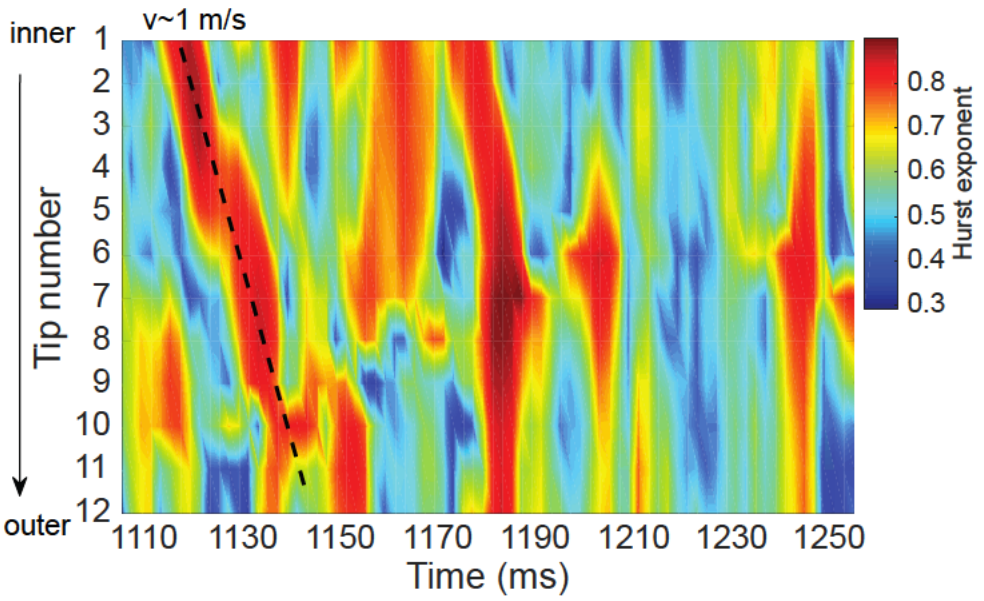

Figure 6.6. Time evolution of Hurst exponents of floating potential signals during dynamic configuration scan in TJ-II. (#24752)

A previous study has shown that low order rational surfaces are related to small transport barriers [143]. These small transport barriers tend to trap particles, leading to subdiffusive behaviour. Because the collisional transport has diffusive behaviour, the subdiffusive regions are less noticeable. This probably explains why the superdiffusive regions are more pronounced. This result is in agreement with [129].

Figure 6 shows a comparison of the time evolution of LRC and Hurst exponent based the measured by the first tip of probe 1. This indicates that the LRC and the Hurst exponent are linked and associated with rational surfaces, in good agreement with the results presented in [129], which shows radial and linked profiles of Hurst exponent and poloidal velocity for turbulence in a resistive MHD model.

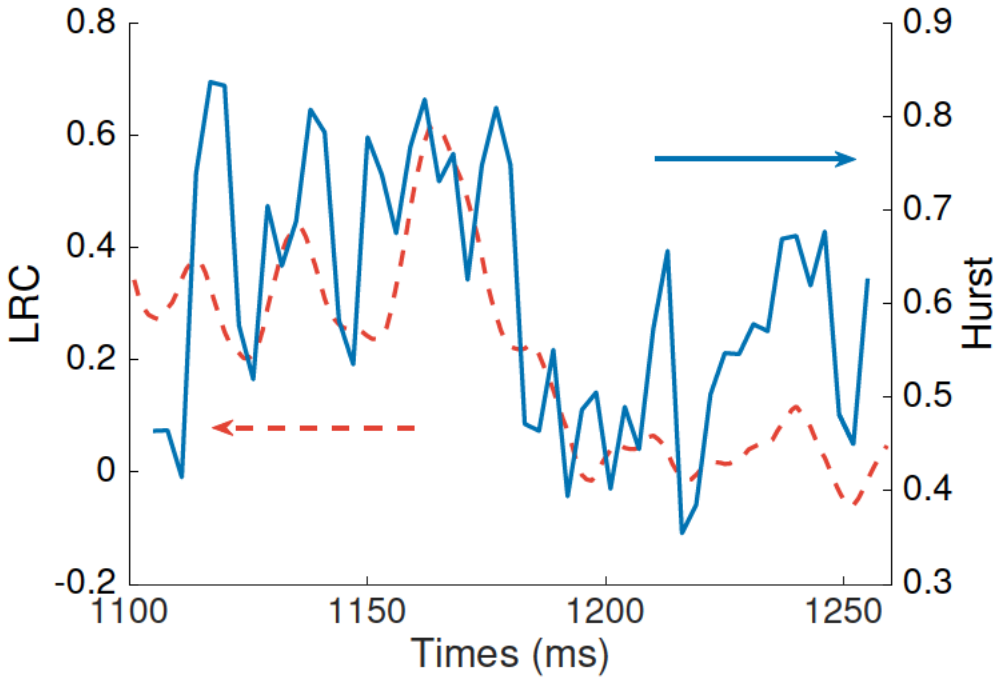

Figure 6.7. Comparison of the time evolution of LRC and Hurst exponent during dynamic configuration scan in TJ-II.

6.4.2 Results from RFX-mod

LRC in RFX-mod

Due to the complexity of the edge magnetic topology, especially in the presence of m=0 islands and edge stochasticity by the multiple helicity state, detection of LRC has been found to be more difficult in RFX-mod than in tokamaks and stellarators [92]. With the improved understanding the role of m=0 at the edge, detectable LRC has been observed at the radial position inward with respect to the m=0 islands, and systematically increase inward in the probe measurement region [132].

Figure 6.8 shows the profiles (taking the $m = 0$ island position as a reference) of LRC in H and D plasmas in RFX-mod. The LRC was calculated with the probe signals measured by the two toroidally separated probe systems. For the shallow case, LRCs maintained at the noise level at around the m=0 island region, and tend to increase when the measurements extend beyond the island region. This is in agreement with previous study [132]. For the deeper case, an increase of LRC takes place outward beyond the island region. From this analysis, we can estimate the width of m=0 to be less than 2 cm. The island seems to be well separated from the wall even at the shallow reversal.

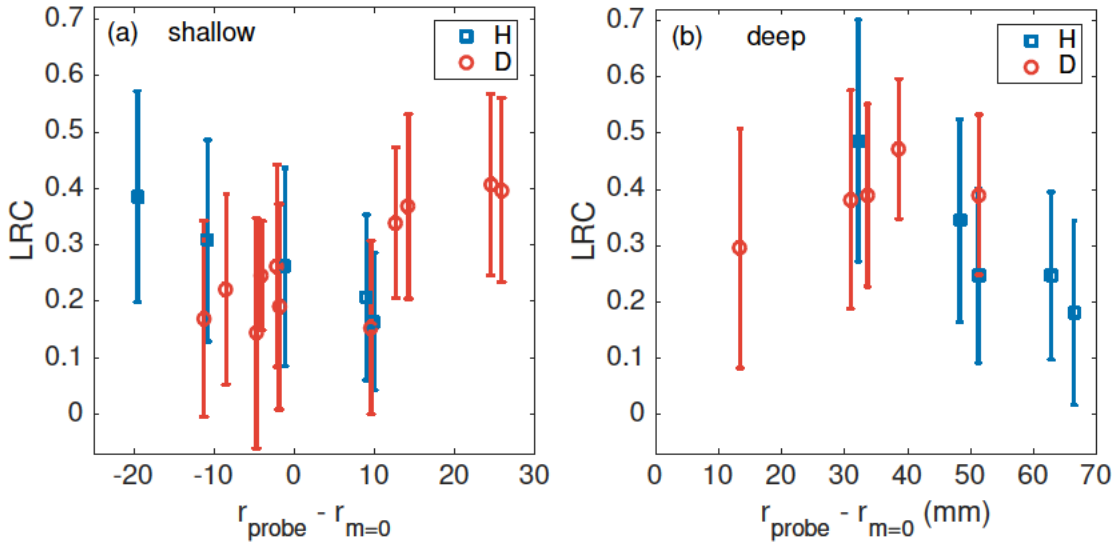

Figure 6.8. LRC in RFX-mod for the case of (a) shallow and (b) deep $m = 0$ magnetic island. Each point corresponds to one shot. The error bars indicate the variation of the correlation coefficient in the time window (flat top).

From figure 6.8 we can also see that there is no clear difference in the level of LRC in H and D plasmas. However, recent study of isotope effect reported that at high current ($I_P > 1$ MA), D plasma has better confinement than the H plasma [144]. The isotope effect has not been reported at low current ($I_P < 500$ kA) plasmas, in which the probe measurements take place.

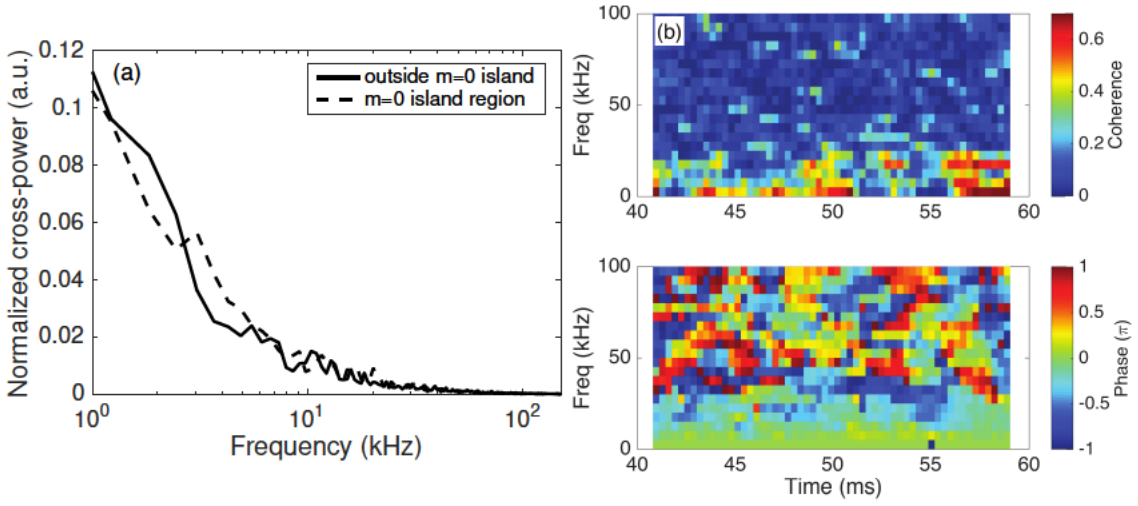

Figure 6.9. (a) Frequency spectra normalised by their total power; (b) coherence and phase between floating potential signals measured by the U-probe and the Gundestrup probe. (#34058, RFX-mod)

In figure 6.9, we plot the normalised average frequency spectra of shots at the island and outside the island region. It shows that the LRCs are dominated by frequencies below 20

kHz. The phase difference between the toroidally separated probe is around zero indicating the toroidal symmetry of the low frequency 'mode'.

Hurst exponent in RFX-mod

In this section we present a preliminary analysis of the effect of helical magnetic perturbation on Hurst exponent at the edge of RFX-mod. In the present study, a helical magnetic perturbation (m=1, n=-7), toroidally rotating with frequency about 10 Hz, was applied. Under this condition, local plasma properties exhibit an oscillation, reflecting the rotating helical perturbation. To characterise the phase relation with the magnetic perturbation, the helical angle has been introduced [126]. The helical angle is defined as:

$$u_{m,n}(t) = m\theta - n\phi + \varphi^{m,n}(t)$$

where $\varphi^{m,n}$ is the proper phase of the magnetic perturbation.

Figure 6.10 [126] illustrates the magnetic flux for the (1,−7) magnetic deformation as a function of the helical angle $u_{1,-7}$ and the radial displacement r/a = 1. The definition of the angle is such that the O-point appears at $u = \pi/2$ and the X-point at $u = 3\pi/2$.

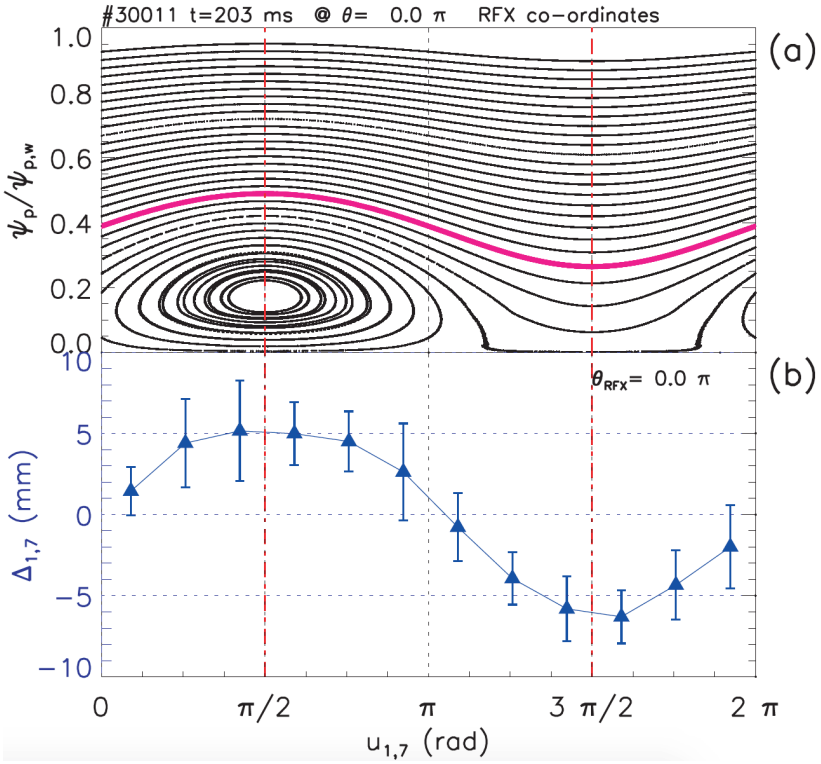

Figure 6.10. (a) Magnetic flux for the (1,−7) magnetic deformation as a function of the helical angle $u_{1,-7}$; (b) radial displacement at r/a = 1, as a function of $u_{1,-7}$ [126].

Five floating potential signals measured by one radial column tips from the U-probe were used for the analysis of Hurst exponent. Figure 6.11 shows the evolution of the Hurst exponent distribution with the helical angle of magnetic perturbation. On average the Hurst exponent is above H = 0.5. At the region of $\pi < u_{1,-7} < 3\pi/2$, the Hurst exponent decreases and tends to be H < 0.5, which is associated with subdiffusive behavior. This may be explained as follows. During the magnetic perturbation, the $m = 0$ islands are coupled with the perturbation [132]. Around the islands regions, small transport barriers may have been formed and trapped particles, leading to subdiffusive behavior.

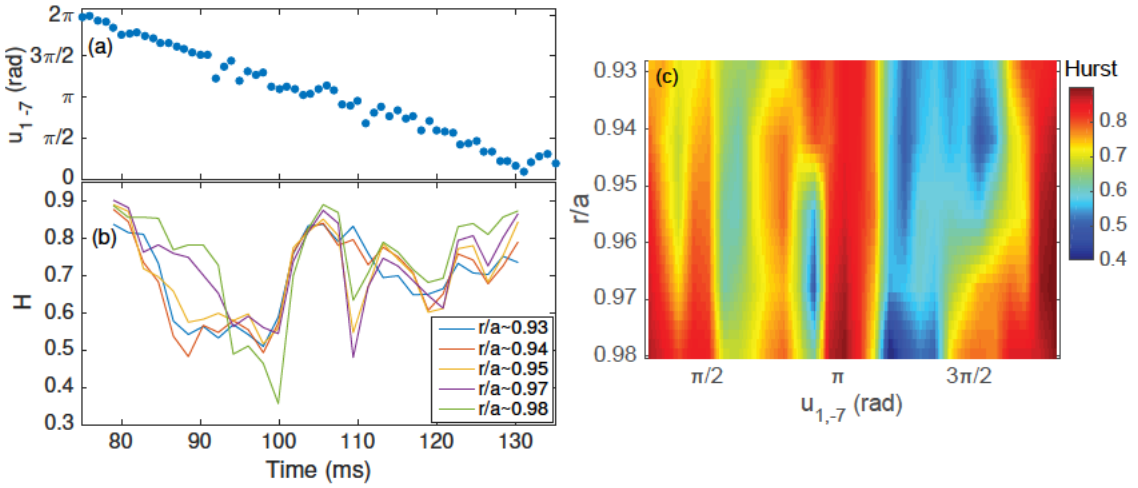

Figure 6.11. (a) Phase angle versus time; (b) time evolution of Hurst exponents of floating potential measured at five radial positions; (c) the Hurst exponent in helical angle and all probe tips. (#38138)

6.5 Conclusion

We have studied the influences of magnetic topology effects on long-range temporal correlation (Hurst) and spatial correlations (LRC) in the TJ-II stellarator and the RFX-mod reversed field pinch. In TJ-II in the ECRH plasma around the critical density ($n_e \geq 0.6 \times 10^{19}\ m^{-3}$), clear change of LRC with magnetic topology has been found during the dynamic configuration. The propagation of rational surface was captured by the Hurst exponent distribution. In RFX-mod LRC has been detected both inwards and outwards beyond the $m = 0$ island, which is complementary to previous study [132]. A preliminary analysis of Hurst exponent at the edge during helical boundary perturbation shows that there might be small transport barrier at m=0 island region. Results from TJ-II and RFX-mod show that magnetic topology has effect on both the formation of large coherent structures and local particle dynamics.

Chapter 7

Direct experimental evidence of asymmetry in the modulation of potential in magnetic flux surfaces in the TJ-II stellarator*

We have developed a new strategy for studying potential asymmetries in magnetic flux surfaces based on edge electrode biasing and dual-Langmuir probe measurements in the ion-root Neutral Beam heated plasmas in the TJ-II stellarator. Two criteria were used to identify the asymmetries. First, matching the floating potential measured by the two poloidally / toroidally distant probe arrays. Experimental findings show that there is no way to match both the biased and unbiased half-cycles of the floating potentials. Second, taking advantage of the amplification of Long-Range Correlations (LRC) by biasing, the amplitude of LRC was used to label magnetic flux surfaces. In both cases, the level of asymmetry was found to increase with electron temperature reaching values above 20 V. These findings are complementary to previous results obtained in the proximity of the electron-ion root transition in Electron Cyclotron Resonance heated plasmas where potential asymmetries were first reported [M.A. Pedrosa *et al* 2015 *Nucl. Fusion* **55** 052001]. Then, plasma potential asymmetries seem to be ubiquitous in the TJ-II stellarator.

*This chapter is based on the manuscript to be submitted to Nuclear Fusion

7.1 Introduction

Power exhaust and impurity are critical issues for the development of fusion energy [108]. Core impurity accumulation has a negative impact on fusion performance due to the increase in radiation-induced losses as well as plasma dilution, whereas edge impurity radiation can affect the maximum attainable edge pedestal temperature with a direct impact on global performance due to profile stiffness. In parallel, high divertor radiation level will be required in a fusion reactor to avoid thermal overload of materials. This issue drives the need to understand the role of impurity seeding to reduce the power heat load in plasma-facing components while avoiding core impurity accumulation.

The measurement and modelling of impurity density asymmetries can provide an indirect validation of model prediction on radial impurity transport. The localisation of impurities in a flux surface depends on the location of magnetic and electrostatic wells, as well as on ion-impurity friction, all of which can be important players in the radial transport of impurities [69, 145]. The understanding of these asymmetries can be a milestone in the progress of our investigation of impurity transport and accumulation in fusion toroidal devices.

Quantifying the level of asymmetry in plasma properties requires accurate alignment of plasma profiles. Recently, efforts have been made to apply correlation tools and magnetic equilibrium reconstruction to achieve satisfactory alignment in plasma profiles [68, 146]. These measurements are a real challenge because small radial misalignment (in the order of few millimeters) could give rise to large uncertainties in the interpretation of the level of asymmetry. In particular, first direct experimental observations of electrostatic potential variations within the same magnetic flux surface has been reported in the electron-root plasmas sustained by Electron Cyclotron Resonance (ECR) heated plasmas [68]. The level of asymmetry has been found to reduce as the electron temperature decreases. The order of magnitude (in the order of tens of volts) as well as the observed dependencies are well reproduced by neoclassical Monte Carlo calculations.

In this paper we present a new strategy for studying potential asymmetries in plasma regimes with radially inwards radial electric fields (i.e. ion root) using electrode biasing and dual-Langmuir probe measurements of Long-Range Correlations (LRC) in the TJ-II stellarator.

7.2 Experimental methods

Experiments were carried out in the TJ-II stellarator in pure Neutral Beam Injection (NBI) heated plasmas (P_{NBI} port-through $\approx 450\,kW$, magnetic field $B_T = 1T$, plasma minor ra-

dius $\langle a \rangle \leq 0.22$ m) initiated by ECR heating ($P_{ECRH} \leq 400$ kW). The TJ-II vacuum vessel is divided into four sectors that are marked in figure 7.1(a) as Sector A, B, C and D, corresponding to its four-fold toroidal symmetry. A graphite electrode was installed on a reciprocating probe drive at Sector A8 and biased with respect to a radially movable limiter at sector C3. In the present experiments the electrode was inserted 3 cm, corresponding to $\rho \sim 0.85$ inside the Last Closed Flux Surface (LCFS) whereas the limiter was kept at the LCFS ($\rho = 1$).

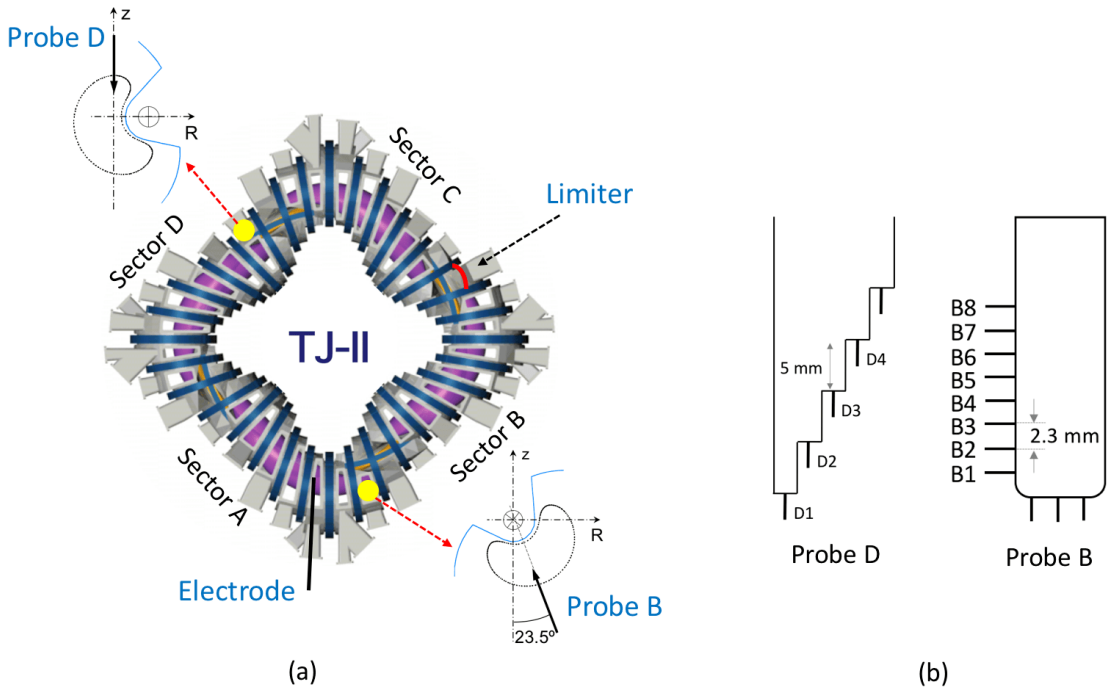

Figure 7.1. (a) Schematic view of TJ-II showing the locations of two Langmuir probe systems, electrode, and limiter; (b) configuration of the tips on probe D and probe B.

The electrode was biased with respect to the limiter with an AC voltage during plasma discharges. The waveform of the biasing voltage is a negative half-wave rectified triangular wave, i.e. in each period, half-cycle unbiased or with $V_{bias} = 0$ and half-cycle biased with a triangular shape peaked at $V_{bias} = -340$ V as shown in Figure 7.2(a). The frequency of the biasing waveform is adjustable and frequencies 40, 60 and 80 Hz were chosen for the present experiments. In this way, the plasma properties in the zero biasing phase can serve as a reference to compare with those in the biasing phase during one discharge.

Two Langmuir probe arrays are installed at reciprocating systems in Sectors D ($\phi = 38.2°$) and Sector B ($\phi = 195°$), from which we named the probes: 'Probe D' and 'Probe B'. The configurations of Probe D and Probe B are shown in figure 7.1(b). Probe D is a 2D probe array consisting of tips radially spaced 5 mm and poloidally spaced 3 mm. In each row (poloidal), three of the tips were operated in a triple probe configuration: the first tip

was set to measure floating potential, whereas the second and third tips were set to measure potential ϕ^+ (with the probe tip positively biased) and ion saturation current (negatively biased) respectively. Thus, the electron temperature can be estimated by $T_e \approx (\phi^+ - \phi_f)/ln2$ [87]. Probe B is a rake probe consisting of eight radial tips spaced 2.3 mm. All tips on Probe B were set to measure floating potentials. This setting allows simultaneously measuring plasma modulations due to the biasing and fluctuations in two poloidally / toroidally distant locations.

Two regions with different magnetic topology can be distinguished around the plasma boundary of fusion plasmas: the plasma region located inwards from the Last Closed Flux Surface (LCFS) and the Scrape-Off layer (SOL) region in which the field lines intersect material surfaces. Near the LCFS sheared flows develop in all magnetic confinement devices due to the reversal in radial electric fields from positive (in the SOL) to negative (in the plasma edge), thus providing a convenient point of reference in the plasma boundary region of fusion devices. The influence of edge sheared flows on turbulence and transport has been a very active area of investigation in nuclear fusion research [28].

7.3 Experimental results

Figure 7.2 shows an example of the time evolution of biasing waveform (negative half-wave rectified triangular wave with frequency 80 Hz and peak -340 V) and floating potentials measured by different tips of the Probe B (the rake). We can see that the floating potential values become more negative for probe tips located further inwards in the plasma edge (i.e. $r < r_{shear}$). The corresponding modulation due to the biasing increases systematically as the radius decreases (i.e. it is larger for tip B1 than for tip B8). The biasing current was measured around 10-20 A.

Figure 7.3 compares the time-averaged floating potential profiles in the unbiased half-cycle ($V_{bias} = 0$) and around the biasing peak ($V_{bias} = -340\,V$) in the biased half-cycle, which were measured by moving Probe B on a shot by shot basis from the plasma edge towards the SOL region. The floating potential is negative in the plasma edge of NBI heated plasmas, in agreement with the ion-root solution of the ambipolarity equation and neoclassical predictions, and rather flat in the SOL region [97]. Thus, near the LCFS $E \times B$ sheared flows are developed providing a convenient point of reference in the plasma boundary region, as shown in figure 7.3. Interestingly, biasing modulation is observed in the plasma edge (i.e. radially inwards the shear location) but not in the SOL side.

Two complementary criteria were used to clarify the existence of potential asymmetries within the same magnetic flux surface.

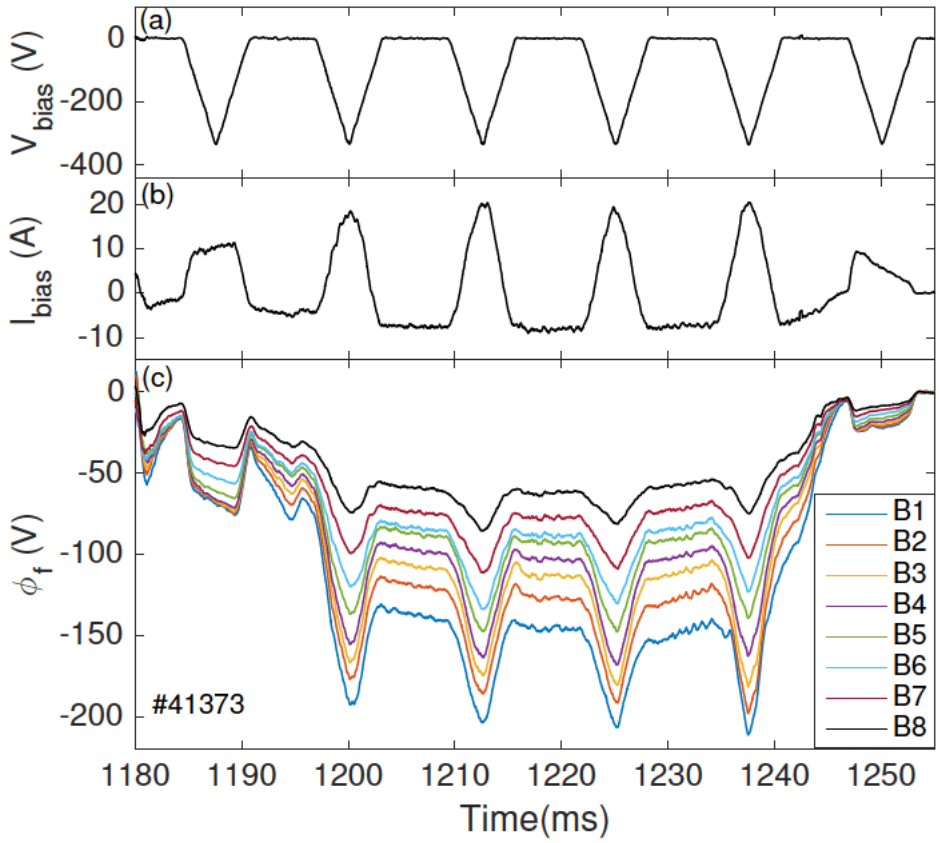

Figure 7.2. Example of the negative half-wave triangular biasing in NBI plasma: (a) biasing voltage, (b) biasing current, and (c) floating potentials measured by probe B. (#41373)

Criterion 1: Is it possible to match the floating potential and amplitude of the potential modulation in measurements carried out simultaneously at two different poloidal / toroidal locations?

We took the floating potential signals at the unbiased half-cycle ($V_{bias} = 0$) as a reference to match floating potential measured by both probes (D and B) and compare the difference in their response during the electrode biasing, as shown in figure 7.4. We found there was no way to match both the biased and unbiased half-cycles by selecting appropriate tips. In the present conditions, the best match of the phase without biasing was between the floating potential measured the first (innermost) tip of Probe D and the fourth tip of Probe B (figure 7.4(c)). We define the level of asymmetry as the difference in the amplitude of biasing modulation in floating potentials between the matched signals, $\Delta\phi_f^{BD} = \phi_f^{B4} - \phi_f^{D1}$. Figure 7.5 shows the dependence of $\Delta\phi_f^{BD}$ on electron temperature measured by the triple probe in Probe D; the level of asymmetry is close to zero at low temperature plasmas, reaching values of up to 20 V as electron temperature increases.

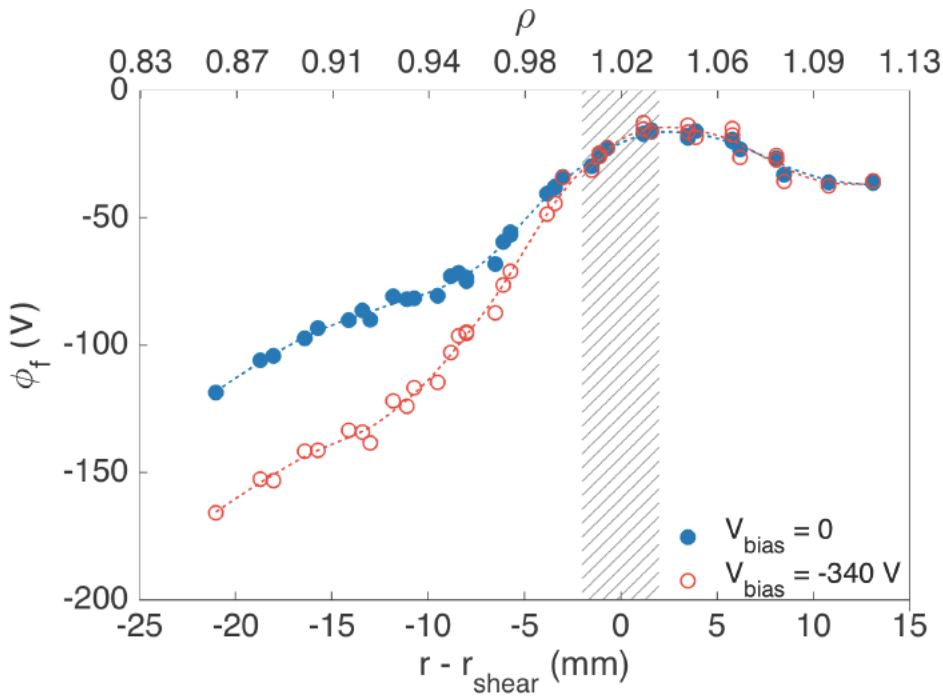

Figure 7.3. Profiles of floating potential measured by probe B during the half-wave biasing at the biasing voltage 0 and negative peak (-340 V). (shots: 41385, 41386, 41387, 41388, 41389, 41390)

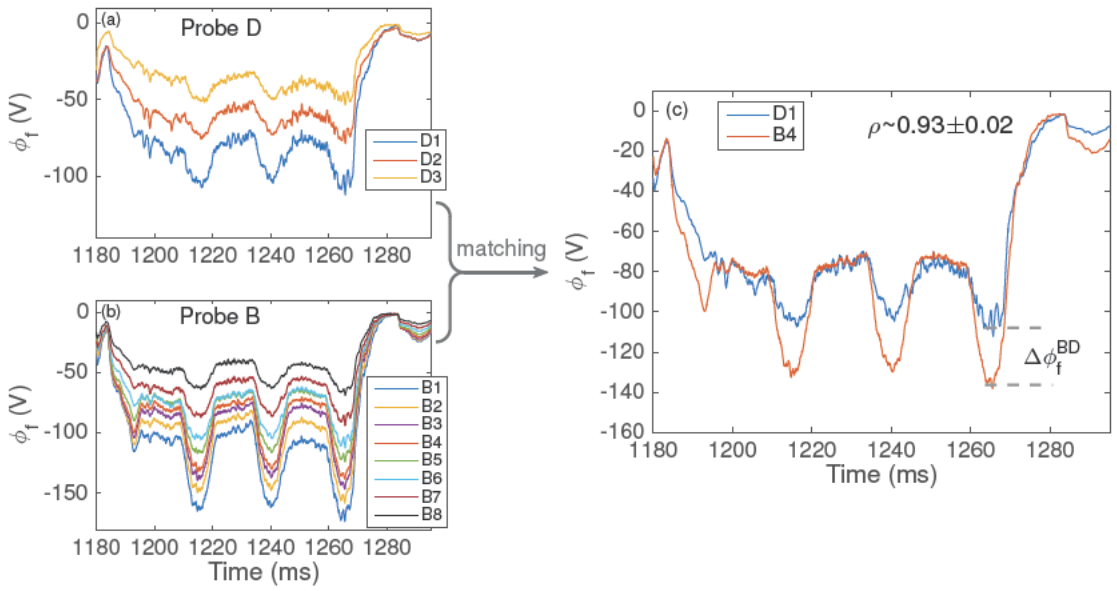

Figure 7.4. (a) Floating potential evolution measured by the first three tips on Probe D, and (b) eight tips on Probe B; (c) the best matching between the measurements from Probe D and Probe B; the difference in modulation between the matched signals is $\Delta\phi_f^{BD}$.(#41363)

Criterion 2: Is there any significant level of potential asymmetry on the magnetic flux surface labeled by the amplitude of Long-Rang Correlation (LRC)?

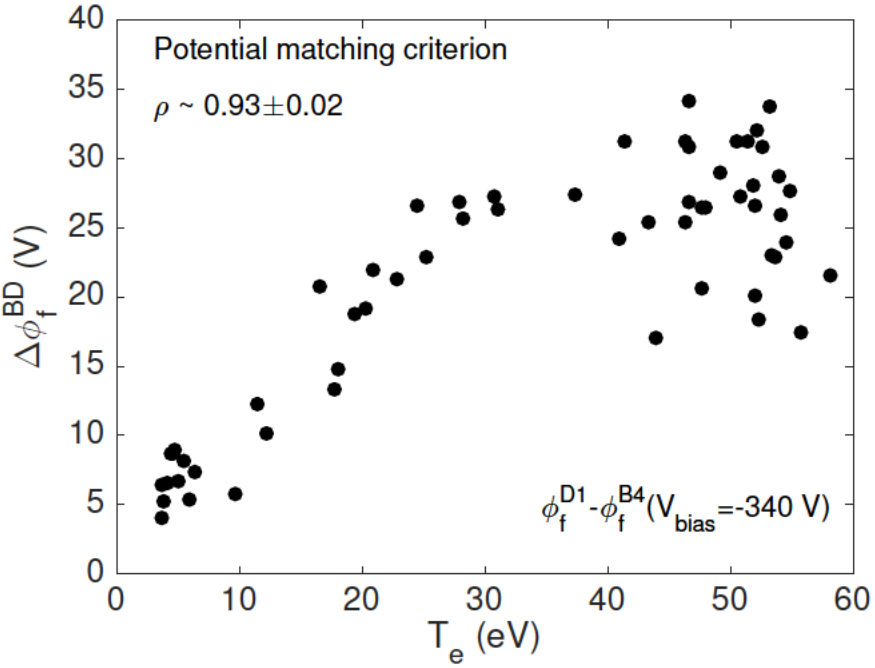

Figure 7.5. Change of the level of asymmetry with electron temperature. (shots: 41363, 41364, 41373, 41374, 41375, 41377, 41378, 41379, 41385)

In this framework, we compute the Long-Range Correlation (LRC) between the innermost tip of Probe D (D1) and all eight tips from Probe B (B1 – B8) after filtering the signals using a band-pass filter such that $1 < f < 20\,\text{kHz}$. The LRC is a measure of the degree of long-range similarity in plasma fluctuations, which was estimated by the normalised cross-correlation between signals as

$$\gamma_{xy}(\tau) = \frac{E\{[x(t+\tau) - \bar{x}][y(t) - \bar{y}]\}}{\sqrt{E\{[x(t) - \bar{x}]^2\}.E\{[y(t) - \bar{y}]^2\}}}$$

at zero time delay, i.e. $\gamma_{xy}(\tau = 0)$.

Figure 7.6 shows the time evolution of the LRC during biasing at two different sweeping frequencies (40 and 60 Hz); the amplitude of LRC is strongly amplified during electrode biasing, reflecting the role of the radial electric field in modifying LRCs, in agreement with previous experiments [51, 42]. The strong amplification of LRC in the biasing phase makes it possible to label magnetic flux surfaces using the LRC amplitude. The feasibility of labelling magnetic flux surfaces by LRC has also been demonstrated in previous experiments [57]. The maximum amplitude of LRC between D1 signal and B rake signals is radially localised at tips B6-B7. We define the level of asymmetry as $\Delta\phi_f^{BD} = \phi_f^{B7} - \phi_f^{D1}$. Figure 7.7 shows the dependence of $\Delta\phi_f^{BD}$ (at $V_{bias} = 0$ and $V_{bias} = -340\,V$) on electron temperature measured

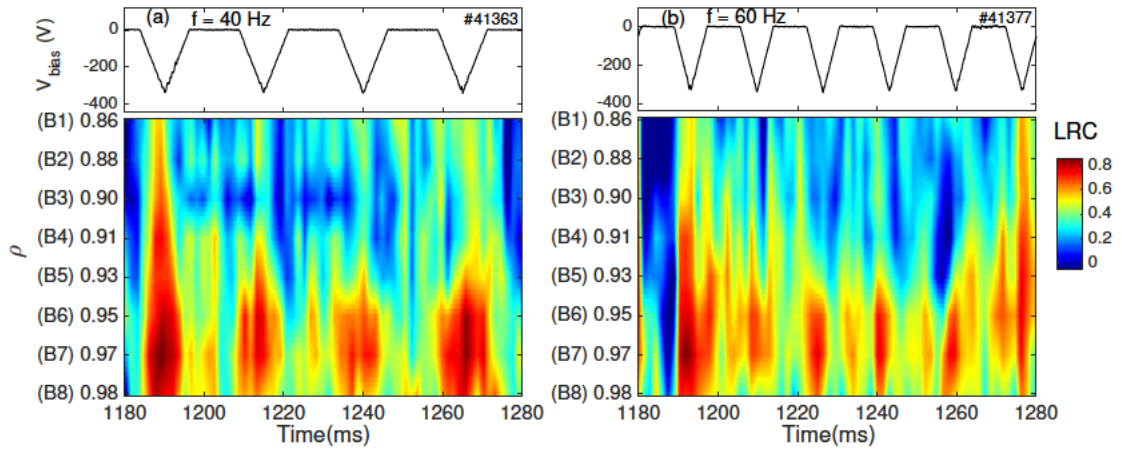

Figure 7.6. Long-range correlation between the fluctuation of signal D1 and signals from Probe B (B1-B8) with frequency of biasing waveform (a) 40 Hz, #41363 and (b) 60 Hz, #41377.

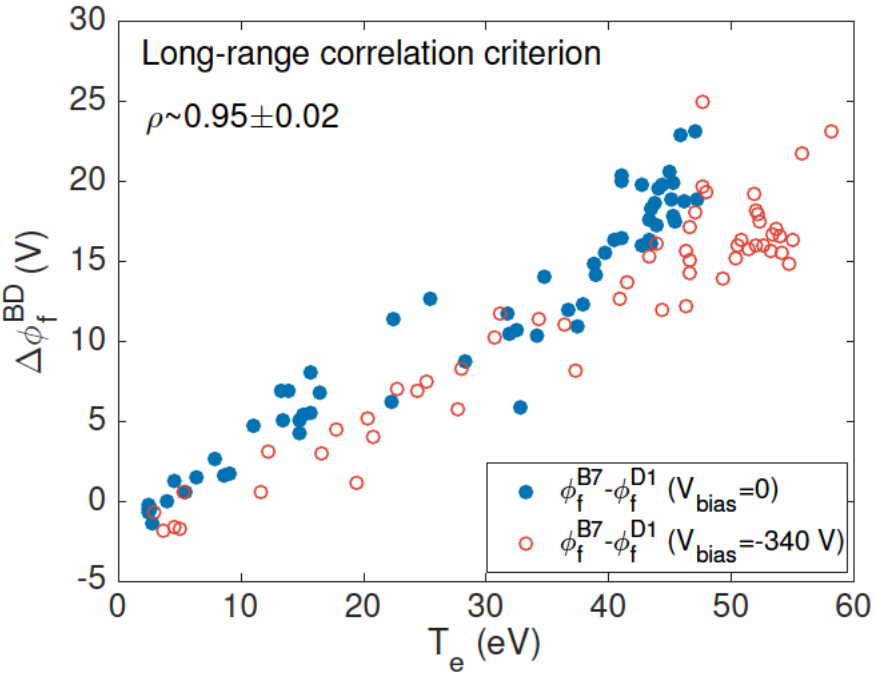

Figure 7.7. Change of the level of asymmetry with electron temperature. (shots: 41363, 41364, 41373, 41374, 41375, 41377, 41378, 41379, 41385)

by the triple probe in Probe D. For both cases, the biased and unbiased phases, $\Delta\phi_f^{BD}$ is at a similar level and increases systematically with electron temperature.

It should be pointed out that the uncertainty in the level of potential asymmetry is limited by the rake probe resolution (2.3 mm). Considering typical radial variation of the potential at the rake probe position (e.g. $E_r < 3$ kV/m at $\rho \approx 0.93$), this uncertainty would be below 7 V.

7.4 Discussion and conclusion

We have investigated the potential asymmetries in the magnetic flux surfaces in the NBI plasmas in the TJ-II stellarator using edge electrode biasing and dual-Langmuir probe measurements. Matching distant floating potential signals and Long-Rang Correlation (LRC) in the biasing phase were used as criteria to clarify the existence of potential asymmetries within the same magnetic flux surface. Experimental findings show that:

1. There is no way to match floating potential values and the amplitude of potential modulation in measurements performed by probe arrays located at different poloidal / toroidal positions. The mismatch in the amplitude of modulation increases with electron temperature reaching values up to 20 V.

2. Using the amplitude of LRC as criterion to match floating potential profiles the mismatch in floating potential profiles in the order of 10–20 V.

It should be noted that the importance of electron temperature corrections in the interpretation of Langmuir probe measurements strongly depends on the measurements under discussion. Temperature correction in the interpretation of Langmuir plasma potential fluctuations can be indeed very relevant [147]. But temperature correction in the searching of plasma flux surface asymmetries should be considered as second order correction as explained in our previous work [68].

Finally, some caveats should be kept in mind when interpreting these experimental findings. It might be questioned whether the observed asymmetries induced by the external actuator (in this case electrode biasing) are reflecting a direct asymmetry due to the plasma itself (e.g. intrinsic asymmetries in plasma potential on magnetic flux surfaces) or/and being introduced by the electrode. The fact that an asymmetry is observed at $V_{bias} = 0$ using the LRC criterion (as demonstrated previously) and that the level of asymmetry does not significantly change with biasing (Figure 7.7) suggests that the asymmetry is natural and not caused by biasing.

In conclusion, significant differences (in the order of 10 V) between the floating potential at the two probe locations were observed in the ion-root NBI heated plasmas in the TJ-II stellarator. These findings are complementary with previous results obtained in the proximity of the electron-ion root transition in ECR heated plasmas where floating potential asymmetries in the order of 20 V were reported [68]. Thus, assuming that asymmetries in electron temperature are a second order correction, plasma potential asymmetries seem to be ubiquitous in the TJ-II stellarator.

Part IV

Conclusion

Chapter 8

Conclusions

The focus of this thesis is on the interplay between large scale flows, turbulence and confinement in fusion plasmas. A set of experimental investigations aimed at improving our understanding of this interplay has been conducted in tokamak (ISTTOK), stellarator (TJ-II) and reversed field pinch (RFX-mod) devices. The main results and conclusions are summarised here.

1. The isotope dependence of local plasma turbulence scale and long-range coherent structure has been studied in the TJ-II stellarator and the ISTTOK tokamak. In both ISTTOK and TJ-II, the local turbulent scale increases with isotope mass. This observation would be consistent with gyro-Bohm scaling.

   However, the radial correlation length of fluctuations (L_r) is determined by both local turbulence and large-scale structures (Zonal Flows). It has been found both in tokamaks (ISTTOK) as well as stellarators (TJ-II) that the radial correlation length is dominated by the radial scale of Long Range Correlated (LRC) structures. This observation is particularly important to unravel the dependence of the characteristic radial scale length of turbulent structure with the gyro-radius. In particular, considering that the low-frequency large scale structures (zonal flows or GAMs) do not contribute to plasma transport, once L_r is controlled by LRC, an increasing in L_r would not imply a deleterious impact on transport.

   The amplitude of LRCs has been found to increase with isotope mass in the ISTTOK tokamak, while in the TJ-II stellarator the amplitude of LRCs slightly decreases with isotope mass in the ECRH plasmas. These results provide further insight to understand why the isotope is weaker in stellarators than in tokamaks and the role of magnetic topologies with reduced magnetic viscosity to amplify zonal flows.

2. The influence of magnetic topology on long-range temporal correlation (Hurst exponent) and long-range spatial correlation (LRC) has been studied in the RFX-mod reversed field pinch and the TJ-II stellarator by taking advantages of helical magnetic perturbations in RFX-mod and dynamic configuration scans in TJ-II. It has been found that in both devices the magnetic topology has a clear influence on the generation of LRC and Hurst exponent. This would indicate the role of magnetic topology on flow generation and local particle dynamics.

3. In TJ-II, it has been found that the gradients of magnetic fluctuation induced Maxwell stress increases in the proximity of the L-H transition. The value of the gradient of Maxwell stress is one order of magnitude smaller than the electrostatic fluctuation induced Reynolds stress. These results would indicate the possible role of electromagnetic effects in the trigger of the L-H transition. However, considering that probe measurements have not reached the transport barrier region, the role of Maxwell stress on the flow generation during the L-H transition remains as an open question.

4. A new strategy has been developed for the study of potential asymmetries in magnetic flux surfaces in TJ-II. In this method, electrode biasing is applied at the edge of TJ-II. The response of plasma to the biasing is measured by two probe systems at different poloidal / toroidal positions. Using the criteria of both matching potential profiles and LRCs, plasma potential asymmetries has been identified in the ion-root plasma. The level of asymmetry was found to increase with electron temperature reaching values up to 20 V. This is consistent with previous measurement in ECRH plasmas in TJ-II. Then, plasma potential asymmetries are ubiquitous in the TJ-II stellarator.

The flexibility of mid-size devices together with their unique diagnostic capabilities reported in this thesis make them ideally suited to study the relation between magnetic topology, electric fields and transport.

Bibliography

[1] IEA. *World Energy Outlook 2015* (OECD Publishing, Paris, 2015).

[2] Stocker, T. F. *et al.* IPCC, 2013: Summary for Policymakers. In *Climate Change 2013: The Physical Science Basis* (Cambridge University Press, 2013).

[3] Freidberg, J. P. *Plasma physics and fusion energy* (Cambridge University Press, 2007).

[4] Oliphant, M. L. E., Harteck, P. & Rutherford, L. Transmutation Effects Observed with Heavy Hydrogen. *Proc. R. Soc. Lond. A* **144**, 692–703 (1934).

[5] Urey, H. C., Brickwedde, F. G. & Murphy, G. M. A Hydrogen Isotope of Mass 2 and its Concentration. *Phys. Rev.* **40**, 1–15 (1932).

[6] Lawson, J. D. Some Criteria for a Power Producing Thermonuclear Reactor. *Proc. Phys. Soc. B* **70**, 6 (1957).

[7] Miyamoto, K. *Fundamentals of plasma physics and controlled fusion* (Nagoya Inst., 2011), 3 edn.

[8] Helander, P. *et al.* Stellarator and tokamak plasmas: a comparison. *Plasma Phys. Control. Fusion* **54**, 124009 (2012).

[9] Spong, D. A. 3D toroidal physics: Testing the boundaries of symmetry breaking. *Phys. Plasmas* **22**, 055602 (2015).

[10] Wesson, J. *Tokamaks*. International Series of Monographs on Physics (Oxford University Press, 2004), 3 edn.

[11] Nishikawa, K. & Wakatani, M. *Plasma Physics: Basic Theory with Fusion Applications* (Springer-Verlag Berlin Heidelberg, 2000), 3 edn.

[12] Lyman Spitzer, J. The Stellarator Concept. *Phys. Fluids* **1**, 253–264 (1958).

[13] Boozer, A. H. Stellarator design. *J. Plasma Phys.* **81**, 515810606 (2015).

[14] Wakatani, M. *Stellarator and Heliotron Devices*. International series of monographs on physics (Oxford University Press, 1998).

[15] Wolf, R. C. *et al.* First plasma operation of Wendelstein 7-X. In *26th IAEA Int. Conf. on Fusion Energy*, OV/3–1 (Kyoto, Japan, 2016).

[16] Xanthopoulos, P. *et al.* Controlling Turbulence in Present and Future Stellarators. *Phys. Rev. Lett.* **113**, 155001 (2014).

[17] Mynick, H. E., Pomphrey, N. & Xanthopoulos, P. Optimizing Stellarators for Turbulent Transport. *Phys. Rev. Lett.* **105**, 95004 (2010).

[18] Bodin, H. A. B. The reversed field pinch. *Nucl. Fusion* **30**, 1717–1737 (1990).

[19] Taylor, J. B. Relaxation of Toroidal Plasma and Generation of Reverse Magnetic Fields. *Phys. Rev. Lett.* **33**, 1139–1141 (1974).

[20] Taylor, G. I. The Spectrum of Turbulence. *Proc. R. Soc. Lond. A* **164**, 476–490 (1938).

[21] Kolmogorov, A. N. The local structure of turbulence in incompressible viscous fluid for very large Reynolds numbers. *Dokl. Akad. Nauk SSSR* **434**, 9–13 (1941).

[22] Kraichnan, R. H. Inertial Ranges in Two-Dimensional Turbulence. *Phys. Fluids* **10**, 1417–1423 (1967).

[23] Hasegawa, A., Maclennan, C. G. & Kodama, Y. Nonlinear behavior and turbulence spectra of drift waves and Rossby waves. *Phys. Fluids* **22**, 2122–2129 (1979).

[24] Hidalgo, C. On the physics of plasma rotation in fusion plasmas. *Phys. Scr.* **T131**, 014037 (2008).

[25] Tynan, G. R., Fujisawa, A. & McKee, G. A review of experimental drift turbulence studies. *Plasma Phys. Control. Fusion* **51**, 113001 (2009).

[26] Sanchez, R. Lecture on Turbulence in Plasmas (2013). (Universidad Carlos III de Madrid).

[27] Biglari, H., Diamond, P. H. & Terry, P. W. Influence of sheared poloidal rotation on edge turbulence. *Phys. Fluids B* **2**, 1–4 (1990).

[28] Terry, P. Suppression of turbulence and transport by sheared flow. *Rev. Mod. Phys.* **72**, 109–165 (2000).

[29] Hidalgo, C., Talmadge, J. & Ramisch, M. Advancing the understanding of plasma transport in mid-size stellarators. In *43rd EPS Conf. on Plasma Physics*, EV.002 (Leuven, Belgium, 2016).

[30] Diamond, P. H. & Kim, Y. B. Theory of mean poloidal flow generation by turbulence. *Phys. Fluids B* **3**, 1626–1633 (1991).

[31] Hidalgo, C. *et al.* Radial Structure of Reynolds Stress in the Plasma Boundary of Tokamak Plasmas. *Phys. Rev. Lett.* **83**, 2203–2205 (1999).

[32] Xu, Y. H. *et al.* Role of Reynolds Stress-Induced Poloidal Flow in Triggering the Transition to Improved Ohmic Confinement on the HT-6M Tokamak. *Phys. Rev. Lett.* **84**, 3867–3870 (2000).

[33] Lin, Z., Hahm, T. S., Lee, W. W., Tang, W. M. & White, R. B. Turbulent Transport Reduction by Zonal Flows: Massively Parallel Simulations. *Science* **281**, 1835–1837 (1998).

[34] Fujisawa, A. *et al.* Identification of Zonal Flows in a Toroidal Plasma. *Phys. Rev. Lett.* **93**, 165002 (2004).

[35] Winsor, N., Johnson, J. L. & Dawson, J. M. Geodesic Acoustic Waves in Hydromagnetic Systems. *Phys. Fluids* **11**, 2448–2450 (1968).

[36] Zhao, K. *et al.* Toroidal Symmetry of the Geodesic Acoustic Mode Zonal Flow in a Tokamak Plasma. *Phys. Rev. Lett.* **96**, 255004 (2006).

[37] Diamond, P. H., Itoh, S. I., Itoh, K. & Hahm, T. S. Zonal flows in plasma - a review. *Plasma Phys. Control. Fusion* **47**, R35–R161 (2005).

[38] Fujisawa, A. A review of zonal flow experiments. *Nucl. Fusion* **49**, 013001 (2009).

[39] Starr, V. P. *Physics of negative viscosity phenomena*. Earth and planetary science series (McGraw-Hill, 1968).

[40] Hidalgo, C. Multi-scale physics and transport barriers in fusion plasmas. *Plasma Phys. Control. Fusion* **53**, 074003 (2011).

[41] Watanabe, T.-H., Sugama, H. & Ferrando-Margalet, S. Reduction of Turbulent Transport with Zonal Flows Enhanced in Helical Systems. *Phys. Rev. Lett.* **100**, 195002 (2008).

[42] Losada, U. *et al.* Influence of long-scale length radial electric field components on zonal flow-like structures in the TJ-II stellarator. *Plasma Phys. Control. Fusion* **58**, 84005 (2016).

[43] Hillesheim, J. C. *et al.* Stationary zonal flows during formation of the edge transport barrier in the JET tokamak. *Phys. Rev. Lett.* **116**, 065002 (2016).

[44] Bessenrodt-Weberpals, M. *et al.* The isotope effect in ASDEX. *Nucl. Fusion* **33**, 1205 (1993).

[45] Hawryluk, R. J., Adler, H. & Alling, P. Confinement and heating of a deuterium-tritium plasma. *Phys. Rev. Lett.* **72**, 3530–3533 (1994).

[46] Stroth, U. A comparative study of transport in stellarators and tokamaks. *Plasma Phys. Control. Fusion* **40**, 9–74 (1998).

[47] Ryter, F. *et al. Nucl. Fusion* **53**, 113003 (2013).

[48] McKee, G. R. *et al.* Non-dimensional scaling of turbulence characteristics and turbulent diffusivity. *Nucl. Fusion* **41**, 1235 (2001).

[49] Liu, B. *et al.* Isotope effect physics, turbulence and long-range correlation studies in the TJ-II stellarator. *Nucl. Fusion* **55**, 112002 (2015).

[50] Ryter, F. *et al.* Experimental evidence for the key role of the ion heat channel in the physics of the L–H transition. *Nucl. Fusion* **54**, 83003 (2014).

[51] Pedrosa, M. A. *et al.* Evidence of Long-Distance Correlation of Fluctuations during Edge Transitions to Improved-Confinement Regimes in the TJ-II Stellarator. *Phys. Rev. Lett.* **100**, 215003 (2008).

[52] Wilcox, R. S. *et al.* Measurements of bicoherence and long-range correlations during biasing in the HSX stellarator. *Nucl. Fusion* **51**, 83048 (2011).

[53] Manz, P., Ramisch, M. & Stroth, U. Poloidal mode structure of long-distance correlation of fluctuations under strong E×B shear in the torsatron TJ-K. *Phys. Plasmas* **16**, 042309 (2009).

[54] Dunne, M. G. *et al.* The role of the density profile location on pedestal stability in ASDEX-Upgrade. In *26th IAEA Int. Conf. on Fusion Energy*, EX/3–5 (Kyoto, Japan, 2016).

[55] Bourdelle, C. *et al.* L to H mode transition: on the role of Z eff. *Nucl. Fusion* **54**, 22001 (2014).

[56] Xu, Y. *et al.* Isotope Effect and Multiscale Physics in Fusion Plasmas. *Phys. Rev. Lett.* **110**, 265005 (2013).

[57] Liu, B. *et al.* Multi-scale study of the isotope effect in ISTTOK. *Nucl. Fusion* **56**, 056012 (2016).

[58] Ramisch, M. *et al.* ρs scaling of characteristic turbulent structures in the torsatron TJ-K. *Phys. Plasmas* **12**, 032504 (2005).

[59] Bustos, A., Bañón Navarro, A., Görler, T., Jenko, F. & Hidalgo, C. Microturbulence study of the isotope effect. *Phys. Plasmas* **22**, 012305 (2015).

[60] Garcia, J. *et al.* Relation of plasma flow structures to particle tracer orbits. In *26th IAEA Int. Conf. on Fusion Energy*, TH/6–3 (Kyoto, Japan, 2016).

[61] Joffrin, E. *et al.* Impact of divertor geometry on ITER scenarios performance in the JET metallic wall. In *25th IAEA Int. Conf. on Fusion Energy*, EX/P5–40 (St. Petersburg, 2014).

[62] de la Cal, E. & Team, T. T.-I. Visualising the electron density structure of blobs and studying its possible effect on neutral turbulence. *Nucl. Fusion* **56**, 106031 (2016).

[63] Burhenn, R. *et al.* On impurity handling in high performance stellarator/heliotron plasmas. *Nucl. Fusion* **49**, 65005 (2009).

[64] McCormick, K. *et al.* New advanced operational regime on the W7-AS stellarator. *Phys. Rev. Lett.* **89**, 015001 (2002).

[65] Yoshinuma, M. *et al.* Observation of an impurity hole in the Large Helical Device. *Nucl. Fusion* **49**, 62002 (2009).

[66] Happel, T. *et al.* Core turbulence behavior moving from ion-temperature-gradient regime towards trapped-electron-mode regime in the ASDEX Upgrade tokamak and comparison with gyrokinetic simulation. *Phys. Plasmas* **22**, 032503 (2015).

[67] Hidalgo, C. *et al.* On the influence of ECRH on neoclassical and anomalous mechanisms using a dual Heavy Ion Beam Probe diagnostic in the TJ-II stellarator. In *26th IAEA Int. Conf. on Fusion Energy*, EX/P7–44 (Kyoto, Japan, 2016).

[68] Pedrosa, M. A. *et al.* Electrostatic potential variations along flux surfaces in stellarators. *Nucl. Fusion* **55**, 052001 (2015).

[69] García-Regaña, J. M. *et al.* On neoclassical impurity transport in stellarator geometry. *Plasma Phys. Control. Fusion* **55**, 074008 (2013).

[70] Liu, B. *et al.* Direct experimental evidence of asymmetry in the modulation of potential in magnetic flux surfaces in the TJ-II stellarator (2016). (to be submitted to Nuclear Fusion).

[71] Alejaldre, C. *et al.* TJ-II project: A flexible heliac stellarator. *Fusion Science and Technology* **17**, 131–139 (1990).

[72] Varandas, C. A. F. *et al.* Engineering aspects of the tokamak ISTTOK. *Fusion Technology* **29**, 105–115 (1996).

[73] Sonato, P. *et al.* Machine modification for active MHD control in RFX. *Fusion Engineering and Design* **66-68**, 161–168 (2003).

[74] Rostagni, G. RFX: an expected step in RFP research. *Fusion Engineering and Design* **25**, 301–313 (1995).

[75] Lorenzini, R. *et al.* Self-organized helical equilibria as a new paradigm for ohmically heated fusion plasmas. *Nature Physics* **5**, 570–574 (2009).

[76] Piovesan, P. *et al.* RFX-mod: A multi-configuration fusion facility for three-dimensional physics studies. *Phys. Plasmas* **20**, 056112 (2013).

[77] Stangeby, P. C. *The plasma boundary of magnetic fusion devices* (Institute of Physics Pub., 2000).

[78] Sheridan, T. E. How big is a small Langmuir probe? *Physics of Plasmas* **7**, 3084 (2000).

[79] Pedrosa, M. A. *et al.* Empirical Similarity of Frequency Spectra of the Edge-Plasma Fluctuations in Toroidal Magnetic-Confinement Systems. *Phys. Rev. Lett.* **82**, 3621–3624 (1999).

[80] Kim, Y. C. & Powers, E. J. Digital Bispectral Analysis and Its Applications to Nonlinear Wave Interactions. *IEEE Transactions on Plasma Science* **7**, 120–131 (1979).

[81] Hidalgo, C. *et al.* Experimental evidence of three-wave coupling on plasma turbulence. *Phys. Rev. Lett.* **71**, 3127–3130 (1993).

[82] van Milligen, B. Ph., Hidalgo, C. & Sánchez, E. Nonlinear Phenomena and Intermittency in Plasma Turbulence. *Phys. Rev. Lett.* **74**, 395–398 (1995).

[83] Carreras, B. A., Newman, D. E., van Milligen, B. Ph. & Hidalgo, C. Long-range time dependence in the cross-correlation function. *Phys. Plasmas* **6**, 485–494 (1999).

[84] Johnson, E. O. & Malter, L. A floating double probe method for measurements in gas discharges. *Phys. Rev.* **80**, 58–68 (1950).

[85] Levinson, S. J., Beall, J. M., Powers, E. J. & Bengtson, R. D. Space/time statistics of the turbulence in a tokamak edge plasma. *Nucl. Fusion* **24**, 527 (1984).

[86] Hidalgo, C. *et al.* Plasma fluctuations near the shear layer in the ATF torsatron. *Nucl. Fusion* **31**, 1471–1478 (1991).

[87] Chen, S. L. & Sekiguchi, T. Instantaneous direct-display system of plasma parameters by means of triple probe. *J. Appl. Phys.* **36**, 2363–2375 (1965).

[88] Tsui, H. Y. W. *et al.* A new scheme for Langmuir probe measurement of transport and electron temperature fluctuations. *Rev. Sci. Instrum.* **63**, 4608–4610 (1992).

[89] Silva, C. *et al.* Fluctuation measurements using a five-pin triple probe in the Joint European Torus boundary plasma. *Rev. Sci. Instrum.* **75**, 4314 (2004).

[90] Ross, D. W. On standard forms for transport equations and quasilinear fluxes. *Plasma Phys. Control. Fusion* **34**, 137 (1992).

[91] Hidalgo, C. *et al.* Multi-scale physics mechanisms and spontaneous edge transport bifurcations in fusion plasmas. *EPL (Europhysics Letters)* **87**, 55002 (2009).

[92] Xu, Y. *et al.* Long-range correlations and edge transport bifurcation in fusion plasmas. *Nucl. Fusion* **51**, 63020 (2011).

[93] Pedrosa, M. A. *et al.* Fast movable remotely controlled Langmuir probe system. *Rev. Sci. Instrum.* **70**, 415 (1999).

[94] Spolaore, M. *et al.* Direct Measurement of Current Filament Structures in a Magnetic-Confinement Fusion Device. *Phys. Rev. Lett.* **102**, 165001 (2009).

[95] Carralero Ortiz, D. *Electromagnetic Instability Studies in Fusion Plasmas Edge*. Phd, Universidad Politécnica de Madrid (2012).

[96] Van Oost, G. *et al.* Turbulent transport reduction by E × B velocity shear during edge plasma biasing: recent experimental results. *Plasma Phys. Control. Fusion* **45**, 621 (2003).

[97] Velasco, J., Alonso, J., Calvo, I. & Arévalo, J. Vanishing neoclassical viscosity and physics of the shear layer in stellarators. *Phys. Rev. Lett.* **109**, 135003 (2012).

[98] Kitajima, S. *et al.* Electrode biasing experiment in the Large Helical Device. *Nucl. Fusion* **51**, 083029 (2011).

[99] Silva, C. *et al.* Transport and fluctuations during electrode biasing on TJ-II. *Czech. J. Phys.* **55**, 1589–1596 (2005).

[100] Pedrosa, M. A. *et al.* Isotope effect on zonal flows and searching for asymmetries in potential profiles in the TJ-II stellarator. In *40th EPS Conf. on Plasma Physics*, P2.180 (Espoo, Finland, 2013).

[101] Altukhov, A. B. *et al.* Poloidal inhomogeneity of turbulence parameters in the FT-2 tokamak by radial correlation Doppler reflectometry. In *41st EPS Conf. on Plasma Physics*, P4.061 (Berlin, 2014).

[102] Hidalgo, C., Pedrosa, M. A., García, L. & Ware, A. Experimental evidence of coupling between sheared-flow development and an increase in the level of turbulence in the TJ-II stellarator. *Phys. Rev. E* **70**, 067402 (2004).

[103] Zurro, B. *et al.* Studying the impurity charge and main ion mass dependence of impurity confinement in ECR-heated TJ-II stellarator. *Plasma Phys. Control. Fusion* **56**, 124007 (2014).

[104] Petty, C. C. Sizing up plasmas using dimensionless parameters. *Phys. Plasmas* **15**, 080501 (2008).

[105] Petty, C. C. *et al.* Gyroradius Scaling of Electron and Ion Transport. *Phys. Rev. Lett.* **74**, 1763–1766 (1995).

[106] Lin, Z., Ethier, S., Hahm, T. S. & Tang, W. M. Size Scaling of Turbulent Transport in Magnetically Confined Plasmas. *Phys. Rev. Lett.* **88**, 195004 (2002).

[107] Sokolov, V. & Sen, A. K. A new paradigm for plasma turbulent transport. *Nucl. Fusion* **45**, 439 (2005).

[108] Hidalgo, C. Progress regarding magnetic confinement experiments, plasma–materials interactions and plasma performance. *Nucl. Fusion* **55**, 104025 (2015).

[109] Gurchenko, A. D., Gusakov, E. Z. & Niscala, P. The Isotope Effect in GAM – Turbulence Interplay and Anomalous Transport in Tokamak. In *25th IAEA Int. Conf. on Fusion Energy* (St. Petersburg, 2014).

[110] Watanabe, T. H., Sugama, H. & Nunami, M. Effects of equilibrium-scale radial electric fields on zonal flows and turbulence in helical configurations. *Nucl. Fusion* **51**, 123003 (2011).

[111] Hahm, T., Wang, L., Wang, W., Yoon, E. & Duthoit, F. Isotopic dependence of residual zonal flows. *Nucl. Fusion* **53**, 072002 (2013).

[112] Silva, C. *et al.* Characterization of geodesic acoustic modes in the ISTTOK edge plasma. *Plasma Phys. Control. Fusion* **51**, 85009 (2009).

[113] van Milligen, B. Ph. *et al.* The use of the biorthogonal decomposition for the identification of zonal flows at TJ-II. *Plasma Phys. Control. Fusion* **57**, 025005 (2015).

[114] Liu, A. D. *et al.* Characterizations of Low-Frequency Zonal Flow in the Edge Plasma of the HL-2A Tokamak. *Phys. Rev. Lett.* **103**, 95002 (2009).

[115] Hennequin, P. Comprehensive experimental study of plasma turbulence structure and its scaling with ρ *. In *42nd EPS Conf. on Plasma Physics* (Lisbon, 2015).

[116] Vianello, N. *et al.* Reynolds and Maxwell stress measurements in the reversed field pinch experiment Extrap-T2R. *Nucl. Fusion* **45**, 761 (2005).

[117] Spolaore, M. *et al.* Turbulent electromagnetic filaments in actively modulated toroidal plasma edge. *Nucl. Fusion* **55**, 063041 (2015).

[118] Alonso, J. A. *et al.* Dynamics of zonal-flow-like structures in the edge of the TJ-II stellarator. *Plasma Phys. Control. Fusion* **55**, 014001 (2013).

[119] Happel, T. *et al.* Scale-selective turbulence reduction in H-mode plasmas in the TJ-II stellarator. *Phys. Plasmas* **18**, 102302 (2011).

[120] Castejón, F. *et al.* 3D effects on transport and plasma control in the TJ-II stellarator. In *26th IAEA Int. Conf. on Fusion Energy*, OV/5–1 (Kyoto, Japan, 2016).

[121] Hidalgo, C. *et al.* Generation of sheared poloidal flows via Reynolds stress and transport barrier physics. *Plasma Phys. Control. Fusion* **42**, A153–A160 (2000).

[122] Ida, K. *et al.* Observation of plasma flow at the magnetic island in the large helical device. *Phys. Rev. Lett.* **88**, 015002 (2002).

[123] Estrada, T. *et al.* Plasma flow, turbulence and magnetic islands in TJ-II. *Nucl. Fusion* **56**, 026011 (2016).

[124] Liang, Y. *et al.* Active control of type-I edge-localized modes with n=1 perturbation fields in the JET tokamak. *Phys. Rev. Lett.* **98**, 265004 (2007).

[125] Vianello, N. *et al.* Magnetic perturbations as a viable tool for edge turbulence modification. *Plasma Phys. Control. Fusion* **57**, 014027 (2015).

[126] Vianello, N. *et al.* 3D effects on the RFX-mod boundary. *Nucl. Fusion* **53**, 073025 (2013).

[127] Hurst, H. E. Long-Term Storage Capacity of Reservoirs. *Transactions of the American Society of Civil Engineers* **1**, 770–799 (1951).

[128] van Milligen, B. Ph. *et al.* Parallel and perpendicular turbulence correlation length in the TJ-II Stellarator. *Nucl. Fusion* **53**, 093025 (2013).

[129] van Milligen, B. Ph. *et al.* The role of magnetic islands in modifying long range temporal correlations of density fluctuations and local heat transport. *Nucl. Fusion* **56**, 16013 (2016).

[130] Ji, X. Q. *et al.* On the interplay between neoclassical tearing modes and nonlocal transport in toroidal plasmas. *Scientific Reports* **6**, 32697 (2016).

[131] Marrelli, L. *et al.* Magnetic self organization, MHD active control and confinement in RFX-mod. *Plasma Phys. Control. Fusion* **49**, B359 (2007).

[132] De Masi, G. *et al.* Electrostatic properties and active magnetic topology modification in the RFX-mod edge plasma. *Nucl. Fusion* **53**, 083026 (2013).

[133] López-Bruna, D. *et al.* First dynamic magnetic configuration scans in ECRH plasmas of the TJ-II Heliac. *Nucl. Fusion* **49**, 085016 (2009).

[134] Pedrosa, M. A. *et al.* Sheared flows and turbulence in fusion plasmas. *Plasma Phys. Control. Fusion* **49**, B303–B311 (2007).

[135] Spolaore, M. *et al.* Electromagnetic turbulent structures: A ubiquitous feature of the edge region of toroidal plasma configurations. *Phys. Plasmas* **22**, 012310 (2015).

[136] MacLatchy, C. S., Boucher, C., Poirier, D. A. & Gunn, J. Gundestrup: A Langmuir/Mach probe array for measuring flows in the scrape-off layer of TdeV. *Rev. Sci. Instrum.* **63**, 3923–3929 (1992).

[137] Martines, E. *et al.* The plasma boundary in single helical axis RFP plasmas. *Nucl. Fusion* **50**, 035014 (2010).

[138] Innocente, P., Lorenzini, R., Terranova, D. & Zanca, E. P. FLiT: A field line trace code for magnetic confinement devices (2016). (submitted to PPCF).

[139] Zanca, P. & Terranova, D. Reconstruction of the magnetic perturbation in a toroidal reversed field pinch. *Plasma Phys. Control. Fusion* **46**, 1115 (2004).

[140] Mandelbrot, B. B. & Wallis, J. R. Noah, Joseph, and operational hydrology. *Water resources research* **4**, 909–918 (1968).

[141] Sánchez, R., Carreras, B. A., Newman, D. E., Lynch, V. E. & van Milligen, B. Ph. Renormalization of tracer turbulence leading to fractional differential equations. *Phys. Rev. E* **74**, 016305 (2006).

[142] López-Bruna, D. *et al.* Magnetic resonances and electric fields in the TJ-II Heliac. *Plasma Phys. Control. Fusion* **53**, 124022 (2011).

[143] Carreras, B. A., Llerena Rodríguez, I. & García, L. Topological structures of the resistive pressure gradient turbulence with averaged poloidal flow. *Nucl. Fusion* **54**, 103005 (2014).

[144] Lorenzini, R. *et al.* The isotope effect in the RFX-mod experiment. *Nucl. Fusion* **55**, 043012 (2015).

[145] Alonso, J. A. *et al.* Parallel impurity dynamics in the TJ-II stellarator. *Plasma Phys. Control. Fusion* **58**, 74009 (2016).

[146] Churchill, R. M. *et al.* Poloidal asymmetries in edge transport barriers. *Phys. Plasmas* **22**, 056104 (2015).

[147] Nold, B. *et al.* Influence of temperature fluctuations on plasma turbulence investigations with Langmuir probes. *New J. Phys.* **14**, 063022 (2012).